Grain Size Control and Microstructural Evolution in Nanocrystalline Ni-W Alloys

by

Andrew J. Detor

B.S., Materials Science and Engineering
Rensselaer Polytechnic Institute, 2003

SUBMITTED TO THE DEPARTMENT OF MATERIALS SCIENCE AND ENGINEERING
IN PARTIAL FULFILLMENT OF THE REQUIREMENTS FOR THE DEGREE OF

DOCTOR OF PHILOSOPHY IN MATERIALS SCIENCE AND ENGINEERING
AT THE
MASSACHUSETTS INSTITUTE OF TECHNOLOGY

JUNE 2007

Signature of Author: _____

Department of Materials Science and Engineering
April 30, 2007

Certified by: _____

Christopher A. Schuh
Danae and Vasilios Salapatas Associate Professor of Metallurgy
Thesis Supervisor

Accepted by: _____

Samuel M. Allen
Chair, Departmental Committee for Graduate Students

Grain Size Control and Microstructural Evolution in Nanocrystalline Ni-W Alloys

by

Andrew J. Detor

Submitted to the Department of Materials Science and Engineering on April 30, 2007 in Partial Fulfillment of the Requirements for the Degree of Doctor of Philosophy in Materials Science and Engineering

ABSTRACT

Nanocrystalline materials have been studied extensively over the past two decades because of their useful and interesting physical properties. In most cases, these properties derive from the fine characteristic length scale of nanocrystalline structures and are superior to those realized in traditional coarse-grained materials. A fundamental challenge, however, involves the synthesis of high-quality specimens, which represent a classical far-from-equilibrium state due to the large presence of high-energy interfaces. Alloying presents a possibility to reduce this energy penalty through solute segregation and thermodynamic stabilization of the grain boundaries. The present work exploits this concept in the nanocrystalline Ni-W system. Atomistic computer simulations are used to evaluate the potential for stabilization based on the equilibrium solute distribution and energetics of nanocrystalline structures. Following this, a synthesis technique based on electrodeposition is developed where precise control over the alloying addition correlates with precise control over grain size. Investigations of the microstructure involving techniques such as transmission electron microscopy, x-ray diffraction, and atom probe tomography provide a detailed view of the structure and solute distribution in these materials, and the results are compared with atomistic simulations and thermodynamic models of nanostructure stabilization. The elevated temperature behavior of experimental specimens is also evaluated and compared to analytical models of microstructural evolution, showing that grain boundary relaxation is an important mechanism for the finest nanocrystalline grain sizes, having a significant influence on properties. With a new degree of control over the nanostructure, Ni-W alloys are produced over a broad range of grain sizes to investigate hardness trends and the breakdown of a classical scaling law in the nanocrystalline regime. An extension of the synthesis technique is also demonstrated for the production of functionally graded and nano-scale composite materials. Potential benefits of the methods developed in this work are highlighted for both fundamental scientific investigations and practical applications.

Thesis Supervisor: Christopher A. Schuh

Title: Danae and Vasilios Salapatas Associate Professor of Metallurgy

Acknowledgements

I would like to thank the members of my thesis committee, Professor Gerbrand Ceder, Professor Donald Sadoway, and Professor Subra Suresh, for their time and insightful comments. I would also like to thank all the members of the Schuh research group, both past and present, including especially Professor Megan Frary, Dr. Alan Lund, Jason Trelewicz, Corinne Packard, Ying Chen, Shiyun Ruan, and Jeremy Mason. These people have engaged me in a number of stimulating discussions over the years, and have made working in the lab a pleasure.

Outside of MIT I have a number of other friends to thank for keeping the work/life balance in line (as much as possible) these past four years: Damon Smith, Steve Flanagan, Ryan DeStefano, Scott Petit, Jeff Duncan, Chris Palmieri, Nate Adams, Chris Egnatz, Tina Bilotta, and most of all, Mia Corcione, who has been there through it all. My family has also been a great support, and I thank both my parents, Lyn and Joe Detor, as well as my sister Jessy for everything.

Lastly, I would like to thank my advisor, Professor Chris Schuh, who has taught me more during the Ph.D. process than I could have ever imagined, not only in terms of fundamental materials science, but also in what it means to do good, meaningful research. Chris has inspired and challenged me with his forward-thinking and creativity, and will continue to serve as a role model throughout my professional career.

Table of contents

List of Figures

Figure 2.5: The Warren-Cowley order parameter, α_k, plotted for each nearest neighbor shell, k, in the (a) 2, (b) 3, and (c) 4 nm grain size structures over a range of global W content. In (d), the order parameter is plotted for an energy-minimized single crystal structure and the 4 nm grain size, 10 at%W data are shown for comparison. Significant chemical ordering is present in the single crystal, while it is suppressed to some extent in the nanocrystalline structures.

Figure 2.6: The Warren-Cowley order parameter, α_k, plotted for each nearest-neighbor shell, k, now as a function of position within the 3 nm grain size structure containing 20 at%W. "Inner" signifies the center 1/3 portion of the grain, and "mid" and "outer" indicate a progression towards the grain boundary region. The greatest degree of ordering is seen in the center, crystalline region of the grains while the grain boundaries appear to induce disordering.

Figure 2.7: Segregation energy, H_{seg}, for simulated Ni-W alloys with 2, 3, and 4 nm grain size plotted as a function of global composition. An exponential decrease is observed with alloying addition due to solute-solute interactions in the grain boundaries.

Figure 2.8: (a) Formation energy in the fully relaxed state after Monte Carlo simulation for the 2, 3, and 4 nm grain size structures (ΔE_f^{defect}) along with the corresponding single crystal ("SC") energy (ΔE_f^{ideal}) having the same degree of short-range order as the polycrystal in each case; typical error on this measurement is shown for the 2 nm, 35 at%W point. (b) Grain boundary energy, γ, calculated for the 2, 3, and 4 nm grain size structures using Eq. (2.4) with the ΔE_f^{defect} and ΔE_f^{ideal} values from (a). A general decrease in energy is observed in all cases; however, all data lie above $\gamma = 0$ suggesting that nanocrystalline Ni-W structures are not thermodynamically stable.

Figure 3.1: Schematic diagram of the electrodeposition set-up used to synthesize nanocrystalline Ni-W alloys.

Figure 3.2: Effect of bath temperature on the composition of electrodeposited Ni-W alloys. A constant direct current density of 0.2 A/cm^2 has been applied for all experiments.

Figure 3.3: Definition of variables that control the shape of the applied current waveform used in electrodeposition experiments.

Figure 3.4: Effect of reverse pulse (a) current density and (b) time on bulk deposit composition. Reverse pulsing is an effective means for controlling W content in the range of ~2-23 at%.

Figure 3.5: Cross-sectional SEM micrographs of nanocrystalline Ni-W specimens prepared by (a) bath temperature and (b) reverse pulsing control; both specimens have

nominally the same composition of ~8 at%W. The specimen in (a) was produced at a plating bath temperature of 45 °C (cf. Fig. 3.2) while that in (b) was deposited at 75 °C using a reverse pulse current of 0.15 A/cm2 (cf. Fig. 3.4(a)). Significant defects are observed in (a) while the (b) reverse pulsing technique yields a high quality deposit. The substrate can be seen at the bottom of both images.

Figure 3.6: Typical X-ray diffraction patterns for specimens produced using the reverse pulsing technique in Fig. 3.4(a) with global W content from 2.5-23.0 at%. The XRD grain size calculated using the integral breadth method is shown for each specimen.

Figure 3.7: Grain size-composition relationship for nanocrystalline Ni-W specimens electrodeposited using reverse pulsing (RP) and conventional (C) techniques. The range of grain sizes achievable using reverse pulsing extends that of conventional methods.

Figure 3.8: (a-c) Bright field TEM images and selected area diffraction patterns showing structural refinement with increasing solute content in Ni-W specimens; two grains are outlined in the high-resolution image (c) where lattice fringes are visible.

Figure 4.1: Representations of 3 nm grain size (a) experimental and (b) simulated structures with the tungsten atoms plotted in red; specimens are approximately 6 x 7 x 5 nm.

Figure 4.2: Composition profiles for experimental (a) $d \approx 3$ nm, (b) 10 nm, (c) 20 nm, and simulated (d) 3 nm structures. The mean composition and standard deviation are marked by thin solid and dashed lines, respectively. In the case of the simulated structure (d) the positions of grain boundaries are known, and are denoted by gray vertical bars.

Figure 4.3: Three-dimensional autocorrelation functions for experimental (a) $d \approx 3$ nm, (b) 10 nm, (c) 20 nm, and simulated (d) 3 nm structures. The first maxima, indicating the periodicity of composition fluctuations, are marked with arrows.

Figure 4.4: Frequency distributions of tungsten composition for experimental (a) $d \approx 3$ nm, (b) 10 nm, and (c) 20 nm specimens, compared with the expected single binomial distribution for a random solid solution (Eq. (4.2)). Also shown are fits of the two-constituent distribution of Eq. 4.3 where both the grain boundary and grain interior are modeled as random solid solutions (binomial-binomial) and where the standard deviation of both regions is included as an additional adjustable parameter (normal-normal). In (d), the distribution for the simulated $d = 3$ nm structure is presented, along with the normal-normal fit.

Figure 4.5: Grain size-independent McLean segregation isotherms plotted as blue and red dashed lines for constant segregation energies of H_{seg} = 55 and 10 kJ/mol, respectively, corresponding to the value assumed in a thermodynamic model of nanostructures stability for Ni-P, and the dilute limit value determined from the

present work in Ni-W (Fig. 2.7). Incorporating nanocrystalline grain-size effects (Eq. 2.3) leads to the solid blue curve for Ni-P alloys, while the exponentially decreasing form of H_{seg} (Fig. 2.7) predicts the solid red curve for Ni-W; these isotherms represent an approximation of the grain boundary segregation tendency in nanocrystalline Ni-P and Ni-W. The disparity between these two predictions (indicated by an arrow) suggests that Ni-W may not derive sufficient grain boundary energy reduction for complete thermodynamic stability. Also shown for comparison are experimental atom probe (AP) data for grain boundary composition in nanocrystalline Ni-W (Table 4.2) and Ni-P specimens.

Figure 5.1: X-ray diffraction patterns for 24 hr heat treatments of an as-deposited (AD) 3 nm grain size specimen containing 21 at%W. The structure remains fairly stable up to 450 °C followed by coarsening and eventual precipitation of the equilibrium Ni_4W phase at higher temperatures.

Figure 5.2: Grain size quantified by X-ray diffraction analysis for 24 hr heat treatments of three different starting grain sizes (plotted at 25 °C), showing excellent stability up to ~500 °C.

Figure 5.3: X-ray diffraction patterns for a ~3 nm grain size Ni-W specimen deposited in October, 2003. No change in the structure is observed after 3.5 years at room temperature, indicating the exceptional long-term stability of the present alloys.

Figure 5.4: Bright-field transmission electron microscopy images and inset selected area diffraction patterns for as-deposited (a-c) ~3 nm and (d-f) ~20 nm grain size specimens in their initial and heat treated states as indicated. Grain growth is normal in all cases.

Figure 5.5: Selected area electron diffraction intensity profiles for the (a) $d_o = 20$ nm grain size specimen containing 13 at%W and the (b) $d_o = 3$ nm grain size specimen containing 21 at%W. Short range ordering, as evidenced by intensity maxima at the {1 ½ 0} position, is observed for temperatures greater than 300 °C in both figures. (b) A long range order transition to the equilibrium Ni_4W phase appears in this higher W content alloy at sufficiently high temperature and time.

Figure 5.6: Grain boundary vs. grain interior composition for as-deposited and heat treated Ni-W alloys as reported in Chapter 4 and Appendix B, respectively; grain size is indicated next to each point. A similar extent of segregation is observed for all specimens.

Figure 5.7: Differential scanning calorimetry results showing the irreversible heat release in as-deposited 3, 20, and 70 nm grain size specimens; all experiments were performed at a scanning rate of 20 °C/min. Exothermic signals, beginning at ~120 °C, scale inversely with grain size and are attributed to grain boundary relaxation of the as-deposited Ni-W specimens.

Figure 5.8: Linear-log plot of hardness vs. grain size for specimens in both the as-deposited condition and subject to low temperature heat treatments where negligible grain growth, chemical ordering, and solute redistribution occur. Significant hardening is observed at the finest grain sizes, likely as a result of grain boundary relaxation.

Figure 5.9: Atom probe maps plotting the positions of individual W atoms within a ~70 x 90 x 4 nm section of (a) as-deposited and (b) heat treated specimens having similar grain sizes of ~10 and 16 nm, respectively. The grain structure is clearly observed in (b) possibly owing to a structural change in the grain boundaries upon annealing; the data in (b) also appear in Appendix B.

Figure 5.10: Microstructural evolution maps for (a, b) pure and (c, d) alloyed structures summarizing the relationship between initial grain size and (a, c) temperature and (b, d) time required for significant activation of grain boundary relaxation, grain growth, chemical ordering, and grain boundary segregation as described by Eqs. (5.3), (5.5), (5.6), and (5.7) with the constants given in Table 5.1. Solid lines in (a) and (c) represent the onset conditions for each mechanism, while the dashed line signifies the completion of grain boundary relaxation; all lines in (b) and (d) represent onset conditions. Kinetic ("γ_o, Q_m") and thermodynamic ("$0.4\gamma_o$, Q_m" and "$0.4\gamma_o$, $1.5Q_m$") contributions to grain growth in alloys are included in (c); see text for details.

Figure 5.11: Combining the results of Fig. 5.10(a) and (c) showing the improved thermal stability of alloys (shaded regions) as compared to pure systems.

Figure 6.1: Hardness plotted as a function of grain size for the present Ni-W alloys along with data from the literature introduced in Fig. 1.2. The present study convincingly demonstrates Hall-Petch strengthening, followed by a plateau in hardness for grain sizes less than ~10 nm.

Figure 6.2: Hardness as a function of grain size for specimens in the as-deposited condition, as well as those subject to isothermal annealing experiments from starting grain sizes of 3, 20, and 70 nm; data are compiled in Appendix C. Inverse Hall-Petch behavior is observed for the heat-treated specimens with grain size less than ~30 nm.

Figure 6.3: Patterned nanocrystalline electrodeposits synthesized using the periodic reverse pulsing technique of Chapter 3. Backscatter SEM images and composition line scans are shown at the top of both figures. Nanoindentation hardness (blue circles) and grain size (green squares) profiles show the level of structure and property control available using this method. The specimen in (a) comprises eight layers of monotonically decreasing W content, while that in (b) contains alternating layers of low and high W content. Grain size measurements in (a) were obtained from a serial sectioning X-ray study, while those in (b) are an estimate based on the composition.

Figure 6.4: Serial XRD study conducted on the eight layer specimen of Figure 6.3(a). Grain size calculated using the integral breadth method is shown along with the corresponding distance from the substrate. The star symbol (*) on the pattern closest to the substrate indicates the emergence of a copper diffraction peak as the X-rays penetrate the Ni-W specimen and begin to sample the substrate.

Figure B.1: Bright field transmission electron microscopy images and inset selected area diffraction patterns for the heat treated (a) ~16 nm (b) ~28 nm grain size Ni-W alloys containing approximately 21 and 13 at%W, respectively.

Figure B.2: Composition profiles constructed from atom probe data in the heat treated (a) ~16 nm grain size and (c) ~28 nm grain size Ni-W alloys. Autocorrelation functions revealing characteristic wavelengths in the composition profiles of (a) and (c) are presented as (b) and (d), respectively. The wavelengths are consistent with the measured grain size in both alloys, suggesting W segregation at the grain boundaries.

Figure B.3: Composition distributions for the heat treated (a) ~16 nm grain size and (b) ~28 nm grain size Ni-W alloys. A double-normal model fit to the experimental points yields information about the individual grain interior (red) and grain boundary (blue) distributions.

Figure B.4: Atom maps plotting the position of individual W atoms within a 4 nm slice of the heat treated (a) ~16 and (b) ~28 nm grain size specimens; the grain structure is seen in these images due to enhanced evaporation from the grain boundary regions. Typical (c, d) composition profiles and (e, f) ladder diagrams are taken across known grain boundary positions in (a, b), respectively. Segregation of W is observed in these constructions and the extent is consistent with the statistical analysis of Fig. B.3.

List of Tables

Chapter 1: Introduction

1.1 Properties of nanocrystalline materials

Nanocrystalline materials have generated interest in recent years in terms of both the challenges they pose to fundamental scientific understanding, and the opportunities they present for technological applications. This interest stems from the unusual and often beneficial properties nanocrystalline materials possess owing to the emergence of grain boundary-dominated physics as the grain size approaches ~100 nm and below [1-19]. At these extremely fine length-scales, grain boundaries are no longer characterized as planar defects, as their volume becomes comparable to that of the grain interior. This concept is simply illustrated through the geometric construction of Palumbo et al. [20], who expressed the volume fraction of crystalline grain interior, f_g, as a function of grain size, d, and grain boundary thickness, t, as:

$$f_g = 1 - f_{gb} = \left(\frac{d-t}{d}\right)^3 \tag{1.1}$$

where f_{gb} represents the volume fraction of grain boundaries. This relationship is plotted in Fig. 1.1 assuming a reasonable value of $t = 1$ nm. Below a grain size of ~5 nm a crossover is observed where the volume fraction of grain boundaries exceeds that of the grain interior. Given the unique, relatively disordered structure of grain boundaries [21], we may speculate that material properties should strongly depend on grain size through this transition.

Of the various techniques that may be used to investigate length-scale dependent behavior in nanocrystalline materials, atomistic computer simulations have dominated the field in recent years, mainly due to advances in accurate multi-body potentials [22, 23] and efficient coding schemes [24]. Because of these advances, it is now possible to systematically explore properties in nanocrystalline structures that are designed with precise atomic-level control over grain size, shape, distribution, and orientation. These techniques have enabled an unprecedented understanding of the atomic-level mechanisms behind macroscopic properties. For example, a number of works have focused on mechanical properties and the potential breakdown of classic

Hall-Petch strength scaling [25], which predicts that the yield strength (or hardness) of a material should increase with the inverse square-root of grain size. A simple extrapolation suggests that nanocrystalline materials should possess extremely high strength at the finest possible grain sizes. However, as grain size approaches ~10 nm and below, it has been suggested that the dislocation mechanisms responsible for the Hall-Petch relationship are no longer operative [26], and other mechanisms such as grain boundary sliding or grain rotation are activated [27-29]. This change in deformation mechanisms has indeed been observed in recent atomistic simulations concurrent with a breakdown in macroscopic properties, where yield strength no longer increases with grain refinement [14, 18]. Thus, while there are still several important drawbacks to the simulation approach, it has substantially increased our understanding of nanocrystalline materials and provided insight on the new and interesting physics that occur at these length-scales.

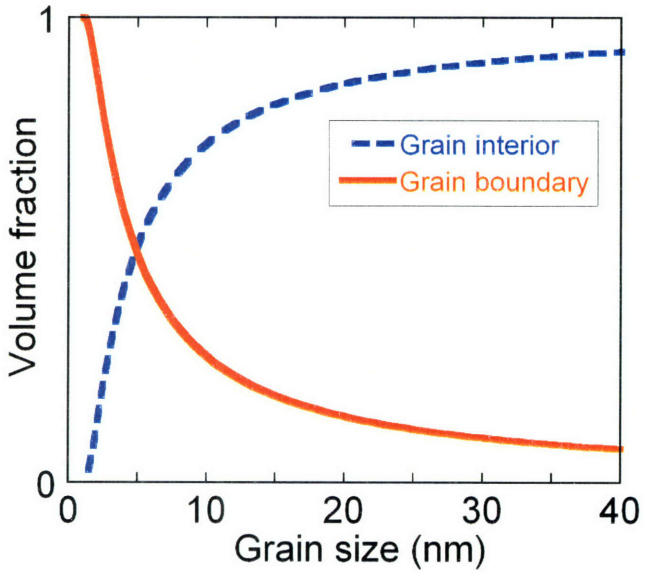

Figure 1.1: Volume fraction of grain interior and boundary regions as a function of grain size after Palumbo et al. [20]. A crossover is observed below ~5 nm where the volume fraction of grain boundaries exceeds that of the crystalline grain interior.

In order to validate analytical and computer simulation predictions, a number of works have focused on experimental techniques to directly measure grain size-dependent trends in nanocrystalline specimens. Beginning with the pioneering work of Glieter et al. [1], experiments in mechanical [9, 13], electrical [10, 15, 30], and magnetic [5, 6] properties have all shown

trends that differ significantly from those in traditional coarse-grained polycrystals. For example, considering the Hall-Petch relationship again, Fig. 1.2 plots hardness as a function of grain size collected from a number of studies in the Ni system [31-34]. Indeed, the maximum hardness observed in this figure (~7 GPa) rivals typical steels [35], supporting the beneficial effects of nanoscale grain refinement. However, for grain size below ~10 nm a breakdown in Hall-Petch scaling is suggested where hardness apparently plateaus. One of the difficulties in interpreting this trend, however, lies in the scarcity of data; no single investigation convincingly spans the entire range of grain sizes in Fig. 1.2. This lack of data is the direct result of difficulties in synthesizing the finest nanocrystalline grain sizes, and encompasses one of the major challenges in experimental approaches thus far. As such, unequivocal experimental evidence of scaling law inflections and anomalous material behavior in the nanocrystalline regime is still lacking. This forms an underlying motivation for the present work: there is need for a means to access new and interesting properties by establishing precise control over the finest nanocrystalline grain sizes.

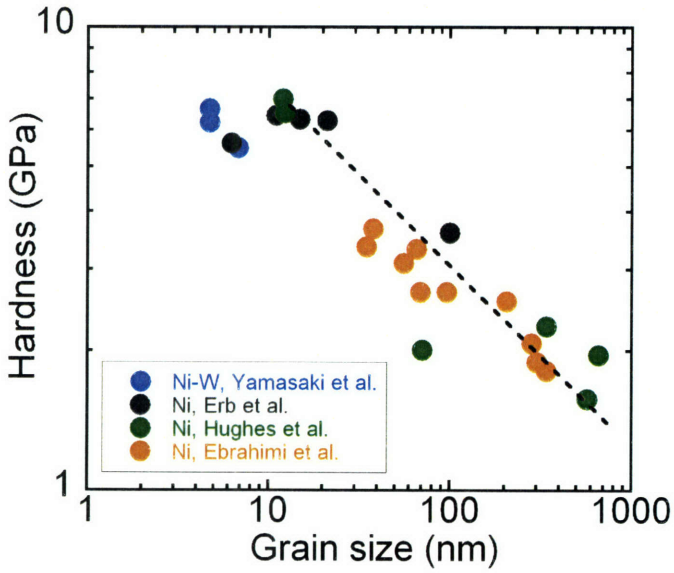

Figure 1.2: Hardness as a function of grain size collected from the literature in pure Ni [32-34] and Ni-W alloys [31]. A breakdown in classic Hall-Petch strength scaling is suggested below a grain size of ~10 nm.

1.2 Synthesis of nanocrystalline specimens

The introduction of high-energy interfaces presents a fundamental challenge in synthesizing the finest nanocrystalline grain sizes. These structures are in a constant struggle against the equilibrium tendency for grain coarsening in polycrystals. Accordingly, synthesis techniques for pure nanocrystalline materials typically involve energetic processes such as severe plastic deformation, mechanical attrition, rapid quenching, or deposition methods [32, 36-40]. In most cases, nanocrystalline grain size cannot be explicitly controlled using these far-from-equilibrium techniques, and is limited by the characteristic kinetics of the process. Severe plastic deformation, for example, cannot typically produce grain sizes below ~50 nm [40]. Other methods involving rapid quenching or mechanical attrition have been able to achieve somewhat finer grain sizes, but additional complications arise from quality issues and the inability to produce bulk specimens using these techniques [41-43]. Of the available processing routes explored to date, electrodeposition methods represent perhaps the best alternative combining high quality with the ability to access fine grain sizes in bulk specimens. However, an overriding problem in all pure systems is the inability to achieve grain sizes below ~10 nm. This fundamental limitation has prevented experimental investigations of the new and interesting behavior predicted at these extremely fine length scales.

An alternative approach that has been successful in producing the finest nanocrystalline grain sizes below ~10 nm involves alloying of two or more elements. The addition of an alloying element has fundamental thermodynamic implications for nanocrystalline metals, which can explain the unique ability of alloyed systems to exhibit fine-grained structures; this has been discussed in the works of Weissmüller [44], Kirchheim et al. [45, 46], and Beke et al. [47, 48], among others [49-52]. These studies have demonstrated the possibility of nanocrystalline structures that are in thermodynamic equilibrium due to the energetics of alloying and, in particular, due to grain boundary segregation. Such stabilized nanostructures have obvious practical advantages for applications, and also for fundamental scientific studies of material behavior.

The thermodynamic framework that has been used to describe nanostructure stabilization is based upon the change in Gibbs free energy, G, with respect to grain boundary area, A:

$$dG \propto \gamma \cdot dA \tag{1.2}$$

In a single component metal, the grain boundary energy, γ, is positive, so the system can reduce its free energy by increasing grain size. This is the usual driving force for grain growth and the reason why processing of pure nanocrystalline materials is nontrivial; they are inherently unstable with respect to grain growth. In contrast, a two-component system offers the opportunity to lower the system energy by segregating one species to the grain boundaries so that the boundary energy is reduced via an adsorption isotherm [53]. For example, assuming a high segregation tendency where nearly all solute atoms are located at the grain boundaries, use of the Gibbs adsorption isotherm gives [44, 45, 54]:

$$\gamma = \gamma_o - \Gamma\left(H_{seg} + RT \ln X\right) \tag{1.3}$$

where γ_o is the grain boundary energy of the pure polycrystalline solvent, Γ is the specific excess of solute located at the grain boundary, H_{seg} is the segregation energy, R is the gas constant, T is temperature, and X is the global solute composition. The segregation term in Eq. (1.3) now counters the positive energy penalty term, γ_o, and can stabilize the grain size at a finite value; for sufficiently high H_{seg} and Γ, the grain boundary energy can equal zero, leaving no driving force for a change in grain size. The physical basis for thermodynamic stabilization involves an interplay between the total number of high-energy grain boundary sites available at a particular nanocrystalline grain size and the global solute content of the alloy. As illustrated in Fig. 1.3, for relatively dilute alloys with small grain size there are excess grain boundary sites available for solute atoms, each with an energy penalty (i.e. the grain boundaries are "under-full"). Grain growth is preferred in this scenario to reduce the excess energy carried by the grain boundaries. In the opposite case, the grain size is too large such that grain boundaries are "overfull" and solute atoms must be rejected from the intercrystalline regions into energetically unfavorable grain interior sites; grain growth is opposed. At the equilibrium grain size these two effects are perfectly in balance, grain boundaries are at their optimal composition, the system energy is minimized, and the grain size is stable. It is important to note that this interpretation of

stability neglects the possibility of second phase precipitation, which may present a more effective route to lower the system energy. This idea has been discussed by Kirchheim [45] who concluded that a significant reduction in grain boundary energy is possible only if precipitation reactions are kinetically hindered in strongly segregating alloys. Thus, the thermodynamic calculations presented above tacitly assume the absence of such reactions.

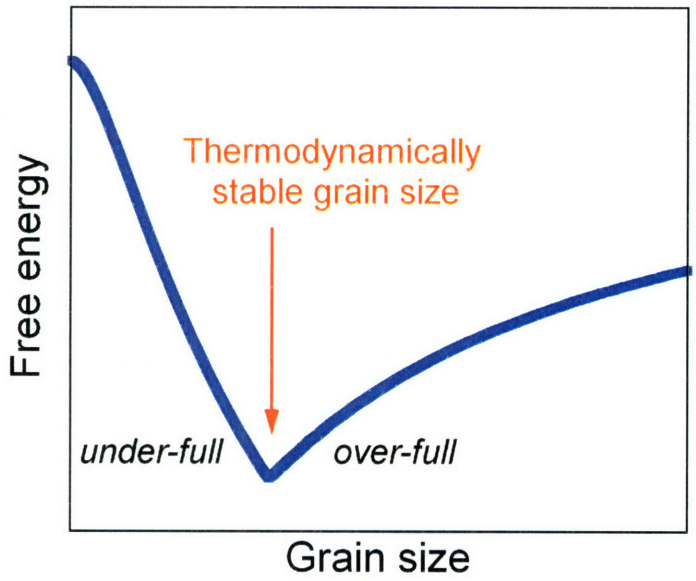

Figure 1.3: Schematic dependence of system energy on grain size for a strongly segregating nanocrystalline alloy at fixed global composition, after Weissmuller [44]. Due to the interplay between the total number of grain boundary sites available and the number of solute atoms in the system, an energy minimized state exists at a critical grain size.

While the concept of complete thermodynamic stability ($\gamma = 0$) is attractive in its simple theoretical basis, it has not yet been demonstrated that a vanishing grain boundary energy can actually be achieved in experimental alloys. In light of this, Krill et al. [49-51] have suggested an alternate, but related explanation for nanostructure stability that focuses on the kinetics of grain growth in relation to grain boundary energy. This explanation relies on a classical result describing grain boundary velocity, v, as [50, 55]:

$$v = M \cdot \frac{4\gamma}{d} \tag{1.4}$$

where M is the interface mobility. Like the previous thermodynamic description, $\gamma = 0$ in Eq. (1.4) predicts a grain boundary velocity of zero and, hence, complete stability of the structure. However, Eq. (1.4) also suggests a spectrum of increasingly stable nanocrystalline structures as γ is suppressed, but not necessarily driven completely to zero. Krill et al. [50] have experimentally shown exceptional thermal stability in the Pd-Zr system, linking this to a thermodynamic reduction of γ. Regardless of whether grain boundary energy is actually reduced to zero, grain boundary segregation leads to a reduction of grain boundary energy and improved stability.

In addition to the Pd-Zr system mentioned above, the idea that grain boundary segregation may stabilize nanocrystalline structures has also been explored experimentally in the Y-Fe [56], Ni-P [46, 57], Ru-Al [45, 46], and Fe-P [46] systems. One of the key observations in all of these systems is a monotonic relationship between grain size and composition. For example, Fig. 1.4 plots the grain size-composition relationship for an electrodeposited Ni-P alloy [46]; higher additions of the minority, segregating component lead to finer grain sizes. This trend is expected

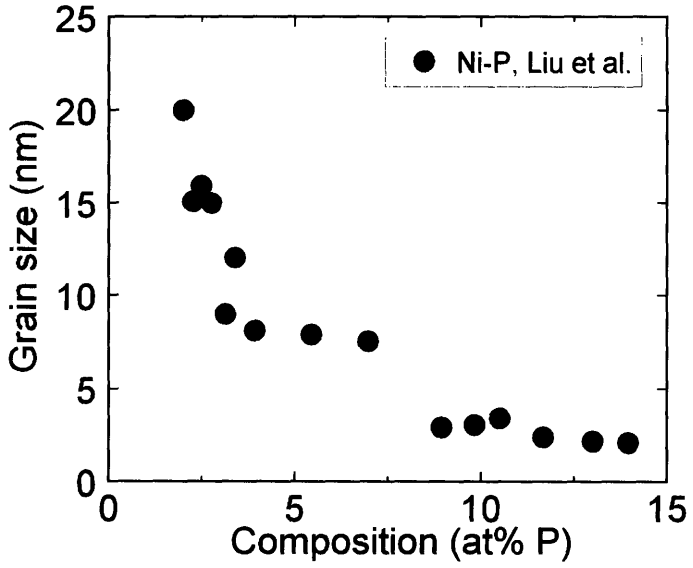

Figure 1.4: Grain size as a function of global P content in the strongly segregating Ni-P system, after Liu et al. [46]. An increase in alloying addition leads to finer nanocrystalline grain sizes due to the energetics of grain boundary segregation.

as alloys containing higher amounts of solute will prefer finer grain sizes in order to accommodate the segregating species in the grain boundaries (i.e. the energy minimum in Fig. 1.3 shifts as a function of global solute content).

The true attraction of segregation-based nanostructure stabilization lies in its thermodynamic foundation and the characteristic relationship between grain size and composition. This trend suggests a method to explicitly control the grain size of nanocrystalline alloys, but has yet to be exploited for this purpose.

1.3 Thermal stability of nanocrystalline materials

With an eye towards both practical applications and fundamental studies, a number of works have aimed at characterizing the thermal stability of nanocrystalline materials and the likelihood for grain coarsening at elevated temperatures. Not surprisingly, it has generally been found that pure nanocrystalline structures are highly unstable, with rapid grain growth occurring at relatively low temperatures. Nanocrystalline forms of Ni and Co, for example, have onset temperatures for grain growth in the range of 220-310°C [58-61], while nanocrystalline Al, Sn, Pb, and Mg have all shown significant grain growth at room temperature [62, 63]. Several nanocrystalline materials have also been found to undergo grain growth due to mechanical deformation alone [64-66]. Thus, the fundamental instability that plagues the processing of pure nanocrystalline materials also makes them undesirable for elevated temperature studies or application.

In addition to grain growth, increasing attention has been focused on the evolution of grain boundary structure during annealing of nanocrystalline materials, largely due to the dominant role these regions play in determining properties [1, 13, 17]. In particular, it has been suggested that the driven synthesis techniques typically used to produce nanocrystalline specimens result in non-equilibrium grain boundaries, containing a large number of excess dislocations [67-70]. Upon heating, kinetic processes allow these defects to annihilate in a process termed "grain boundary relaxation". This phenomenon has indeed been directly observed in coarse-grained [71, 72] and nanocrystalline structures [73] through high-resolution microscopy experiments, and has also been suggested to explain the broad exothermic reaction preceding grain growth in a

number of nanocrystalline materials [58, 60, 61, 74, 75]. Recent mechanistic models have further connected this kind of relaxation with strengthening [76], providing insight on disparate property measurements of earlier studies where nanocrystalline grain size was considered as the sole variable affecting strength. For example, Weertman [77] commented on variations in Hall-Petch data from a number of studies, observing that heat treated samples often show a much higher hardness and different strength-scaling with nanocrystalline grain size than those tested in the as-processed condition. A later study [67, 78] demonstrated that the hardness of nanocrystalline Cu can be increased by ~50% (at the same grain size) based solely on improvements in processing technique. Thus, it is clear that the state of grain boundaries and their potential relaxation should be considered as an additional variable in stability studies, especially given the significant impact on properties.

As a means to study elevated temperature behavior at the finest grain sizes, as well as extend the temperature range over which a nanocrystalline structure can be maintained, researchers have again turned to alloying. In line with the processing advantages that come with the addition of a second component, vast thermal stability improvements have been observed in a number of alloyed systems. For example, adding 3.6 at% P to Ni increases the onset temperature for grain growth from 289 to 430 °C [58]. Over the past several decades, much work has been directed at rationalizing this stability improvement by considering the kinetic and thermodynamic mechanisms governing grain growth in alloys. Kinetic descriptions typically involve classical mechanisms where solute atoms or precipitates impose drag forces on interface motion [55, 79, 80], while thermodynamic descriptions are rather unique to the nanocrystalline structure involving significant changes in grain boundary energy as discussed in Section 1.2 [44, 81]. This thermodynamic effect has been suggested, for example, to explain the impressive stability of nanocrystalline Pd-Zr [50], up to 1500 °C—fully 95% of the melting point for this material.

To identify the physical mechanisms governing alloy stability and the synergistic role of kinetic and thermodynamic contributions, detailed characterization of the solute distribution is required in nanocrystalline specimens. This includes not only an evaluation of the grain boundary segregation tendency, but also the degree of chemical ordering and possible second phase precipitation during heat treatment. Unfortunately, this information becomes difficult to access

as grain size is reduced to the finest possible levels. As such, a number of works have focused on advanced techniques such as atom probe tomography [57, 82-85], positron annihilation [86-89], or neutron scattering [78, 90] in an effort to characterize the microstructure and solute distribution. Still other works have used more traditional methods such as x-ray diffraction [83, 85, 91, 92], electron microscopy [83, 85, 91, 93, 94], or calorimetry [85, 91, 92]. Together, some combination of techniques should suffice to form an adequately complete picture of the structural and chemical evolution during heat treatment; however, only a limited number of works to date [82, 83, 85] have included such a set of experiments in a single nanocrystalline system, and we are not aware of any study that explicitly investigates all of the possible structural evolutions that may occur in nanocrystalline alloys, including segregation, ordering, grain growth, and grain boundary relaxation.

1.4 Problem statement

The above discussion suggests a number of possible areas for advancement in the study of nanocrystalline materials. In particular, a major obstacle thus far has been the inability to precisely control nanocrystalline grain size in a single system. Unlike the atomic-level structural control available in simulations, this inability has plagued experimental efforts aimed at studying length-scale dependent trends in material behavior. Therefore, a central aim of the present work is to exploit the thermodynamic effects of alloying to tailor microstructures over a wide range of the finest nanocrystalline grain sizes. We specifically focus on Ni-W as a model alloy system in this study for a number of reasons, some of which are outline below:

- Accurate multibody potentials exist for Ni-W enabling investigations via atomistic computer simulation.
- Previous works have successfully demonstrated the experimental synthesis of nanocrystalline Ni-W alloys [31, 95], although over a very limited range of grain sizes and without precise control over the structure.
- There is a vast amount of data in the literature for nanocrystalline Ni-based systems with which we may compare our results.

With Ni-W as a model alloy, the present work is outlined according to the five major themes presented below:

- Atomistic computer simulations are used to understand the energetics of alloying and evaluate the potential for nanostructure stabilization in Ni-W.
- Learning from the atomistic simulations, an experimental effort validates nanostructure control and tailorability of grain size in electrodeposited Ni-W specimens. A new, scalable, and robust synthesis technique is introduced, providing unprecedented control over composition and grain size, which should also be applicable to a broad range of other alloy systems.
- Detailed characterization of the experimental specimens is accomplished using electron microscopy and atom probe tomography, providing atomic-level resolution of the structure for direct comparison with simulation results and validation of the stabilizing mechanisms in Ni-W alloys.
- The thermal stability of nanocrystalline Ni-W is studied using a combination of techniques, paying special attention to grain boundary relaxation mechanisms that are shown to have important consequences on macroscopic properties at the finest grain sizes.
- Application of the synthesis technique developed in this work is demonstrated for the study of scaling laws and the production of a new class of patterned nanostructures.

Chapter 2: Computer simulations of nanostructure stability

As described in Section 1.2, there are existing analytical thermodynamic models of nanostructure stability, but these are unfortunately all derived for systems with a strong segregation tendency under the assumption that $H_{seg} >> RT$. In these systems, saturation-type segregation occurs resulting in significant grain boundary energy reduction via Eq. (1.3). In contrast, the Ni-W system is expected to exhibit weaker segregation tendency given the relatively high equilibrium solubility for W in Ni (~12 at% at room temperature [96]). For this more general case the thermodynamic models previously described do not apply. Accordingly, in this chapter, we resort to a more rigorous theoretical analysis of nanocrystalline Ni-W using atomistic computer simulations. Simulations have proven very successful in fundamental studies of grain boundary segregation at individual grain boundaries [97-99] and should therefore be of use to investigate nanostructure stability. To date, however, there have been very few works along these lines. Millet et al. [100, 101] have used molecular dynamics simulations to systematically study solute atom effects on grain boundary energetics in simple but informative 2-D bicrystals [101] and polycrystals [100]. By adjusting the effective size mismatch and enthalpy of solution between the solute and solvent atoms, they showed that zero (or even negative) grain boundary energy could be achieved, and grain growth suppressed, at a sufficient solute concentration. While these simulations are qualitatively instructive, the artificially introduced state of complete solute saturation at grain boundaries is unrealistic for most systems, and the 2-D geometry, simplified pairwise atomic interactions, and dilute levels of solute concentration considered prevent any direct comparison of these simulations with experimental works or proposed analytical models. Therefore, in what follows, we use system-specific potentials in fully 3-D structures to accurately simulate the solute distribution and associated energetics in nanocrystalline Ni-W alloys. The main aim of these simulations is to evaluate the potential for nanostructure stabilization as manifested through a significant reduction in grain boundary energy. Most of the work presented in this chapter has been published in Ref. [102].

2.1 Simulation procedure

To investigate nanostructure stability through computer simulation, we employ three unique polycrystalline structures with average grain sizes of 2, 3, and 4 nm. Each simulated structure contains a total of twelve grains, with 84 unique grain boundaries, and periodic boundary conditions along all three primary axes. The grain geometry as well as the crystallographic orientations of the grains are fixed across the three specimens, ensuring that the 2, 3, and 4 nm grain size structures are geometrically similar and comparisons across grain sizes isolate this variable from other structural differences. A graphical representation of the 3 nm grain size structure is presented in Fig. 2.1(a) with the grain boundary atoms highlighted in red, along with (b) an analysis of the grain boundary disorientation distribution [11]. Note that the grain orientations are selected such that the disorientation distribution is random, effectively capturing the average behavior of a bulk polycrystalline specimen. By systematically alloying the 2, 3, and 4 nm structures, we can study the equilibrium configurations and energetics as a function of global composition and grain size in nanocrystalline alloys. The atomic interactions for these simulations are modeled with a multi-body Finnis-Sinclair potential optimized for Ni-W [103], allowing for a reasonable comparison with states achieved in experiments.

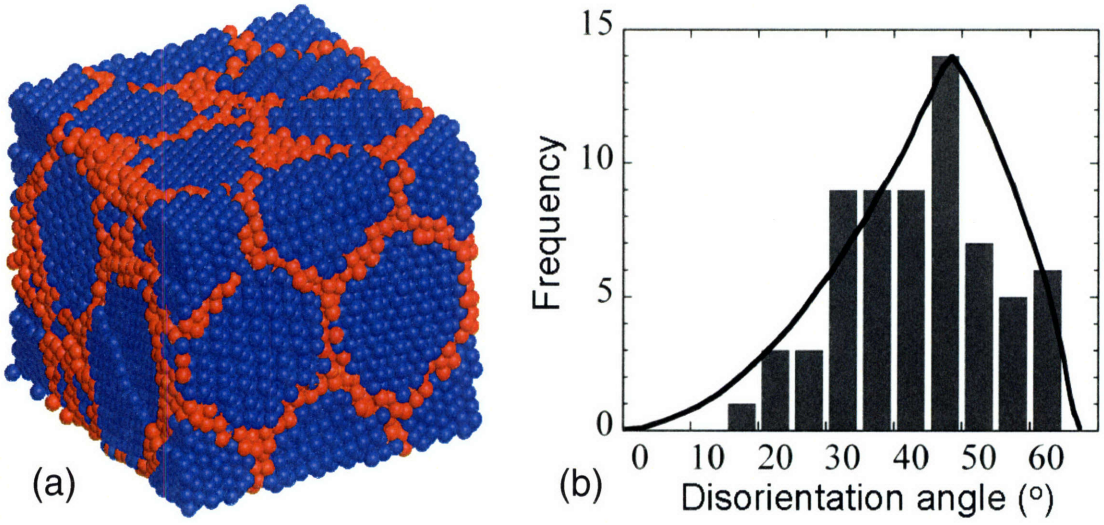

Figure 2.1: (a) A representation of the 3 nm grain size structure used in atomistic simulations, with the grain boundary atoms highlighted in red. (b) The grain boundary disorientation distribution of the simulated structure; the solid line is the MacKenzie function [104] which characterizes a specimen of random texture.

For each simulation we begin with nanocrystalline structures of pure Ni, and randomly replace Ni atoms with W up to a specified concentration. To ensure that all simulations are conducted under a state of constant zero pressure, we isotropically expand or contract this random solid solution alloy to a minimum energy cell size; strain is applied in 0.01% increments with a conjugate gradient relaxation routine of the entire structure at each step. As expected, alloys containing more of the relatively larger W atoms expand to a greater extent. Once the depressurized state is achieved for the random solid solution, a Monte Carlo procedure is then commenced, where the total system energy change is calculated after switching the positions of randomly selected Ni and W atoms. In addition to simply exchanging atoms, we also perform a complete conjugate gradient relaxation of the entire structure at every switch event. Thus, atoms are not fixed on a rigid lattice allowing for local atomic relaxations in the grain boundary and grain interior regions. While this adds significant computation time, it has been shown to be a necessary step for accurate simulations of segregation behavior [105, 106]. Atomic switches that lower the system energy are always accepted, while those that increase the energy are accepted with an Arrhenius probability dependent on temperature; here we have used 80° C which is a nominal processing temperature for nanocrystalline Ni-W alloys (see Chapter 3) [31, 95]. After a sufficient number of switch attempts, the energy of the system decreases to a minimum, at which point the simulation is complete.

For the present study, we have performed simulations on the 2, 3, and 4 nm grain size structures over a composition range from 1-40 at%W. In what follows, we first characterize the solute distribution in these structures to assess the degree of solute segregation to the grain boundary regions, and any ordering/clustering tendency. We then focus on the energetics, namely a determination of the segregation, formation, and grain boundary energies. To aid in these analyses we also introduce simulations performed on fcc single crystals (with periodic boundary conditions), which proceed in an identical manner as those described above for the polycrystalline specimens unless otherwise noted. These simulations provide a useful reference state for our discussion.

2.2 Solute distribution in nanocrystalline Ni-W

In all of our simulations, an initially random solid solution of W in nanocrystalline Ni evolves to a lower energy state through the Monte Carlo procedure. Figure 2.2(a) shows a typical plot of total system energy, initialized to the starting energy of the random solution, as a function of Monte Carlo time for a 3 nm grain size structure; in all cases the energy decreases essentially monotonically before plateauing at a minimum. The total energy drop achieved is summarized as a function of composition for the 2, 3, and 4 nm grain size structures in Fig. 2.2(b); also shown is the corresponding energy drop for a single crystal (SC) structure to be discussed later. This plot demonstrates that with increasing W content, the system can access lower energy states as compared to a random solid solution. Because the grain size is fixed in these Monte Carlo simulations (i.e., no grain growth occurs) this energy drop can only come from changes in alloy configuration. For these binary solutions there are two possibilities: segregation of solute to the grain boundary regions, or some degree of solute ordering or clustering in the structure. We examine these two effects in turn below.

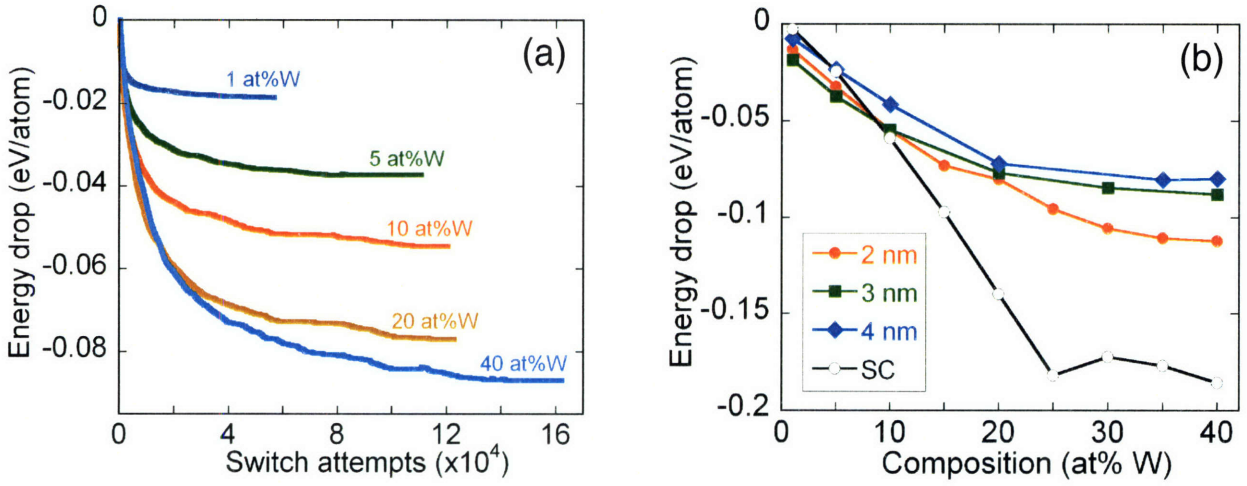

Figure 2.2: (a) Total system energy as a function of Monte Carlo switch attempts for the 3 nm grain size structure with composition ranging from 1-40 at%W; starting random solid solution energies are initialized to zero. Energy decreases to a clear minimum in all cases after a sufficient number of switches. (b) The maximum energy drop achieved in reference to a random solid solution for all simulations.

2.2.1 Grain boundary segregation

To evaluate the grain boundary segregation tendency in these simulations, we first directly visualize the position of solute atoms in their equilibrium configurations. In Fig. 2.3(a-c) a single representative 3 nm diameter grain is shown over a range of compositions from 1-20 at%W; the W atoms in this figure appear larger (and red) for visual clarity. In the dilute limit (Fig. 2.3(a, b)) it is clear that W is segregated to the grain boundaries, while the concentration is relatively low in the grain interior. In fact, the atoms that appear near the center of the grain in these projections actually occupy grain boundary sites on the front or back side of the grain. As the W content is increased, however, the structure becomes saturated and it is difficult to discern whether there is any appreciable amount of segregation (Fig. 2.3(c)). The trend illustrated in Fig. 2.3 for the 3 nm grain size case is also representative of that observed in the 2 and 4 nm grain size structures.

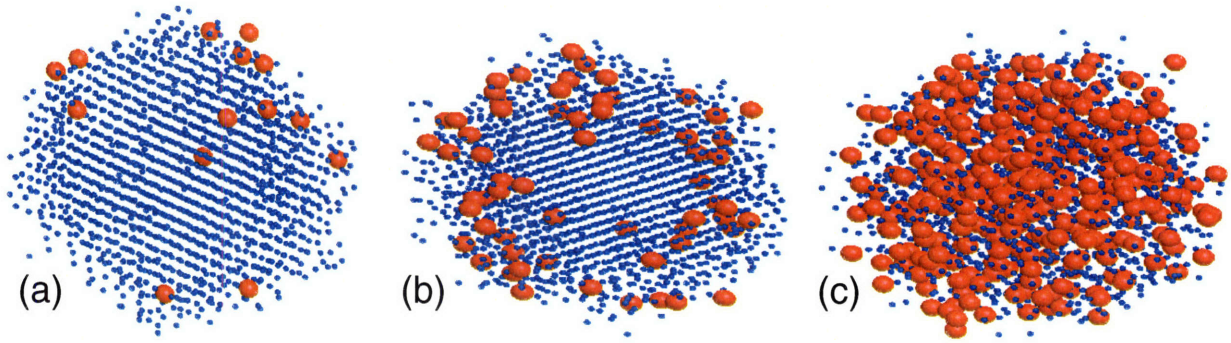

Figure 2.3: Visual representation of a single grain from the 3 nm structure, W atoms (red) are shown relatively larger than Ni atoms (blue) for clarity. In the dilute limit of (a) 1 at%W and (b) 5 at%W atoms preferentially occupy grain boundary sites while at (c) 20 at%W the structure is saturated and there is no obvious segregation tendency.

In order to quantitatively assess grain boundary segregation we next consider the spatial variation of composition within the simulated grain structure. We begin by constructing a radial composition profile using each grain center as the origin, defining a series of concentric spherical shells each containing the same total number of atoms. In Fig. 2.4(a-c) the resulting composition (normalized by the global alloy composition) is plotted as a function of position for the 2, 3, and 4 nm grain size structures; these composition profiles run from the middle of an average grain (left-most point in each plot) out to the grain boundary (right-most point). It is important to note that the data to the right of each plot are somewhat complicated by the fact that this analysis

coerces spherical symmetry onto equiaxed polyhedral grains. Still, it is clear from Fig. 2.4 not only that grain boundary segregation occurs, but that it is most pronounced in the dilute limit for all three grain sizes. As the global solute concentration increases, the relative extent of segregation to the intercrystalline regions diminishes.

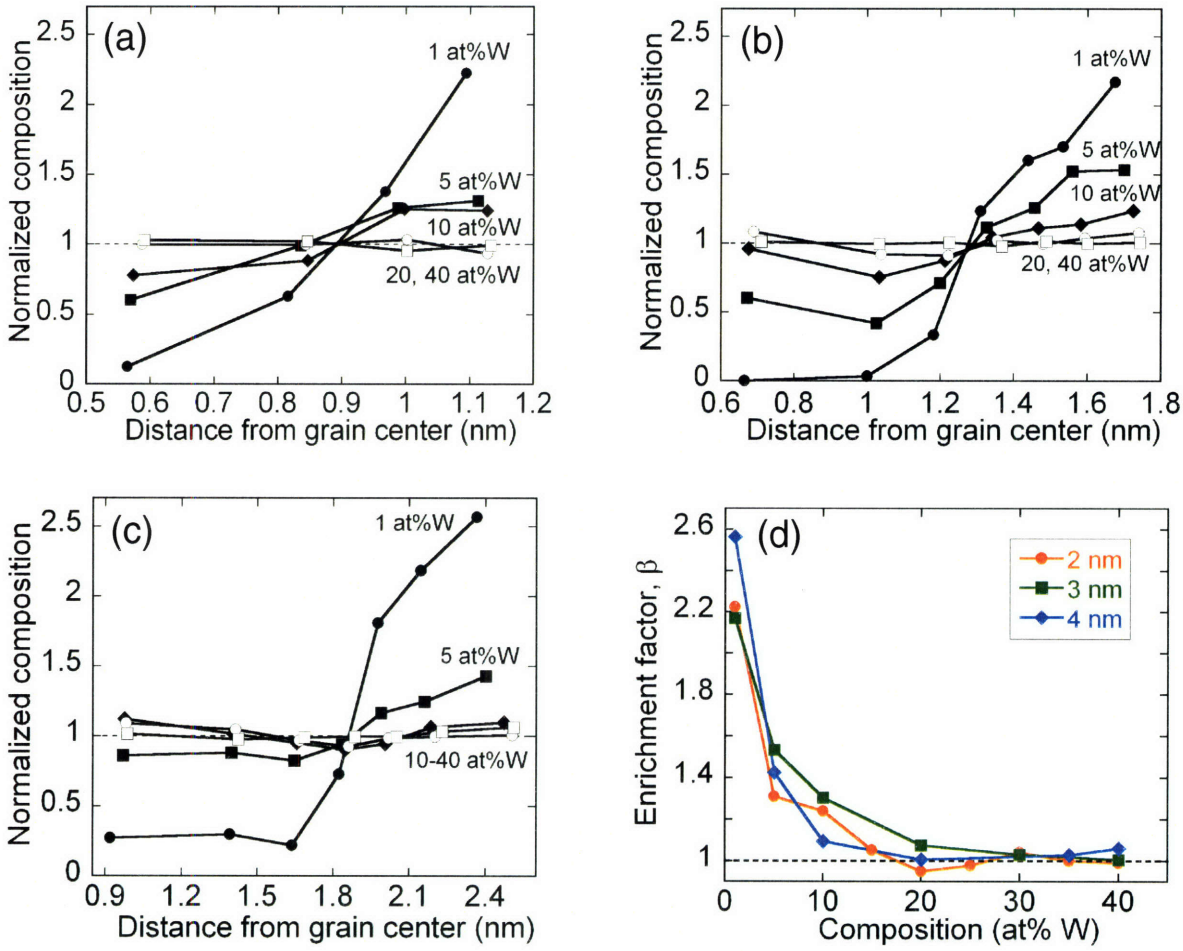

Figure 2.4: Average normalized composition plotted versus the distance from grain centers in (a) 2, (b) 3, and (c) 4 nm grain size structures at various levels of global W content: 1 at% (solid circles), 5 at% (solid squares), 10 at% (solid diamonds), 20 at% (open circles), and 40 at% (open squares). Points to the left on these plots lie in the grain interior while those to the right represent the grain boundary. (d) Compiled enrichment factor, β (grain boundary composition normalized by global composition), for all simulations; the dashed line indicates a condition of no grain boundary segregation.

The segregation behavior for all of our simulations is summarized in Fig. 2.4(d), where the enrichment factor, β, defined as the ratio of grain boundary composition to global composition

[107] (i.e., the right-most points in Fig. 2.4(a-c)) is plotted as a function of the global W content of the alloy. The dashed line in this figure at $\beta = 1$ indicates a condition with no grain boundary segregation, where composition is homogeneous throughout the structure. It is again obvious that the dilute alloys exhibit the most significant segregation while, as solute content is increased, the segregation tendency decreases with the points moving closer to the dashed line. This behavior is consistent with the qualitative conclusions drawn from the structures in Fig. 2.3 and is characteristic of a composition-dependent segregation energy, where, as energetically preferable grain boundary sites fill with solute atoms, the driving force for segregation decreases. Because of this, the dilute alloys show a high degree of segregation to the grain boundaries while a more homogeneous distribution of solute is observed as the W content increases.

2.2.2 Chemical ordering

Aside from grain boundary segregation, chemical ordering (in either the grain interior or intercrystalline regions, or both) is an additional configurational change that could account for some portion of the energy drop in Fig. 2.2. It is well established that crystalline Ni-W [108-110] and the chemically similar Ni-Mo alloys [111-113] tend to exhibit some degree of short or long range chemical ordering (depending on thermal history), and Monte Carlo simulations have reproduced experimental observations of ordering in general [114-116], and in Ni-Mo particularly [117, 118]. For the present work, we characterize short range order (SRO) or clustering using the Warren-Cowley order parameter, α_k, given as [117, 119]:

$$\alpha_k = 1 - \frac{P_k}{P_{random}} \tag{2.1}$$

where P_k is the probability of finding an unlike atom in the k'th nearest-neighbor shell about any given atomic position, and $P_{random} = 2X(1-X)$ is the probability of selecting two unlike atoms in the case of a perfectly random solid solution. A positive value of α_k denotes a preference for like atomic pairs, while negative values indicate that the system prefers unlike solute-solvent interactions. Extending the Warren-Cowley order parameter out to additional neighbor shells, k, allows one to determine the spatial extent of order in a system [117].

The order parameter α_k is plotted as a function of neighbor shell number in Fig. 2.5(a-c) for the 2, 3, and 4 nm grain size structures, over a range of compositions from 10 to 40 at%W. Here, the entire structure is considered, including both the grain interior and boundary regions, and the neighbor shells are defined to cleanly separate the distinct peaks of a radial distribution function calculated for each structure. Figure 2.5 suggests that some degree of SRO exists in all the simulated alloys, where the first (and second) nearest-neighbor shells preferentially contain unlike (and like) atomic pairs. Beyond the first and second shells these correlations decrease and the alloys exhibit a more random distribution of pair types; it is also apparent that the degree of ordering generally decreases with increasing composition, and decreasing grain size, over the range plotted here.

The non-zero values of α_k in Fig. 2.5(a-c) imply that some amount of energy reduction is derived from SRO during the simulation of our nanocrystalline structures, but with no reference state it is difficult to judge whether these values are significant. An appropriate reference is provided by our simulations on fcc single crystals of Ni-W, which permit us to separate the effects of a nanocrystalline structure on the solute distribution and alloy energetics. The Warren-Cowley order parameters calculated for the single crystal structure containing 10-40 at%W are plotted in Fig. 2.5(d). Also shown for comparison are the α_k values for the 4 nm grain size structure at 10 at%W, which corresponds to the most ordered condition observed in the nanocrystalline systems. Note that the degree of ordering in the single crystal is extensive as compared to the polycrystal, showing significantly stronger correlations in all neighbor shells considered.

The sharp contrast in chemical ordering behavior for the single crystal and nanocrystalline structures, exemplified in Fig. 2.5(d), is an important finding of the present work. Evidently, the nanocrystalline structure has a significant impact on the state of ordering that can be achieved. This behavior is reminiscent of the "surface-induced disorder" phenomenon [120-124] known to occur at free surfaces of ordered alloys, and recently suggested in simulations on alloy nanoparticles [125]. The disordering effect has been studied experimentally by Dosch et al. [121, 122], among others [120, 123], who probed the $L1_2$ ordering behavior in a Cu_3Au alloy as

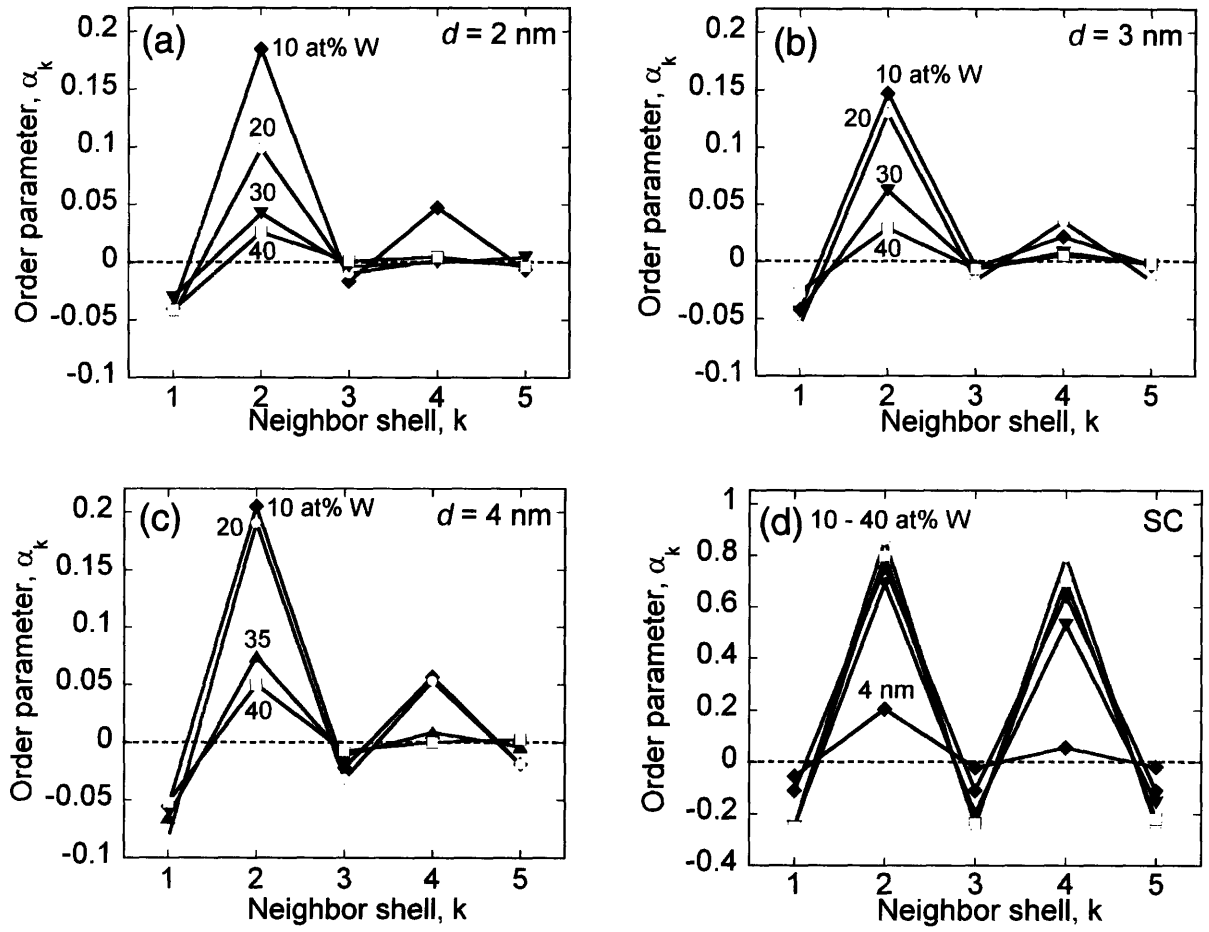

Figure 2.5: The Warren-Cowley order parameter, α_k, plotted for each nearest neighbor shell, k, in the (a) 2, (b) 3, and (c) 4 nm grain size structures over a range of global W content. In (d), the order parameter is plotted for an energy-minimized single crystal structure and the 4 nm grain size, 10 at%W data are shown for comparison. Significant chemical ordering is present in the single crystal, while it is suppressed to some extent in the nanocrystalline structures.

a function of depth from a (100) surface. Their findings were consistent with the theoretical predictions of Lipowsky [126, 127], who showed that a surface layer of chemical disorder should penetrate into the bulk with a logarithmic dependence on the critical bulk order-disorder transition temperature; even at low temperature the characteristic length-scale of the disordered region is on the order of a nanometer. Grain boundaries are internal surfaces where the atomic translational symmetry of the bulk is lost, and hence by analogy we may expect that a similar behavior, which might be termed "grain-boundary-induced disorder", may occur due to the

presence of these interfaces [128]. At temperatures well below the critical bulk order-disorder transition, this disordering effect should still significantly impact the solute distribution throughout a nanocrystalline structure.

To quantitatively evaluate the possible presence of grain-boundary induced disorder, we calculate the Warren-Cowley order parameters as a function of position within the grains. We divide the grain structure into three regions (inner, middle, and outer), where "inner" signifies the regions around the grain centers, and "outer" incorporates the intergranular regions. A typical order parameter profile resulting from this analysis is presented in Fig. 2.6 for the 3 nm grain size structure containing 20 at%W. Ordering is most pronounced in the grain interiors ("inner"), and less pronounced (more random) in the grain boundaries ("outer"). Similar results are obtained for other compositions and in the 2 and 4 nm grain size structures. To our knowledge this is the first evidence of grain-boundary induced disorder in simulated nanocrystalline alloys. This effect prevents long-range order and phase separation, and will have considerable impact on the energetics of these nanostructures.

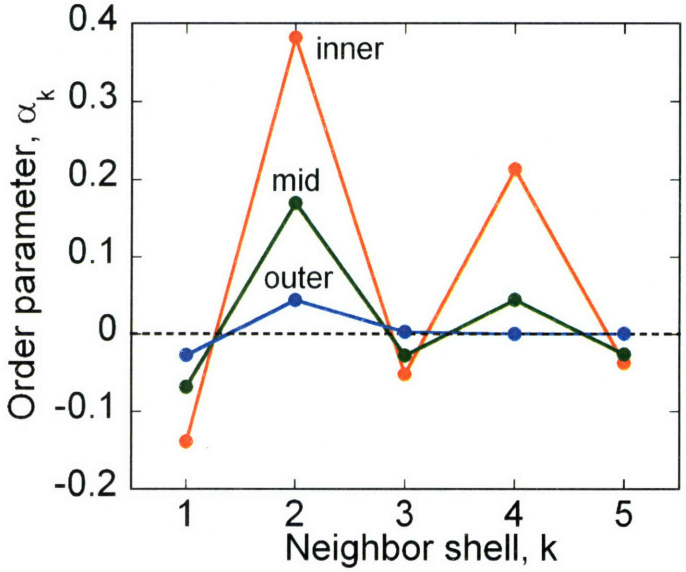

Figure 2.6: The Warren-Cowley order parameter, α_k, plotted for each nearest-neighbor shell, k, now as a function of position within the 3 nm grain size structure containing 20 at%W. "Inner" signifies the center 1/3 portion of the grain, and "mid" and "outer" indicate a progression towards the grain boundary region. The greatest degree of ordering is seen in the center, crystalline region of the grains while the grain boundaries appear to induce disordering.

2.3 Energetics of segregation and ordering

In the previous section we concluded that solute segregation to the grain boundaries in nanocrystalline Ni-W is most pronounced in the dilute limit, and becomes increasingly subtle with alloying addition. We also observed a degree of SRO, where unlike (and like) atomic pairs are preferred in the first (and second) nearest neighbor shell as compared to a random solid solution, and where more extensive long-range ordering is apparently suppressed by the high density of grain boundaries in the nanocrystalline structure. In this section we will evaluate the energetic consequences of both solute segregation and ordering, and attempt to link this evaluation to existing thermodynamic models of nanostructure stability. In particular, we evaluate the segregation energy, H_{seg}, and grain boundary energy, γ, for nanocrystalline Ni-W structures as a function of composition and grain size.

2.3.1 Segregation energy

The quantity H_{seg} can be defined as the difference in energy between a solute atom in the crystalline grain interior and in the grain boundary [107, 129]; a positive value indicates that the system energy may be lowered if solute atoms preferentially occupy intercrystalline sites. In our earlier discussion we proposed that a composition-dependent H_{seg} may explain the data in Fig. 2.4; a high positive value is expected in the dilute limit where segregation is most pronounced, followed by decreasing H_{seg} as W content increases and the entire structure becomes saturated. Here, we quantitatively evaluate H_{seg} as a function of composition following a technique described by Rittner et al. [130], who used Monte Carlo simulations to determine the equilibrium solute distribution for simple tilt grain boundary configurations in the Pt-Au system. By measuring the equilibrium composition in grain interior and grain boundary regions, Rittner et al. calculated H_{seg} from the McLean isotherm [107, 129], given by:

$$\frac{X_{gb}}{1-X_{gb}} = \frac{X_g}{1-X_g}\exp\left[\frac{H_{seg}}{RT}\right] \tag{2.2}$$

where X_{gb} and X_g are the composition of the grain boundary and grain interior, respectively. Classically, X_g is assumed to be approximately equal to X (global solute concentration) in coarse-grained polycrystals where the volume fraction of intercrystalline regions is negligible. In nanocrystalline materials, however, this volume fraction can be significant and may actually exceed that of the grain interior [20]; in this case, the composition X_{gb} will strongly influence X and the assumption that $X \approx X_g$ is no longer valid. In light of this, Ishida [131] introduced a rule-of-mixtures, $X = f_g X_g + f_{gb} X_{gb}$, into the McLean equation (Eq. (2.2)) to incorporate grain size effects in the nanocrystalline regime, where f_g and f_{gb} are given by Eq. (1.1). Introducing Ishida's rule-of-mixtures relationship into Eq. (2.2) and simplifying we obtain a grain-size-dependent segregation isotherm:

$$\frac{X_{gb}}{1-X_{gb}} = \frac{X_{gb}(3d^2 - 3dt + t^2) - Xd^3}{(1-X_{gb})t(3d^2 - 3dt + t^2) - (1-X)d^3} \exp\left[\frac{H_{seg}}{RT}\right] \tag{2.3}$$

We use Eq. (2.3) to calculate H_{seg} as a function of X from the simulation data, by taking the grain boundary composition, X_{gb}, from Fig. 2.4(d) for each simulation of global composition X. A plot of H_{seg} extracted from the 2, 3, and 4 nm grain size structures is presented as Fig. 2.7 along with a least-squares fitted exponential function shown for purposes of visualization, and to be used in later analysis. (Note that several of the $d = 2$ nm data points at higher W content have not been included in this plot where values of $\beta \leq 1$ (Fig. 2.4(d)) prohibit a reasonable analysis of H_{seg}, which must be near zero in these cases.)

The calculations in Fig. 2.7 quantitatively show that H_{seg} is strongly composition-dependent in the Ni-W system, decreasing sharply with alloying addition from a maximum value in the dilute limit of ~10 kJ/mol. This behavior is reminiscent of the classical Fowler-Guggenheim segregation isotherm [107], which approximately accounts for solute-solute interaction effects that decrease the driving force for segregation beyond the dilute limit. However, the exponential

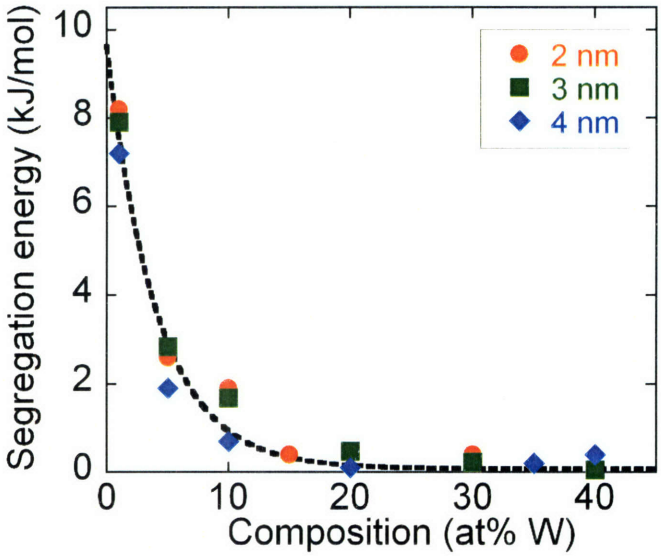

Figure 2.7: Segregation energy, H_{seg}, for simulated Ni-W alloys with 2, 3, and 4 nm grain size plotted as a function of global composition. An exponential decrease is observed with alloying addition due to solute-solute interactions in the grain boundaries.

form for H_{seg} in Fig. 2.7 is somewhat different from the linearly-decreasing trend in the Fowler-Guggenheim isotherm; this is likely due to the use of multibody potentials in the present work, leading to a more accurate H_{seg} calculation as compared to the nearest-neighbor pairwise interactions assumed in the Fowler-Guggenheim model.

A composition-dependent H_{seg} as derived above has not yet been considered in thermodynamic models for nanostructure stability, such as those of Weissmuller [44] or Kirchheim et al. [45, 46]. Instead, these models have generally assumed a high constant value of $H_{seg} \approx 50-100$ kJ/mol over the entire range of alloying addition. Even in the dilute limit, the Ni-W value of 10 kJ/mol from Fig. 2.7 is only a fraction of that previously assumed, reflective of the much higher solubility of W in Ni, leading to a lower segregation tendency. The implications of these vastly different segregation energies on the potential for nanostructure stabilization will be discussed later on in Chapter 4.

2.3.2 Grain boundary energy

As mentioned in the introduction, vanishing grain boundary energy ($\gamma = 0$) is an underlying assumption in several proposed models of nanostructure stabilization [44-46]. Therefore, it is instructive to extract this quantity from the present simulations to determine if $\gamma = 0$ can be realized in nanocrystalline Ni-W. Grain boundary energy can be calculated from our simulations by comparing a structure containing boundaries to an ideal structure containing no defects (at the same global composition); γ is then the excess energy, normalized by the total area of grain boundaries:

$$\gamma = \frac{\Delta E_f^{defect} - \Delta E_f^{ideal}}{A_{defect}} \tag{2.4}$$

where ΔE_f^{defect} and ΔE_f^{ideal} are the formation energies of the polycrystal and the ideal single crystal, respectively, and A_{defect} is the total grain boundary area [119, 132, 133]. The formation energies in Eq. (2.4) are defined by [119]:

$$\Delta E_f = E_{alloy} - \left[(1 - X) \cdot E_{Ni} + X \cdot E_W\right] \tag{2.5}$$

where E_{alloy} is the energy per atom of an alloyed structure, and E_{Ni} and E_W are the energies of pure Ni and pure W, respectively, fully relaxed and with the same crystal structure as the alloy. The values of E_{Ni} and E_W have been determined in the present work by simulating pure fcc single crystals of Ni or W, at zero pressure.

For pure metals the calculations in Eqs. (2.4) and (2.5) are fairly straightforward, but in alloys an additional complication arises due to the possibility of chemical ordering. In particular, an appropriate reference state (from which ΔE_f^{ideal} is calculated) must be chosen to account for the energetics of ordering in multicomponent systems. For example, when calculating the grain boundary energy of an intermetallic phase [132, 134], the reference state is a single crystal with

the same ideal long-range order of the intermetallic. For the present case, we have found that extensive ordering of Ni-W is disrupted by the nanocrystalline structure (cf. Fig. 2.5(d)) and, therefore, we propose that a fully-ordered structure is an inappropriate reference state. Using a fully-ordered reference, such as the single crystal simulations in Fig. 2.2(b), yields unrealistically high grain boundary energies as W is added to the system. Instead, we use an ideal reference structure that exhibits the same degree of chemical ordering as the polycrystal, so that the numerator in Eq. (2.4) accounts for the excess energy due to the polycrystalline structure alone, and not a change in the state of chemical order. To reach this ideal reference state, we have performed simulations on single crystal structures where the Monte Carlo procedure was altered to iterate to the α_k values shown in Fig. 2.5(a-c), rather than to a minimum energy.

A plot of ΔE_f^{defect} for the 2, 3, and 4 nm grain size structures in the energy-minimized state (after the Monte Carlo procedure) is presented in Fig. 2.8(a). Also shown are the single crystal ΔE_f^{ideal} values corresponding to the same extent of SRO for each of the polycrystals. It is clear that the single crystal structures are in each case the lower energy state as compared to their corresponding nanocrystalline form. Furthermore, within the scatter of the data, it is generally found that larger grain sizes are preferred over the entire range of alloying addition. This suggests that nanocrystalline Ni-W structures are not thermodynamically stable; grain boundaries must still represent an energy penalty to the system with $\gamma > 0$.

From the above discussion and the values of ΔE_f^{defect} and ΔE_f^{ideal} in Fig. 2.8(a) we can now calculate the numerator in Eq. (2.4). However, A_{defect} remains a quantity that is not trivial to calculate given the complex 3-dimensional nature of the structures. A simple method to determine A_{defect} is by calculating ΔE_f^{defect} and ΔE_f^{ideal} for the random solid solution polycrystals and then calibrating to the known γ of pure Ni (0.87 J/m^2 [135]) using Eq. (2.4). The values of A_{defect} extracted in this way are in line with those estimated from a simple geometric construction, assuming spherical grains and using Eq. (1.1) to calculate grain boundary area. For the case of pure Ni, this geometric analysis yields grain boundary areas of 77.7, 193, and 361

nm^2 while the method outlined above, using Eq. (2.4), gives 91.3, 183, and 246 nm^2 for the 2, 3, and 4 nm structures, respectively.

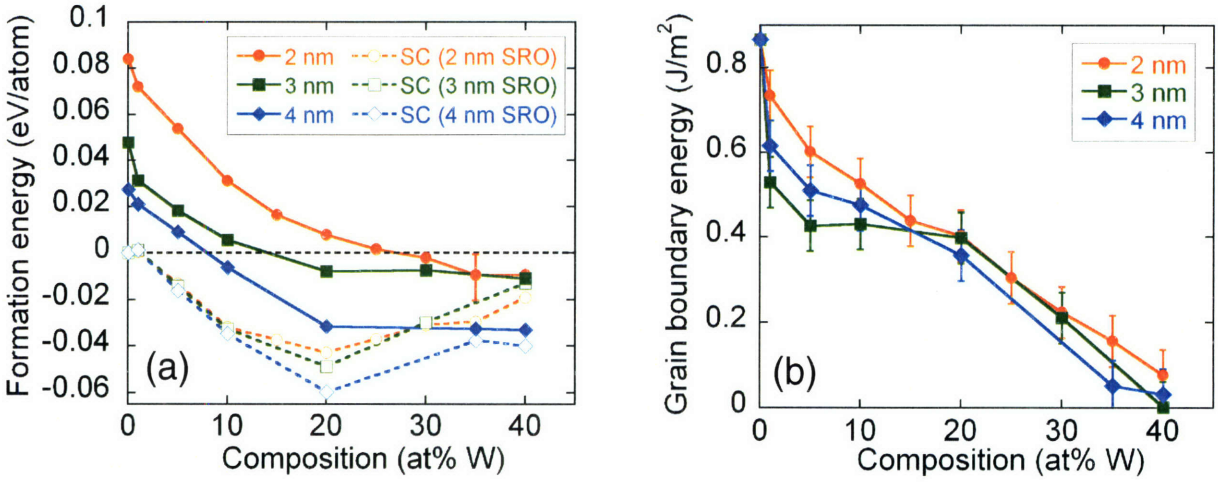

Figure 2.8: (a) Formation energy in the fully relaxed state after Monte Carlo simulation for the 2, 3, and 4 nm grain size structures (ΔE_f^{defect}) along with the corresponding single crystal ("SC") energy (ΔE_f^{ideal}) having the same degree of short-range order as the polycrystal in each case; typical error on this measurement is shown for the 2 nm, 35 at%W point. (b) Grain boundary energy, γ, calculated for the 2, 3, and 4 nm grain size structures using Eq. (2.4) with the ΔE_f^{defect} and ΔE_f^{ideal} values from (a). A general decrease in energy is observed in all cases; however, all data lie above $\gamma = 0$ suggesting that nanocrystalline Ni-W structures are not thermodynamically stable.

With an estimate for A_{defect}, along with the values of ΔE_f^{defect} and ΔE_f^{ideal} from the Monte Carlo simulations, we calculate γ using Eq. (2.4) for the energy-minimized 2, 3, and 4 nm grain size structures as a function of W content. These values are plotted in Fig. 2.8(b) where it is seen that γ generally decreases with W addition. Here, the composition-dependent H_{seg} (Fig. 2.7) and subtle amount of grain boundary segregation (Fig. 2.4) in the Ni-W system are naturally included. Several interesting features can be seen in Fig. 2.8(b). First, the most dramatic decrease in γ with alloying addition occurs in the dilute limit, where the extent of segregation is the greatest (Fig. 2.4). Second, while there is a significant reduction in γ for all grain sizes, none cross $\gamma = 0$ over the range of compositions considered. Lastly, within the scatter of this analysis, the grain boundary energies for the 2, 3, and 4 nm grain size structures appear to be similar at every composition, especially at higher W contents.

2.4 Concluding remarks

This chapter has focused on atomistic computer simulations as a means to investigate the equilibrium solute distribution and associated energetics in nanocrystalline Ni-W alloys. In particular, we have evaluated the grain boundary segregation tendency and chemical ordering behavior for 2, 3, and 4 nm grain size structures over a range of compositions from 1-40 at%W, with the following main conclusions:

- The extent of W segregation to intercrystalline regions is most pronounced in the dilute limit, and decreases with increasing solute content.
- Short range chemical ordering occurs in all nanocrystalline structures, but to a degree less than that achieved in ideal single crystals. This suppression of chemical ordering becomes more pronounced as the density of grain boundaries increases (i.e., grain size decreases), an effect termed "grain boundary induced disorder" analogous to the well-known "surface-induced disorder" effect.

In addition, several relevant energetic quantities were extracted from our simulations with the main goal of relating these to thermodynamic models of nanostructure stability. Specifically, segregation, formation, and grain boundary energies were evaluated, revealing that:

- Segregation energy decreases exponentially with W addition from a dilute limit value of ~10 kJ/mol, owing to solute-solute interactions in the grain boundaries.
- Formation energy calculations predict that nanocrystalline Ni-W alloys become more stable with increasing grain size, with ideal single crystal structures maintaining the lowest overall energy state for any given composition.
- Grain boundary energy decreases significantly with solute addition in nanocrystalline Ni-W.

Based on the prediction of significant grain boundary energy reduction in nanocrystalline Ni-W (Fig. 2.8(b)), it is reasonable to suspect that nanostructure stabilization may occur in this system. In the next chapter we investigate this possibility through experiments in electrodeposited Ni-W alloys. Our main goal will be to develop precise control over alloy composition in order to investigate relationships with grain size.

Chapter 3: Experimental synthesis of nanocrystalline Ni-W

Electrodeposition offers one of the most promising routes to fabricate bulk, full-density, high purity nanocrystalline materials. A number of researchers have used this method to synthesize nanocrystalline Ni-W with the goal of producing high quality specimens of the finest possible grain sizes. These works may be categorized according to two general themes: fundamental electrochemical studies [136-145], and structure/property investigations [31, 95, 146-161]. In the former category, researchers study the effects of various deposition parameters on the electrochemical response of the plating process, as well as the atomic-level mechanisms of the deposition reaction. Structure/property investigations, on the other hand, are more concerned with the net result of the electrodeposition process, linking the as-deposited microstructure to macroscopic property measurements. In this chapter we bridge these two approaches, establishing a means to tailor the as-deposited microstructure through manipulation of the deposition parameters. In what follows, we first introduce the electrodeposition and characterization procedures, followed by an investigation of some key variables having significant effects on the deposit composition. Composition, in turn, is linked to the microstructure through several experimental techniques and discussed in terms of the thermodynamics of nanostructure stability. Connecting these observations, we present a new method to precisely control nanocrystalline grain size over a wider range than previously possible. Some of the work presented in this chapter has been published in Ref. [162].

3.1 Electrodeposition procedures

A schematic of the electrodeposition set-up used in the present work is presented as Fig. 3.1, consisting of a cathode (substrate) and anode submerged in an electrolyte bath and connected to a power supply (Dynatronix model # PDPR 40-50-100 or DPR 20-30-100). The electrolyte is continuously stirred and maintained at a prescribed temperature via a heated oil bath. There are a number of variables that can be controlled in this process including, most notably: electrolyte bath composition, rate of stirring, substrate/anode material, bath temperature, and applied current/voltage waveform. For the present work we have maintained several of these variables constant. In particular, we have used commercial purity copper sheet as the substrate (~12 cm^2

area, polished to a mirror finish) and pure platinum mesh as the inert anode for all experiments. The electrolyte bath has been stirred at a rate of ~100 RPM and maintained at the composition given in Table 3.1. This ammoniacal citrate bath is one of the most common used in the literature for Ni-W deposition [31, 95, 136, 148, 149], containing nickel sulfate and sodium tungstate as metal sources, with sodium citrate and ammonium chloride acting as complexing agents to induce the co-deposition of Ni and W [31, 136]; sodium bromide is added here to increase the conductivity of the plating bath. The remaining variables of bath temperature and applied current waveform have been studied in detail in the present work and will be discussed in sections 3.3 and 3.4, respectively. In the next section we introduce the characterization procedures used to assess the composition, quality, and structure of the as-deposited specimens.

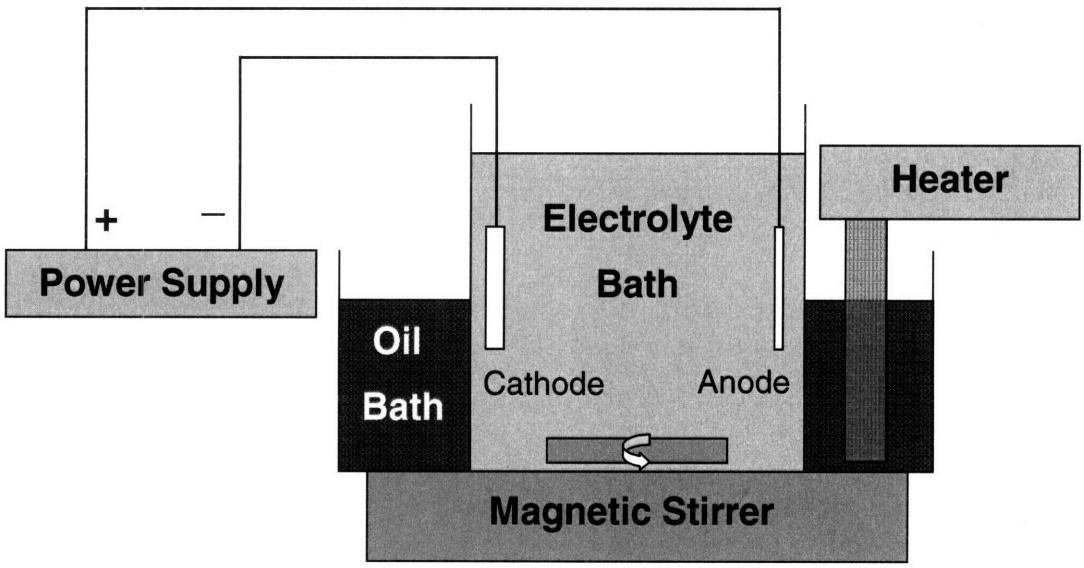

Figure 3.1: Schematic diagram of the electrodeposition set-up used to synthesize nanocrystalline Ni-W alloys.

Table 3.1: Electrolyte bath composition used for all electrodeposition experiments, after Yamasaki et al. [31]

Chemical Name	Formula	Concentration (g/L)
Nickel sulfate hexahydrate	($NiSO_4 . 6H_2O$)	15.8
Sodium tungstate dihydrate	($Na_2WO_4 . 2H_2O$)	46.2
Sodium citrate dihydrate	($Na_3C_6H_5O_7 . 2H_2O$)	147.1
Ammonium chloride	(NH_4Cl)	26.7
Sodium Bromide	(NaBr)	15.4

3.2 Characterization procedures

Following deposition, specimens were sectioned and prepared via traditional metallographic techniques for examination in a Leo 438VP scanning electron microscope (SEM) to gather quantitative information on composition to within ± 1 at% via energy dispersive spectroscopy (EDS) (X-ray Optics/AAT). Cross-sectional examination in the SEM also allowed for direct measurement of specimen thickness and inspection of any possible microscopic flaws (i.e. cracking, porosity, inclusions, etc.). Structural characterization was conducted via X-ray diffraction (XRD), as well as transmission electron microscopy (TEM). The X-ray diffraction measurements were performed on a Rigaku RU300 operating at 300 mA and 60 kV, and peak analysis (including phase identification) was conducted using the software package Jade. An approximate grain size was quantified from the XRD data by applying the integral breadth method to the {111} family of peaks after removing the instrumental broadening effect; this method has been shown to provide reasonable nanocrystalline grain size measurements as it approximately accounts for both microstrain and crystallite size contributions to peak broadening [163]. Direct observation of the structure was conducted by TEM investigations in a JEOL 2010 operating at 200 kV using traditional bright field imaging and selected area diffraction techniques. TEM specimens were prepared via twin-jet electropolishing at 10 V in a 2:1 solution of methanol and nitric acid at a temperature of -60 °C. Several specimens were further thinned in a Fischione 1010 Ion Mill operating at 4 kV and 5 mA, at a milling angle of 12°.

A complete set of all experiments performed at various bath temperatures and applied current waveforms is presented as Appendix A, along with the resulting composition and grain size extracted through the above techniques. A select set of these experiments, as noted, will be discussed in the following sections to determine the important effects of bath temperature and current waveform on the composition and structure of the deposits.

3.3 Effect of electrolyte bath temperature

Measurements of specimen composition are plotted as a function of electrolyte bath temperature in Fig. 3.2. A linear trend is observed in this figure with composition increasing from ~9-26 at%W over a temperature range of 45-85 °C; note that all other variables are kept constant

including the direct current (D.C.) density of 0.2 A/cm^2. These results are consistent with the work of Yamasaki et al. [31] and Giga et al. [149] who have found similar trends, although the present study extends to lower bath temperatures.

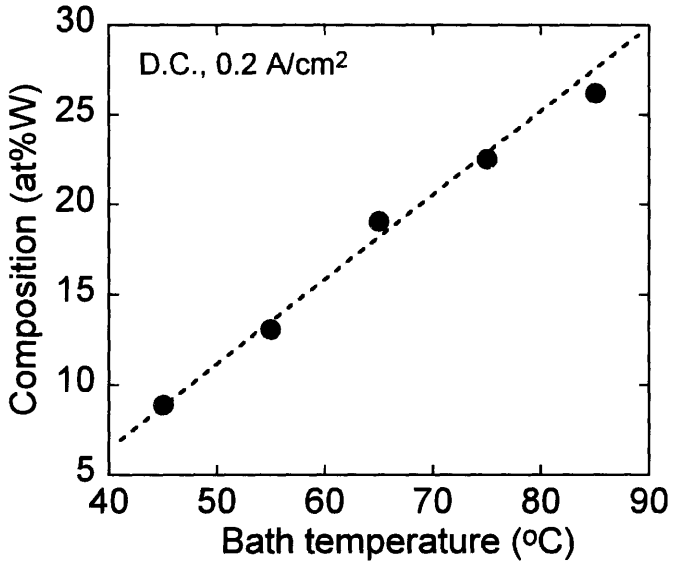

Figure 3.2: Effect of bath temperature on the composition of electrodeposited Ni-W alloys. A constant direct current density of 0.2 A/cm^2 has been applied for all experiments.

The electrochemical mechanism behind the observed temperature dependence in Fig. 3.2 has received only limited attention in the literature. Atanassov et al. [139], who studied a similar bath composition having the same W complex as the present case [136], also noted an increase in W composition with bath temperature. They attributed this increase to a transport phenomenon in the electrolyte, where higher temperatures promote diffusion of the (slow) W complex in solution. Hence, in this diffusion controlled scenario, higher temperatures enable more W ions to reach the cathode surface, resulting in higher W content in the deposit. Regardless of the exact electrolytic mechanism, which is not the primary focus of this work, the relationship between W content and bath temperature in Fig. 3.2 suggests a systematic method to investigate composition-structure relationships. Unfortunately, as we will address in the next section, quality issues plague specimens deposited at temperatures below ~65 °C, such that an alternative means of composition control is required for reliable property investigations and applications.

3.4 Effect of applied current waveform

Current controlled (galvanostatic) electrodeposition techniques can be divided into three unique groups based on the shape of the applied waveform: direct, unipolar pulsed, or bipolar pulsed. The first of these has received by far the most attention in the literature and simply involves the application of a fixed current over the entire duration of the deposition experiment. Unipolar pulsing incorporates some periodic "off-time" that can range anywhere from a millisecond to several seconds or more where no current is applied to the system. This interruption of the current has been suggested to have a number of important effects on the formation of nanocrystalline structures [164] and has been used successfully in a variety of systems including Ni [164-167], Cu [168], Zn [169, 170], Ni-Cu [166], and Ni-Mo [171, 172] to name a few. Bipolar pulsing involves some periodic reverse current in the electrodeposition process, typically on the time scale of milliseconds, where the anode and cathode are effectively "switched" by definition. The schematic in Fig. 3.3 defines the variables that control the shape of the bipolar waveform as presented in Appendix A: forward and reverse current density (Fwd C.D. and Rev C.D., respectively), forward and reverse on-time (Fwd t_{on} and Rev t_{on}, respectively) and off-time (t_{off}). Here, off-time is always applied directly after the forward pulse. The introduction of

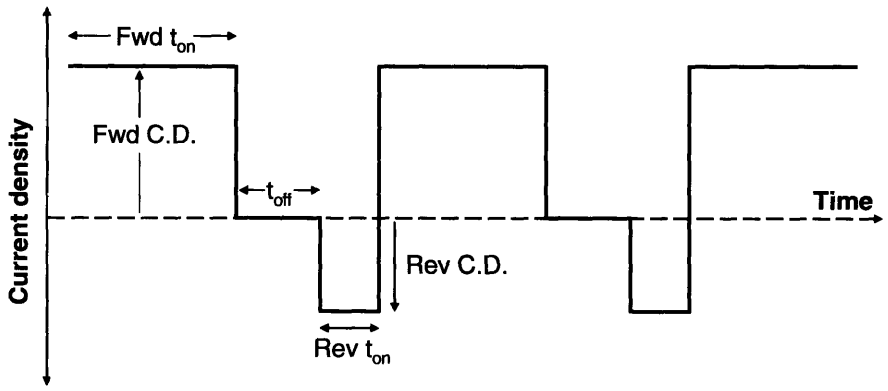

Figure 3.3: Definition of variables that control the shape of the applied current waveform used in electrodeposition experiments.

bipolar pulsing has received relatively little attention in the literature with several studies suggesting that a reverse pulse may effectively strip unwanted elements such as hydrogen from incorporating in the deposit [173], or reduce stress levels [174] or surface roughness [175, 176]. To our knowledge, the effect of a bipolar waveform has not been investigated in the

electrodeposition of Ni-W alloys whereas most studies to date have involved only direct current. In what follows we present a series of experiments investigating the effect of reverse pulse current density (Rev C.D.) and reverse pulse time (Rev t_{on}) on the deposit composition (noted as 'b' and 'c' in Appendix A, respectively).

The relationship between composition and reverse pulse current density is plotted in Fig. 3.4(a). All other variables as defined in Fig. 3.3 are fixed in these experiments as: Fwd C.D. = 0.2 A/cm^2, Fwd t_{on} = 20 ms, t_{off} = 0, and Rev t_{on} = 3 ms; an exception is for the deposition at 0 Rev C.D. which was deposited under direct current (i.e. Rev t_{on}=0). It is apparent that an increase in the intensity of the reverse pulse leads to a monotonic decrease in W content. Similarly, Fig. 3.4(b) plots the effect of the reverse pulse duration (Rev t_{on}) on deposit composition, where the remaining variables are fixed at: Fwd C.D. = 0.2 A/cm^2, Fwd t_{on} = 20 ms, and Rev C.D. = 0.05 A/cm^2. Here, an increase in the duration of the reverse pulse leads to a decrease in W content. Based on these observations, it is evident that composition is directly dependent on the time-integrated intensity of the reverse pulse; increases in either intensity or duration lead to reduced levels of W incorporation in the deposit.

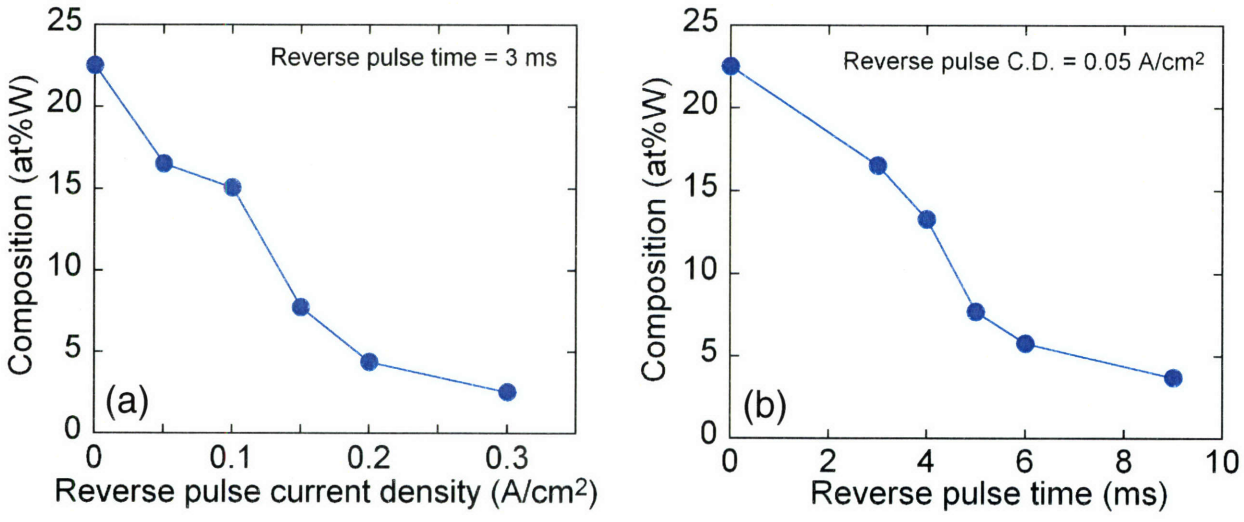

Figure 3.4: Effect of reverse pulse (a) current density and (b) time on bulk deposit composition. Reverse pulsing is an effective means for controlling W content in the range of ~2 – 23 at%.

From an electrochemical standpoint, it has been suggested that specific elements may be preferentially stripped from the cathode surface with reverse pulses that are targeted in an appropriate potential range [173]. In the present work we have not studied the electrochemistry in detail, but may gain some insight on the reverse pulsing mechanism by referring to standard reduction potentials available in the literature [177, 178]. During electrodeposition, reactions with a higher (more positive) reduction potential occur preferentially, with later reactions commencing only if the necessary over-voltage is applied [179]. This type of behavior is typically presented in electrochemical experiments as a current-potential curve for each of the possible reactions, forming the basis for understanding alloy electrodeposition. Table 3.2 lists standard reduction potentials for ions expected in the present Ni-W electrolyte (cf. Table 3.1): WO_4^{2-}, H^+, and Ni^{2+} [177, 178]. Several interesting conclusions can be drawn from this data. First, according to Table 3.2, pure Ni should deposit preferentially (along with hydrogen evolution), and any appreciable amount of W deposition would require extremely high over-voltages. In fact, it is common knowledge that W cannot be deposited in pure form from aqueous solutions [137, 177, 180, 181] partly due to the low reduction potential listed in Table 3.2. However, as mentioned previously, sodium citrate and ammonium chloride are introduced

Reaction	Standard potential, E° (volts vs. SHE)
$2H^+ + 2e^- \Leftrightarrow H_2$	0.0
$Ni^{2+} + 2e^- \Leftrightarrow Ni$	- 0.257
$WO_4^{2-} + 4H_2O + 6e^- \Leftrightarrow W + 8OH^-$	- 1.074

Table 3.2: Standard reduction potentials for WO_4^{2-}, H^+, and Ni^{2+} ions. The equilibrium values suggest that W is preferentially stripped from the deposit surface during the reverse (anodic) pulse.

in the present plating bath as complexing agents, whose function is to bring the reduction potentials of Ni and W closer together. This processes is termed "induced codeposition" [181] and enables the present Ni-W alloy to be formed. Second, during the application of the reverse (anodic) pulse, the data in Table 3.2 suggest that W should be preferentially stripped from the deposit surface, as this reaction has the highest *oxidation* potential. While the details of these

electrochemical phenomenona are not the main focus of this thesis, comparing the equilibrium reduction potentials provides some qualitative insight on the deposition process, and the possible mechanism involved in reverse pulsing. This area represents an important avenue for future work.

Regardless of the specific electrochemical mechanism, the dissolution of W is apparently proportional to the intensity or duration of the reverse pulse, leading to the trends observed in Fig. 3.4(a, b). Thus, reverse pulsing presents an alternative method to tailor alloy composition in the Ni-W system over the wide range from ~2-23 at%W. Before proceeding, it is important to note that the millisecond timescale of pulses used in the present work essentially provide for monolayer control of W content. Therefore, the resulting composition may be regarded as homogeneous through thickness and the values reported represent bulk measurements.

In comparison to bath temperature control, the reverse pulsing technique described above is found to yield high quality deposits over the entire range of composition. This is demonstrated in the cross-sectional SEM micrographs of Fig. 3.5 for specimens deposited by (a) bath temperature and (b) reverse pulsing control. The W content of both these specimens is roughly 8 at%, achieved in (a) through a low bath temperature of 45 °C (cf. Fig. 3.2) and in (b) through the

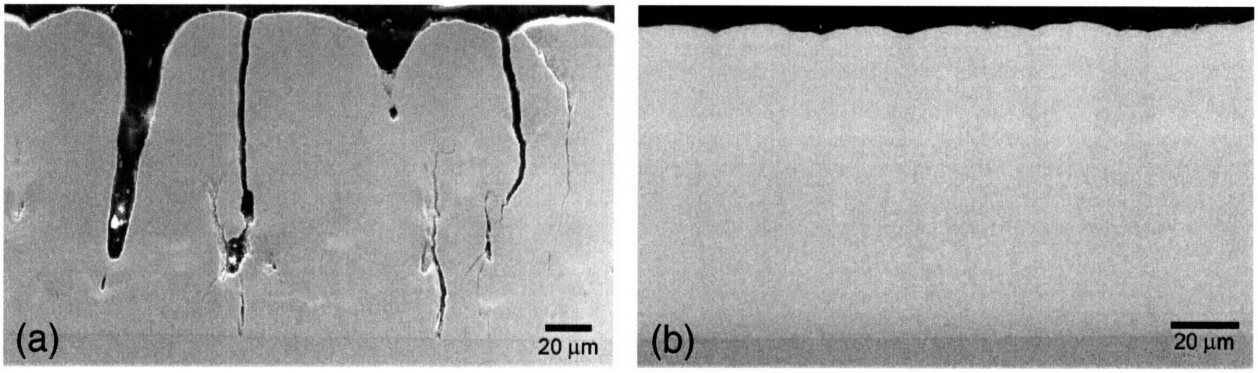

Figure 3.5: Cross-sectional SEM micrographs of nanocrystalline Ni-W specimens prepared by (a) bath temperature and (b) reverse pulsing control; both specimens have nominally the same composition of ~8 at%W. The specimen in (a) was produced at a plating bath temperature of 45 °C (cf. Fig. 3.2) while that in (b) was deposited at 75 °C using a reverse pulse current of 0.15 A/cm^2 (cf. Fig. 3.4(a)). Significant defects are observed in (a) while the (b) reverse pulsing technique yields a high quality deposit. The substrate can be seen at the bottom of both images.

application of a 0.15 A/cm^2 reverse pulse (cf. Fig. 3.4(a)). It is apparent that the bath temperature technique leads to a number of defects in the form of voids and extensive cracking; most deposits synthesized at bath temperature below ~65 °C show these types of flaws. On the other hand, the deposit in (b) shows no defects and is typical of the high quality achieved using the reverse pulsing method.

With the above information, the reverse pulsing technique stands out as a robust means to tailor the composition of Ni-W specimens. Not only can a wide range of W contents be accessed through systematic changes to the applied current waveform, but the resulting deposits are of excellent quality. In the next section we investigate the structure of the electrodeposited specimens through XRD and TEM techniques and make correlations with composition.

3.5 Composition-structure relationship

As a preliminary investigation of the microstructure, X-ray diffraction patterns are presented in Fig. 3.6 for each of the specimens in Fig. 3.4(a), where composition has been tailored through the reverse pulse current density. Several trends can be observed as the W content of the deposit increases. First, the crystal structure is unchanged with composition; all of the peaks in Fig. 3.6 can be indexed with fcc reflections, as expected for Ni-rich solid solutions. It is interesting to observe that W is dissolved to levels much higher than nominally expected from the equilibrium phase diagram (which indicates a solubility limit near 12 at% at low temperatures [96]). Second, the addition of W clearly leads to substantial peak broadening, which is quantified through the trend of decreasing grain size reported at the right of Fig. 3.6. Finally, an increase in W content leads to a clear shift of the FCC reflections to lower Bragg angles; this is consistent with lattice swelling due to the relatively large size of W atoms in solution.

The relationship between grain size and composition revealed in Fig. 3.6 is reminiscent of that expected for alloys stabilized by grain boundary segregation, as discussed in the introduction with reference to Fig. 1.4. These alloys exhibit a monotonically decreasing trend in grain size with increasing solute addition due to the energetics of segregation and, in particular, the relationship between the total number of solute atoms and grain boundary sites available in the system. Higher concentrations of solute prefer finer grain sizes so as to be accommodated with a

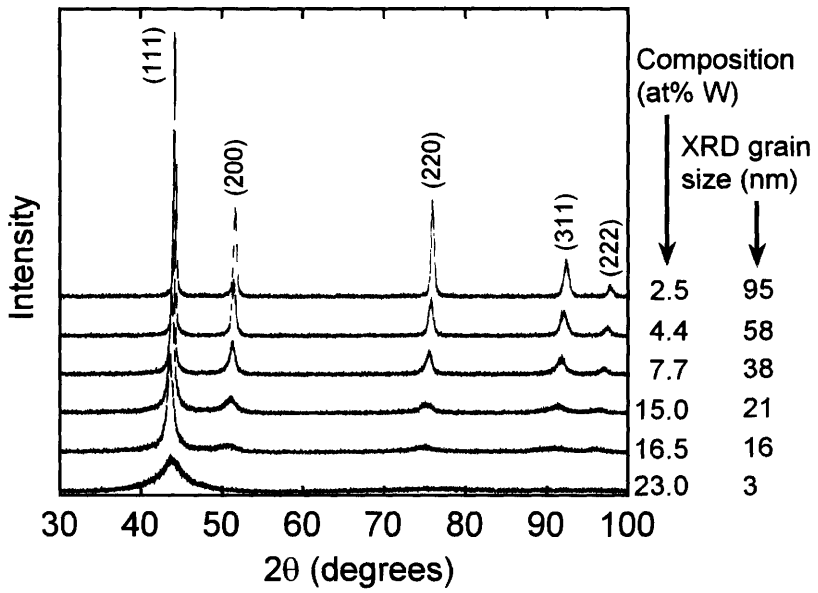

Figure 3.6: Typical X-ray diffraction patterns for specimens produced using the reverse pulsing technique in Fig. 3.4(a) with global W content from 2.5 – 23.0 at%. The XRD grain size calculated using the integral breadth method is shown for each specimen.

lower energy penalty in the intercrystalline regions. To further examine this trend in Ni-W, Fig. 3.7 plots grain size as a function of composition for all the experiments listed in Appendix A. Note that we distinguish the experiments here according to those that involved reverse pulsing ('RP', blue squares) or those that were deposited under "conventional" uni-polar or direct current conditions ('C', red circles). The first important observation here is that, irrespective of the processing technique, grain size generally scales monotonically with composition, decreasing from ~140-2 nm over the range of ~2-26 at%W, respectively. This finding implies that grain size is dictated by bulk composition alone, rather than the specific details of the synthesis conditions. Second, the reverse pulsing technique enables larger grain sizes to be accessed in high quality specimens. In fact, the range of grain sizes presented in Fig. 3.7 is wider than any previously reported in nanocrystalline Ni-W alloys; this will prove to be an important advantage in later property studies.

The grain sizes quantified in Fig. 3.7 were all measured indirectly using XRD techniques. To confirm these measurements, direct structural observations were made on select samples using TEM (as noted in Appendix A). Three bright-field images and selected area diffraction patterns

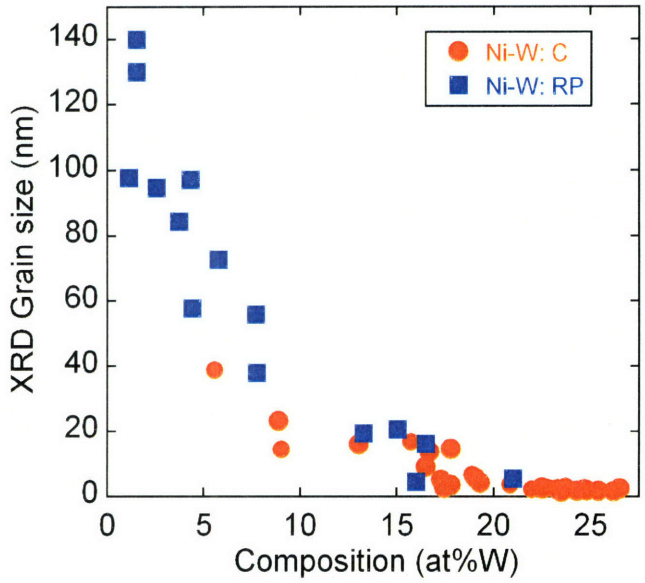

Figure 3.7: Grain size-composition relationship for nanocrystalline Ni-W specimens electrodeposited using reverse pulsing (RP) and conventional (C) techniques. The range of grain sizes achievable using reverse pulsing extends that of conventional methods.

from these investigations are presented in Fig. 3.8(a-c) for specimens containing ~3, 15, and 23 at%W, respectively; Fig. 3.8(d) reproduces Fig. 3.7 for reference. The images in Fig. 3.8(a) and (b) reveal average grain sizes of approximately 100 and 20 nm, respectively; these values are in line with those approximated by the XRD line broadening measurements which gave 95 and 21 nm for specimens of similar respective composition (see Fig. 3.6). Fig. 3.8(c) is a high resolution TEM image where lattice fringes can be seen for individual grains with appropriate orientations, two of which have been circled. The individual grains visible here are all about 2-4 nm in diameter, which again correlates well with the XRD measurement (~3 nm). Together, the series of micrographs in Fig. 3.8(a-c) confirm that a clear refinement of the nanocrystalline structure occurs with increasing W content.

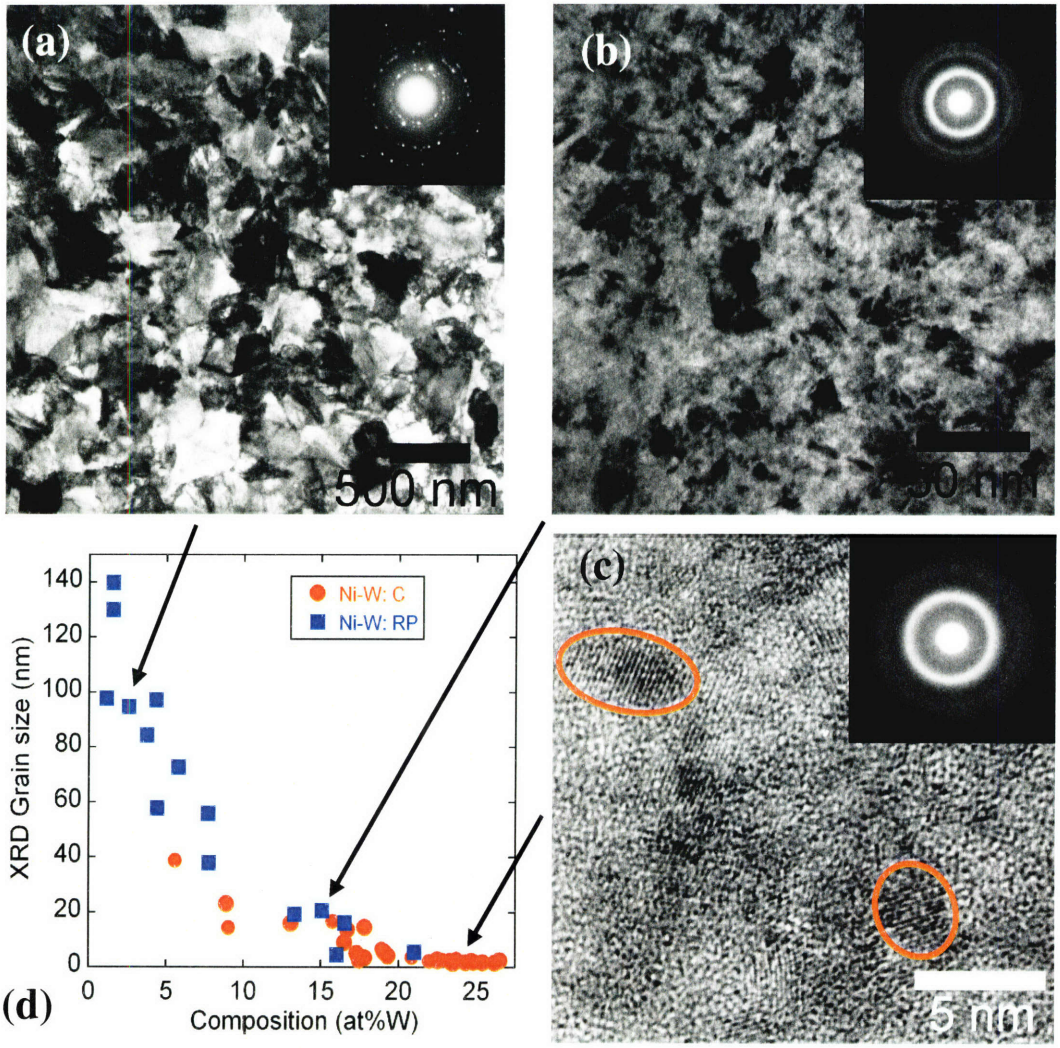

Figure 3.8: (a-c) Bright field TEM images and selected area diffraction patterns showing structural refinement with increasing solute content in Ni-W specimens; two grains are outlined in the high-resolution image (c) where lattice fringes are visible.

3.6 Concluding remarks

The present chapter focused on the experimental synthesis of nanocrystalline Ni-W alloys using electrodeposition. Several parameters of the process where investigated in detail in terms of their effect on alloy composition. We have found that:

- Increasing the electrolyte bath temperature from 45-85 °C leads to increased W content in the deposit over the range of ~9-26 at%.

- Introducing a periodic reverse pulse in the applied current waveform allows for precise control of alloy composition, where increases in either the duration or intensity of the pulse decrease W incorporation in the specimen (cf. Fig. 3.4).

While both bath temperature and reverse pulsing control may be used to adjust the deposit composition, the reverse pulsing technique was shown to yield higher quality specimens free of cracking and other defects. Investigating the microstructure of reverse pulsed specimens revealed a monotonic trend of decreasing grain size with W addition (cf. Fig. 3.7). Combining the relationships in Figs. 3.4 and 3.7 leads to a new, robust method to precisely tailor grain size in nanocrystalline Ni-W alloys. Systematic changes in reverse pulsing conditions affect the deposit composition and, in turn, the grain size of the resulting specimen. It is important to note that the methods developed here should also be applicable to other alloy systems as well; this possibility represents a significant opportunity for future work. In the next chapter we investigate possible mechanisms behind the observed grain size-composition relationship in Ni-W. Specifically, we characterize the grain boundary segregation tendency in experimental specimens to determine the applicability of segregation based models of nanostructure stability.

Chapter 4: Grain boundary segregation in nanocrystalline Ni-W specimens

The experimental results presented in Chapter 3 are characteristic of a system stabilized by grain boundary segregation, after the thermodynamic models of Weissmüller [44] and others [45-47, 50] discussed in the introduction. Specifically, the observed trend of decreasing grain size with alloying addition suggests that W may be segregated at the grain boundaries in nanocrystalline Ni-W. In this chapter we evaluate the potential for nanostructure stabilization through experimental measurements of the grain boundary segregation tendency in Ni-W specimens. Unfortunately, this behavior is difficult to quantify in nanocrystalline materials due to the extremely fine characteristic length-scales, especially when the grain size is below ~20 nm. In this case most traditional methods used to study grain boundary segregation (e.g., energy-dispersive spectroscopy in the TEM, or Auger spectroscopy) are inadequate. Therefore, we use the three-dimensional atom probe (3DAP) in the present work, which provides near atomic-level resolution of the position and chemical identity of individual atoms in a specimen. For a detailed discussion of the atom probe tomography technique, including the history and operation of the instrument, see the works of Miller et al. [182-185].

The 3DAP has been used to study grain boundary segregation in a number of coarse-grained alloys [186]. Typically, the area to be analyzed is pre-screened by TEM and/or field ion microscopy to identify the location and orientation of the grain or phase boundary so that 3DAP data, collected subsequently, can be related back to a known microstructure. A number of authors [97, 187-195] have successfully applied this method to study solute segregation at internal interfaces in steels and Ni-based superalloys. For nanocrystalline materials of the finest grain sizes (less than 20 nm) this type of analysis becomes complicated, as a typical analyzed volume will contain a number of randomly oriented boundaries that are difficult to map, even by TEM. In this case, it is not generally possible to relate 3DAP data directly to a known microstructure, so careful analysis is required when attempting to quantify solute segregation. Because of this and other complications (i.e., specimen preparation, quality, strength, etc.) there have been relatively few atom probe studies of nanocrystalline materials [57, 82, 84, 85, 196-

199]. Of particular relevance to the present work are studies of solute distribution in systems suspected to obey thermodynamic models of nanostructure stabilization, such as Ni-P [46].

The Ni-P system is an example of a strongly segregating alloy and has been studied both experimentally and theoretically by a number of authors including Kirchheim [45], Liu et al. [46], Färber et al. [57], Hentschel et al. [82] and Abraham et al. [200]. Segregation isotherms for this alloy predict essentially perfect saturation-type partitioning of P to the grain boundaries, behavior that has been confirmed in 3DAP experiments [82] on a 9 nm grain size alloy, where composition profiles along the analyzed volume showed clear peaks in P composition at intervals consistent with the average grain size. Unlike Ni-P, the Ni-W system is expected to show only weak segregation behavior owing to the high degree of W solubility in the Ni lattice [107]. In spite of this, the nanocrystalline Ni-W system shows a characteristic composition-dependent grain size (cf. Fig. 3.7) as mentioned above. A 3DAP investigation of nanocrystalline Ni-W has only previously been conducted by Choi et al. [84] in an alloy containing 18 at%W with ~3 nm grain size, where evidence for W segregation to grain boundaries was presented. However, this study focused primarily on the thermal stability and evolution of solute distribution with time and temperature in a single 3 nm grain size specimen. A more complete understanding of the segregation behavior in nanocrystalline Ni-W, to determine the applicability of thermodynamic models of nanostructure stabilization, requires an investigation of specimens over a range of grain sizes.

This chapter seeks to experimentally characterize the solute distribution in high-quality nanocrystalline Ni-W specimens, with grain sizes ranging from 3-20 nm, produced using the reverse pulsing technique described in Chapter 3. To overcome the difficulty in associating 3DAP data with known microstructural features, we introduce a statistical approach to extract an average grain interior and grain boundary composition. This technique is guided by the atomistic computer simulation results of Chapter 2, and has been further validated experimentally in heat-treated nanocrystalline Ni-W specimens in Appendix B. We introduce the technique here as applied to the as-deposited condition. The work that follows has been published in Refs. [201] and [102].

4.1 Atom probe procedures

3DAP experiments were conducted at Oak Ridge National Laboratory (Oak Ridge, TN) on an Imago Local Electrode Atom Probe. Three specimens were examined with average grain sizes of $d \approx 3$, 10, and 20 nm and global compositions of ~19, 16, and 12 at%W, respectively. Needle-shaped specimens required for atom probe experiments were prepared by electropolishing using the standard floating layer method [184, 185] resulting in tip radii of ~50 nm. The specimens were held at 60-70 K under ultra-high vacuum in the 3DAP and subject to a voltage pulse of 20% the standing voltage (typically ~5-10 kV) at a rate of 200 kHz. Following field evaporation, the position and chemical identity of individual ions was back calculated using standard equipment and procedures detailed in Refs. [182-185]. A typical sample volume contained about 15 million atoms with overall dimensions of approximately 60 x 60 x 100 nm. The data obtained from the 3DAP was analyzed with Oxford nanoScience Ltd.'s Position Sensitive Atom Probe (PoSAP) software. Additional analysis was also conducted with custom software written by the authors.

To characterize the grain boundary segregation tendency in electrodeposited specimens, we begin with an analysis of the length scale of composition fluctuations, linking this to the structural length scale of the material. Following this, the extent of segregation is assessed through statistical analysis of the composition distribution. Throughout the analysis, direct comparisons with the atomistic computer simulation results of Chapter 2 facilitate interpretation of the experimental data. As mentioned, the statistical techniques presented here are validated in Appendix B on heat-treated nanocrystalline Ni-W alloys, which form the main focus of Chapter 5.

4.2 Length scales

As a first comparison between experiments and simulations, Fig. 4.1 presents graphical representations of a $d = 3$ nm simulated structure containing 18 at%W (a) and an equal representative volume of the d $\approx$ 3 nm atom probe specimen (b), where tungsten atoms are highlighted; the atom probe structure appears more disordered and more sparsely populated than the simulated cell due to the spatial resolution and limited detection efficiency (~60%) of the

3DAP[†]. From these images the W appears to be approximately randomly distributed with no obvious segregation tendency. Accordingly, more quantitative analysis, involving composition profiles, autocorrelation functions, and composition frequency distributions, are required to better appreciate the solute distribution in these specimens; these techniques will be the main focus of what follows.

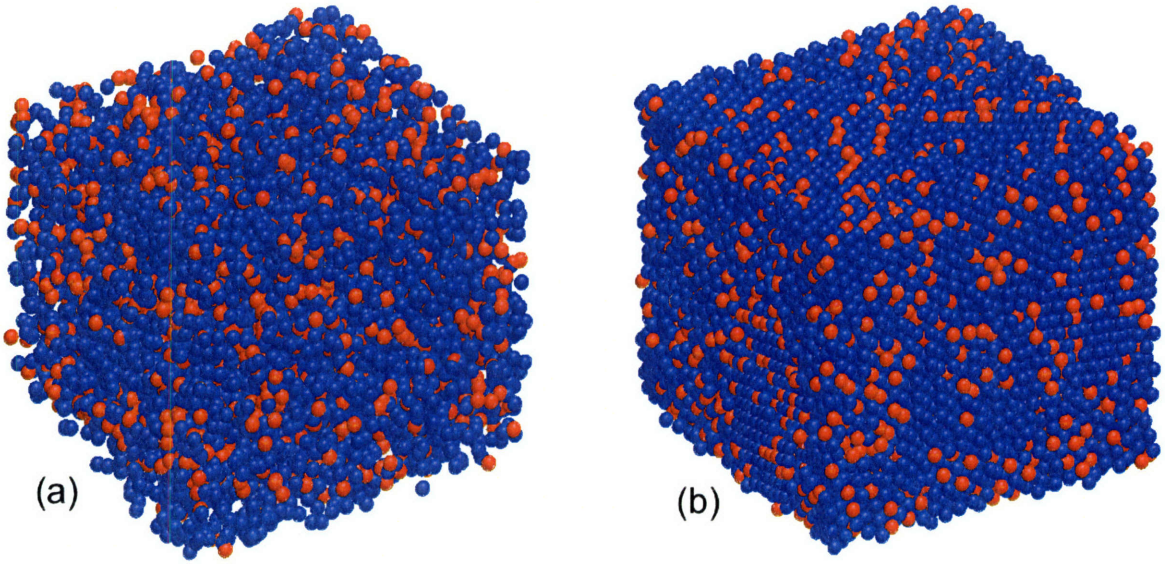

Figure 4.1: Representations of 3 nm grain size (a) experimental and (b) simulated structures with the tungsten atoms plotted in red; specimens are approximately 6 x 7 x 5 nm.

Composition profiles have been constructed along the length of the 3DAP sampling volume (or along a primary axis of the simulated structure) using a 2 nm square cross-section and a moving average over 100 atoms (~0.3 nm resolution); this method has been shown to provide an accurate measure of interfacial composition for specimens containing a single grain boundary of known position [185]. Fig. 4.2 plots typical examples of these profiles for both the experimental (Fig. 4.2(a-c)) and simulated (Fig. 4.2(d)) structures. For each of the 3DAP specimens, the total length of the sampled volume is the distance shown along the x-axis in the composition profiles, while the simulated structure was repeated twice (periodic boundary conditions) to better

[†] In an effort to better match the density and resolution of the atom probe data, we have also considered simulated structures in which 40% of the atoms were removed at random, or in which the atoms were randomly displaced by as much as several atomic diameters. However, these variations were found to have no effect on the analysis presented in this chapter, and here we report only the results from the full, unaltered simulated structure.

elucidate the composition trends. For all of the structures in Fig. 4.2 it is apparent that the composition is not homogeneous, but fluctuates around a mean value with a noticeable periodicity; mean composition is indicated with a thin solid line, and the dashed lines indicate the standard deviation in the data.

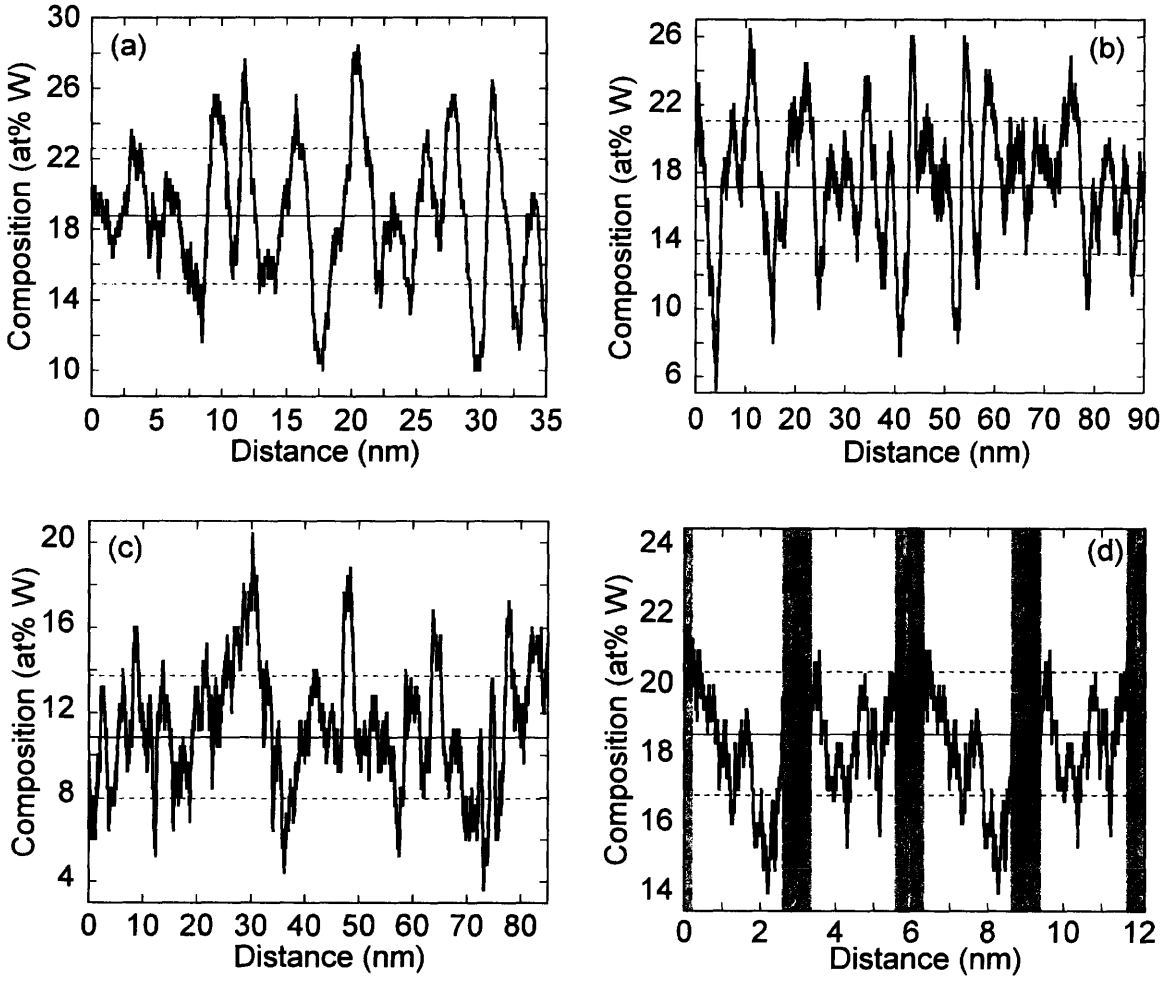

Figure 4.2: Composition profiles for experimental (a) d ≈ 3 nm, (b) 10 nm, (c) 20 nm, and simulated (d) 3 nm structures. The mean composition and standard deviation are marked by thin solid and dashed lines, respectively. In the case of the simulated structure (d) the positions of grain boundaries are known, and are denoted by gray vertical bars.

If grain boundary segregation were present in these specimens then peaks in the composition fluctuations in Fig. 4.2 would be expected to coincide with the location of grain boundaries, and, hence, we expect that the average wavelength of the composition fluctuations should be

consistent with the grain size. Analysis of the simulated structure provides further insight on this issue because, in this case, the positions of the grain boundaries are exactly known. In Fig. 4.2(d) the known grain boundary locations are indicated by thick vertical lines, and it is obvious that the W composition peaks coincide with these positions, confirming the presence of grain boundary segregation. Based on this result, it seems reasonable to infer that the composition peaks in the atom probe data, Fig. 4.2(a-c), also correspond to intergranular regions. Taking those peaks which clearly extend above the standard deviation limit, we calculate mean peak separations of 4, 8, and 17 (± 2) nm, which correspond well with the measured grain sizes of d ≈ 3, 10, and 20 nm, respectively.

A more statistically robust measure of the mean wavelength of composition fluctuations in Fig. 4.2 can be obtained through use of the autocorrelation function. The autocorrelation function has been used in a number of atom probe studies to measure characteristic length scales in a microstructure [185, 202-205], such as the size of precipitates or the periodicity of a composition fluctuation. For a system of assumed spherical symmetry, the autocorrelation function, R_k, can be defined as [185, 206]:

$$R_k = \frac{\sum_{r=0}^{r_{max}-k}(X_r - X)(X_{r+k} - X)}{\sum_{r=0}^{r_{max}-k}(X_r - X)^2} \tag{4.1}$$

where X_r and X_{r+k} are the mean compositions within spherical shells at a distance r and $r+k$, respectively, from a chosen center point, and r_{max} is the largest value of r permitted by the finite sample size. Here k is the characteristic length-scale or "lag" of the measurement, and X is the mean composition of the total analyzed volume. According to Eq. (4.1), a positive value of R_k indicates a correlation in the composition profile, at a wavelength of k, where the values of X_r and X_{r+k} are both greater than the mean composition, X.

Plots of the autocorrelation function, averaged over 100 randomly chosen center points with a k resolution of 0.3 nm, are shown in Fig. 4.3(a-d) for the atom probe and simulation data. The characteristic wavelength is indicated by the value of k coinciding with the first non-trivial maximum in R_k, as marked with arrows.

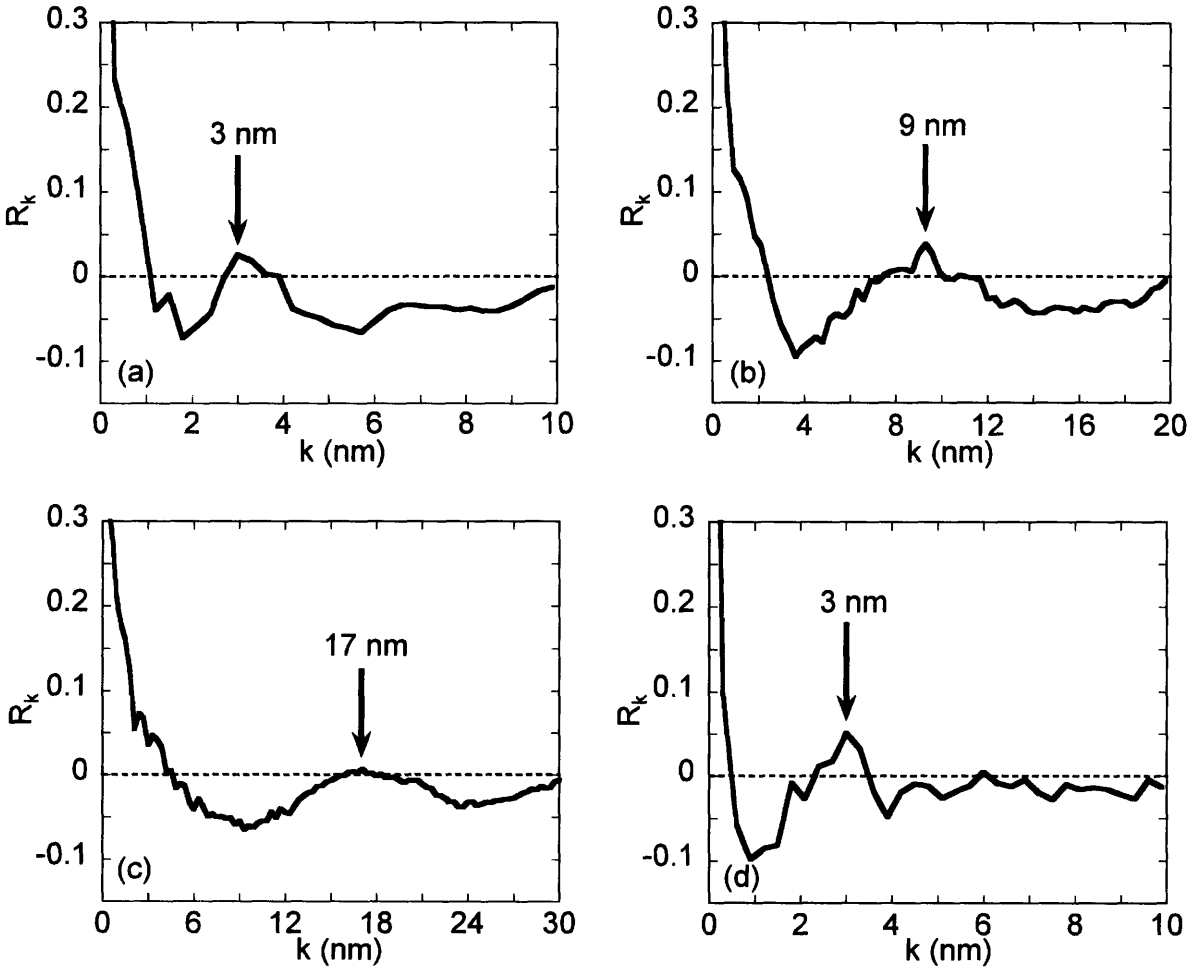

Figure 4.3: Three-dimensional autocorrelation functions for experimental (a) d $\approx$ 3 nm, (b) 10 nm, (c) 20 nm, and simulated (d) 3 nm structures. The first maxima, indicating the periodicity of composition fluctuations, are marked with arrows.

As expected from our earlier discussion, the characteristic length-scales, as determined from the autocorrelation function (d =3, 9, and 17 nm), are in excellent agreement with the measured grain size of the experimental structures ($d \approx$3, 10, and 20 nm, respectively). In addition, the length-scale determined for the simulation data (d =3 nm) lines up well with our *a priori*

knowledge of the solute distribution and grain size of this structure, again confirming segregation to the grain boundary regions.

A summary of our length-scale measurements using TEM and XRD (as described in Chapter 3), as well as observation of the composition profiles and autocorrelation data, are presented in Table 4.1. The mutual agreement between all of these techniques, along with the side-by-side comparison of the experimental data and simulated structure, lends strong support to the assertion that grain boundary segregation is present in these alloys. In the next section, we will be concerned with the amplitude of composition fluctuations in these materials to assess the extent of segregation.

Table 4.1: Comparison of characteristic length-scales as determined by a number of different methods. For the XRD and TEM measurements the values denote the mean grain size, while the composition profiles and autocorrelation function analysis from 3DAP and simulation data give the scale of W composition fluctuations without direct information about grain size.

	Characteristic length-scale (nm)			
	XRD	TEM	Composition profiles	Autocorrelation function
Experimental	2	~3	4	3
	9	~10	8	9
	17	~20	17	17
Simulated	3		3	3

4.3 Extent of segregation

The composition profiles in Fig. 4.2 not only provide information about the length scale of composition fluctuations, but also about the degree to which solute is partitioned in the grain interior and grain boundary. In the case of our idealized simulated structure (Fig. 4.2(d)), the composition peaks are uniquely attributed to grain boundaries, and the solute enrichment is readily discerned as ~7 at% compared with the grain interior regions. In the case of the 3DAP data from experimental materials there is a much wider variability in the composition profiles, due to the larger volume and unknown microstructural elements being sampled (including a range of grain sizes, various grain boundary inclinations with respect to the sampling axis, and

possibly triple junctions). Nevertheless, from the data in Fig. 4.2(a-c) we judge the average level of solute enrichment at the intergranular regions to be on the order of 5-10 at%. As this is an important quantity in thermodynamic models of nanostructure stabilization, a more accurate analysis of the level of intergranular segregation, using composition frequency distributions, is described next.

For a perfectly random binary solid solution the frequency distribution of the composition is binomial, i.e., the probability of a solute atom occupying any atomic site is exactly the atomic fraction of the alloying element. In this case the probability, $P(c)$, of observing any given composition, c, in a sufficiently large discrete sample volume, can be accurately approximated with a single normal distribution given by [207]:

$$P(c) = \frac{1}{\sigma\sqrt{2\pi}} \exp\left[\frac{-(c-X)^2}{2\sigma^2}\right] \tag{4.2}$$

where σ is the standard deviation, calculated as $\sigma^2 = X(1-X)/n$ where n is the number of atoms in the sampling volume. A compelling fit of Eq. (4.2) to experimental data would therefore suggest that the solute distribution were homogeneously random, while deviation of the experimental data from the form of Eq. (4.2) would be characteristic of some non-random solute distribution.

To calculate composition distributions from the 3DAP data, the specimen volumes have been divided into non-overlapping cubes containing $n \approx 100$ atoms each, and the frequency of composition observations amongst these blocks has been counted; the results are presented as solid points in Fig. 4.4(a-c). Also included are the binomial distributions predicted by Eq. (4.2) for a random solid solution (wide black dashed line labeled as "single binomial"); note the poor fit for these specimens, where the observed distribution is significantly broader. This lack of fit suggests some degree of solute partitioning or segregation in the alloy structure, which we will rationalize by modeling nanocrystalline materials as composed of two regions: grain interior and grain boundary. The relative volume fraction of these regions are determined by the grain size, d, through the simple geometric model introduced in Eq. 1.1 [20]. By assuming that the grain

interior (g) and boundary (gb) regions are both random solid solutions, the composition frequency distribution of the microstructure can be characterized by the weighted average of two normal approximations to the binomial distribution:

$$P(c) = \frac{f_g}{\sigma_g\sqrt{2\pi}}\exp\left[\frac{-(c-X_g)^2}{2\sigma_g^{\,2}}\right] + \frac{f_{gb}}{\sigma_{gb}\sqrt{2\pi}}\exp\left[\frac{-(c-X_{gb})^2}{2\sigma_{gb}^{\,2}}\right] \tag{4.3}$$

where each regions is now allowed to have a unique mean composition related to the global mean composition through a rule-of-mixtures ($X = f_g X_g + f_{gb} X_{gb}$), with a standard deviation as defined for Eq. (4.2). For the present analysis, t is approximated as 0.75 nm, in line with previous experimental measures of the grain boundary thickness in similar electrodeposited Ni-W specimens [208] and consistent with the typical width of a segregated grain boundary layer [107] [‡]. Knowing the global mean composition and average grain size, Eq. (4.3) can be fitted to the experimental data with only a single adjustable parameter, either X_g or X_{gb}. From this analysis we can extract the important parameters that characterize the mean composition of the grain interior and grain boundary regions. This analysis is similar to the method of Langer, Baron, and Miller (LBM) [185] used, for example, by Hyde et al. [204] to analyze 3DAP data from a spinodally decomposed Fe-Cr alloy. Here, however, the volume fractions are fixed by Eq. (1.1) and each constituent assumes the corresponding binomial standard deviation. The free parameter, X_g, in Eq. (4.3) has been determined using a least-squares fit over the experimental composition distribution for each of the 3DAP specimens. The results are assembled in Table 4.2, and Eq. (4.3) has been plotted using these best-fit values as a thin blue dashed line (labeled "Binomial-Binomial") in Fig. 4.4(a-c). For the smallest grain size specimen of Fig. 4.4(a) the binomial-binomial approximation fits the experimental data well, while only a moderate improvement is observed for the larger grain size structures of (b) and (c).

To obtain a better fit to the data, we may further relax the constraint on the standard deviations in Eq. (4.3), as there is no reason to assume that the solute distribution is perfectly random in both

[‡] Changing t over the range 0.5-1.0 nm has no major effect on the conclusions drawn.

constituents, as evidenced, for example, by the ordering tendency in the atomistic computer simulations of Chapter 2. Repeating the fitting procedure as above, but now including the additional parameters of σ_g and σ_{gb} (three fitting parameters total), provides an excellent fit to the experiments as shown by the solid red curve in Fig. 4.4(a-c) (labeled "Normal-Normal"); the parameters extracted from this fit are collected in Table 4.2. It is important to note that the

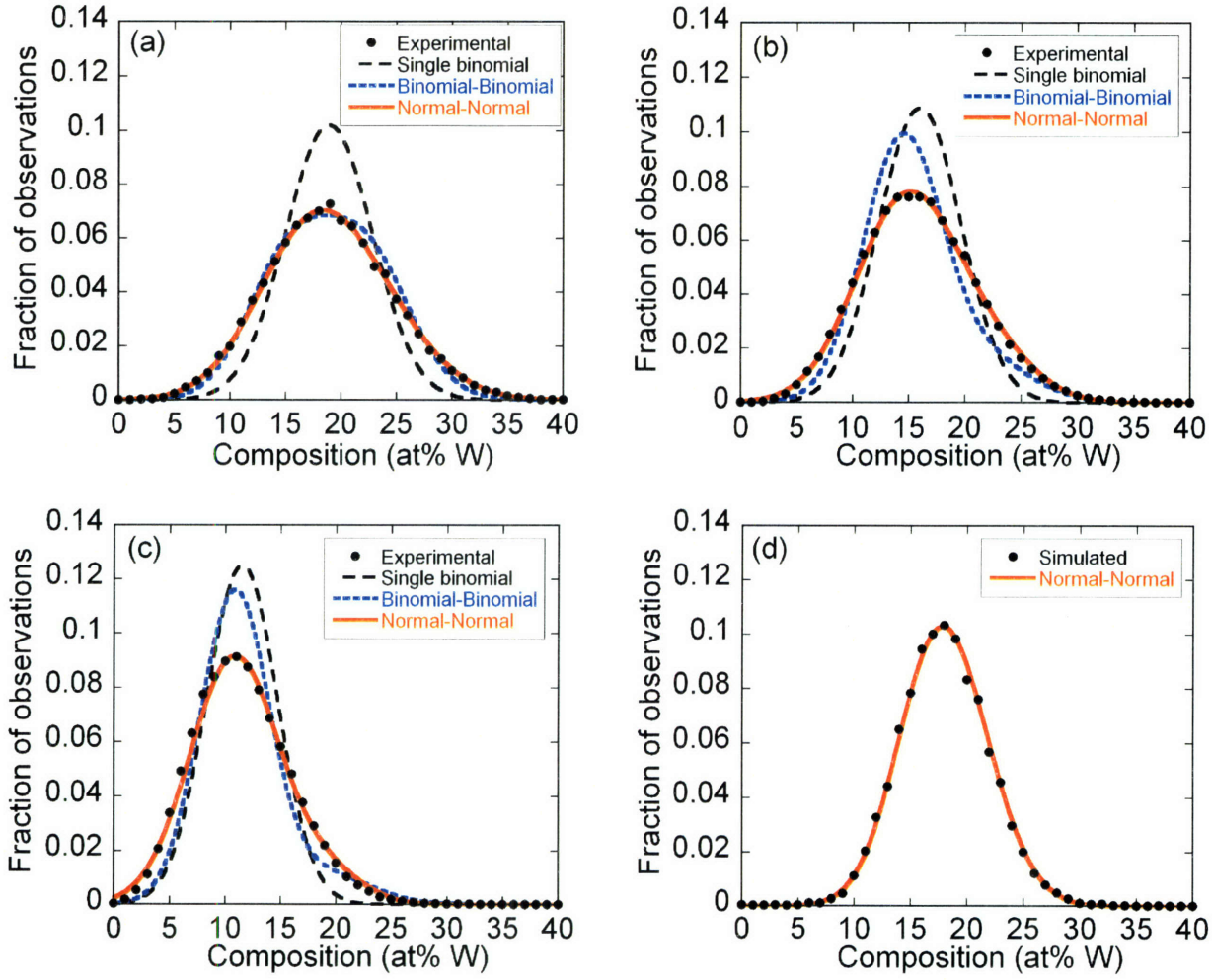

Figure 4.4: Frequency distributions of tungsten composition for experimental (a) d ≈ 3 nm, (b) 10 nm, and (c) 20 nm specimens, compared with the expected single binomial distribution for a random solid solution (Eq. (4.2)). Also shown are fits of the two-constituent distribution of Eq. 4.3 where both the grain boundary and grain interior are modeled as random solid solutions (binomial-binomial) and where the standard deviation of both regions is included as an additional adjustable parameter (normal-normal). In (d), the distribution for the simulated d = 3 nm structure is presented, along with the normal-normal fit.

Table 4.2: Model parameters for the best fit of Eq. 4.3 to the composition frequency distributions in Fig. 4.4 Here, the volume fractions are fixed by Eq. (1.1) and the composition of the grain interior (X_g) and grain boundary (X_{gb}) are related to the mean composition through a rule-of-mixtures. For the binomial-binomial fit, the standard deviations σ_g and σ_{gb} are fixed to approximate the binomial form, while for the normal-normal fit both are included as additional adjustable parameters.

		Binomial-Binomial fit		Normal-Normal fit			
	Grain size (nm)	X_g	X_{gb}	X_g	X_{gb}	σ_g	σ_{gb}
Experimental	3	14.9	21.9	16.4	20.8	4.7	5.6
	10	14.4	21.8	14.8	22.3	4.5	4
	20	10.8	19.2	10.8	19.2	4	3.3
Simulated	3	-	-	16.5	19.2	3.4	3.8

addition of these fitting parameters does not materially affect the main result of this exercise: the compositions extracted for both the binomial-binomial and normal-normal fit are similar for the $d \approx 3$ nm specimen (within 1.5 at%) and nearly identical or exactly identical for the $d \approx 10$ and 20 nm structures, respectively. Consequently, either model will suffice for the purpose of approximating the extent of segregation to the grain boundary regions.

The compositions extracted from these analyses (Table 4.2) directly indicate the average level of solute enrichment at the grain boundaries, which we find to be in line with our earlier observations from the composition profiles of Fig. 4.2. We note that the values of X_g and X_{gb} represent the *mean* compositions of the grain interior and grain boundary regions, and so are not expected to coincide with the composition peaks in Fig. 4.2, but rather with some less extreme value found from averaging over the peaks of different heights and widths. An important result here is that the degree of segregation measured in nanocrystalline Ni-W is relatively subtle (~5-8 at%) as compared to other, strongly segregating alloys such as Ni-P [57, 82].

We can gain further insight on the segregation behavior in this system by considering the simulation data, for which a composition distribution is shown in Fig. 4.4(d). Unfortunately, for the simulated structure we cannot follow precisely the same analysis as used for the 3DAP data because the relatively small number of simulated atoms (~21,000) produces insufficient

sampling statistics to compare with the binomial form of Eq. (4.2). More specifically, the standard deviation of a randomly distributed 21,000 atom structure is narrower than that predicted by the binomial approximation. This precludes application of the binomial-binomial fit, but imposes no limitation on the normal-normal fit with the standard deviations included as free parameters. The results of a normal-normal fit on the simulated distribution are shown in Fig. 4.4(d) with the parameters included in Table 4.2. These values, as for the experimental data, are found to be reasonably in line with the composition profile of the simulated structure.

4.4 Thermodynamically stable nanostructures?

A main goal of the above sections was to verify the existence of grain boundary segregation and quantify its extent in experimental nanocrystalline Ni-W specimens. As pointed out in the introduction, grain boundary segregation and its impact on grain boundary energy form the basis for thermodynamic models of nanostructure stabilization [44-46, 50]. With the results presented in this chapter, along with the atomistic simulation results of Chapter 2, we now compare with existing data in the literature to gauge the potential for thermodynamic nanostructure stability in Ni-W.

Returning to the computer simulations, the grain boundary energy values of Fig. 2.8(b) directly challenge a thermodynamic interpretation of stability in nanocrystalline Ni-W alloys where a state of $\gamma > 0$ is apparently maintained for any alloying addition. An important question then arises as to how systems previously modeled, such as Y-Fe [56] and Ni-P [46], can attain a thermodynamically stable state with vanishing grain boundary energy. Because γ is directly related to grain boundary segregation [135], with more extensive segregation leading to greater reductions in γ, it is instructive to compare the extent of segregation in Ni-W with that assumed in the previously studied systems. Here, we directly compare with Ni-P, for which there have been significant theoretical modeling efforts [45, 46] as well as detailed experimental investigations of solute distribution [57, 82]. The expected large extent of grain boundary segregation in this system is reflected by the high, constant value assumed as the segregation energy (55 kJ/mol [46]) in the proposed theoretical models of nanostructure stabilization. With the composition-dependent H_{seg} derived in the present work for Ni-W (Fig. 2.7), we can

compare the segregation tendency of these two systems using an appropriate isotherm (such as Eq. (2.2) or (2.3)).

The grain size-independent McLean isotherm (i.e., Eq. (2.2) or Eq. (2.3) assuming $d \to \infty$) is plotted as a blue dashed line in Fig. 4.5 for a constant value of $H_{seg} = 55$ kJ/mol, corresponding to that assumed for the Ni-P system. Note that this extremely high segregation energy predicts complete saturation of the grain boundaries in coarse-grained structures over the entire range of

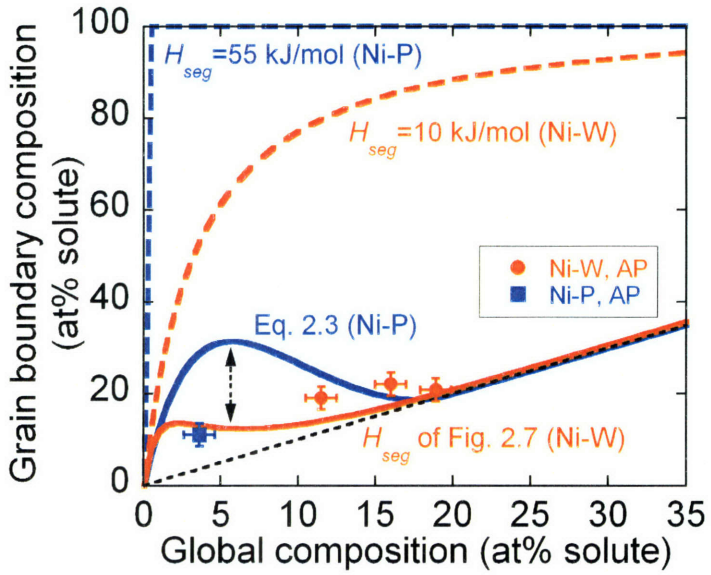

Figure 4.5: Grain size-independent McLean segregation isotherms plotted as blue and red dashed lines for constant segregation energies of H_{seg} = 55 and 10 kJ/mol, respectively, corresponding to the value assumed in a thermodynamic model of nanostructures stability for Ni-P [46], and the dilute limit value determined from the present work in Ni-W (Fig. 2.7). Incorporating nanocrystalline grain-size effects (Eq. 2.3) leads to the solid blue curve for Ni-P alloys, while the exponentially decreasing form of H_{seg} (Fig. 2.7) predicts the solid red curve for Ni-W; these isotherms represent an approximation of the grain boundary segregation tendency in nanocrystalline Ni-P and Ni-W. The disparity between these two predictions (indicated by an arrow) suggests that Ni-W may not derive sufficient grain boundary energy reduction for complete thermodynamic stability. Also shown for comparison are experimental atom probe (AP) data for grain boundary composition in nanocrystalline Ni-W (Table 4.2) and Ni-P [82] specimens.

global composition. To more accurately represent the segregation in nanocrystalline alloys, grain size effects as discussed in relation to Eq. (2.3) must be included in this type of analysis.

Following the results of Liu and Kirchheim [46], the grain size-dependent form assumed for Ni-P is plotted as a solid blue line in Fig. 4.5 for comparison, demonstrating a significant decrease in the predicted extent of segregation for nanocrystalline structures. This grain size-dependent isotherm corresponds to the level of segregation predicted and required for thermodynamically stable Ni-P alloys in Ref. [46].

We may conduct a similar type of analysis for Ni-W, to compare with the Ni-P results. The dashed red line in Fig. 4.5 plots a grain size-independent isotherm assuming a constant value of $H_{seg} = 10$ kJ/mol, corresponding to the dilute limit value found for Ni-W (Fig. 2.7), and representing an upper bound for the extent of segregation. Note that this curve falls well below the grain size-independent form assumed for Ni-P. For a more accurate representation of the segregation behavior in Ni-W we may incorporate grain-size effects (as in the Ni-P analysis), as well as the composition-dependent form of H_{seg} derived in Fig. 2.7. In our analysis we have found that the latter effect most significantly affects the shape of the curve in Fig. 4.5, with the additional effect from nanocrystalline grain sizes being relatively minor by comparison. The solid red line in Fig. 4.5 plots Eq. (2.2) incorporating the composition-dependent segregation energy from Fig. 2.7, and presents a reasonable estimate of the extent of segregation in nanocrystalline Ni-W structures.

At this point we can compare the nanocrystalline Ni-P and Ni-W systems on an equal basis, as the solid blue and red curves in Fig. 4.5 most accurately reflect the respective solute distribution in the thermodynamic model of Kirchheim et al. for Ni-P [45, 46], and also that expected in Ni-W based on our simulations. Also shown for comparison are experimental atom probe data in both these systems; the Ni-W data (from Table 4.2) line up reasonably well with the simulation prediction, while the Ni-P isotherm appears to overestimate grain boundary composition for the single experimental point measured [82]. We note that these data are somewhat complicated as the analytical and computer simulation predictions are based on equilibrium calculations, while the experimental electrodeposited specimens are not necessarily in an equilibrium state. Nevertheless, the most important finding here is that in the range of ~2-17 at% solute the isotherm for Ni-P anticipates significantly higher grain boundary solute content as compared to Ni-W (as indicated by the arrow in Fig. 4.5). It is this high assumed extent of segregation that

could lead to a condition of $\gamma = 0$ in Ni-P, for which there would be true thermodynamic stability as proposed by Kirchheim et al. [45, 46]. On the other hand, the comparatively subtle degree of segregation in Ni-W suggests that the grain boundary energy may not be depressed as thoroughly in this system; this is consistent with the results presented in Fig. 2.8(b), which indicates that the grain boundary energy is positive for the conditions we have simulated.

Although true thermodynamic stability may not be reached in nanocrystalline Ni-W, a non-vanishing grain boundary energy does not rule out the possibility of achieving metastable nanocrystalline structures as proposed by Krill et al. [50]. Based on experiments in the Pd-Zr system, Krill et al. found that a significant reduction in γ still leads to the characteristic grain size-composition relationship in this system, in line with theories of segregation-based nanostructure stabilization but relying on a kinetic, rather than purely thermodynamic explanation. In this case, the condition of metastability is a significant reduction in γ such that the driving force for grain growth is diminished [55]. Linking the thermodynamic and kinetic approaches, data such as those in Fig. 2.8(b) may be useful in defining a threshold value for γ below which grain growth is effectively suppressed. Instead of requiring $\gamma = 0$, for example, we may relax this constraint and instead require that $\gamma \leq C \cdot \gamma_o$, where C takes on a value from 0-1 and γ_o is the grain boundary energy of the pure solvent.

To gain some insight into the extent of γ reduction in experimental Ni-W alloys, we can compare the data of Fig. 2.8(b) with the experimental grain size-composition relationship presented in Chapter 3 (cf. Fig. 3.7). Although these data were acquired from electrodeposited specimens, and thus, as mentioned above, are not necessarily in an equilibrium state, we can estimate the extent to which their grain boundary energy may be reduced. Figure 3.7 suggests that alloys with grain sizes in the range of 2-4 nm prefer an experimental composition of ~22 at%W. At this composition, Fig. 2.8(b) yields a grain boundary energy of ~0.35 J/m^2, a ~60% reduction from the pure Ni value of 0.87 J/m^2 (i.e. $C = 0.4$ in the above discussion). This reduction in grain boundary energy is significant, and should substantially stabilize the nanocrystalline structure. However, this result also supports the notion that these

electrodeposited alloys are out of equilibrium, since true thermodynamic stability ($\gamma = 0$) has apparently not been achieved.

4.5 Concluding remarks

The solute distribution in nanocrystalline Ni-W alloys has been investigated in the present chapter by means of atom probe tomography. Three experimental specimens with grain sizes of ~3, 10, and 20 nm were examined, and their solute distribution compared with a simulated 3 nm grain size structure. The following major conclusions were drawn:

- The characteristic length-scale of composition profile fluctuations, and that extracted from a three-dimensional autocorrelation function analysis, are consistent with the grain size of experimental and simulated structures, indicating segregation of W to the grain boundaries.
- For the experimental and simulated specimens, the observed composition frequency distribution is best described by a two-constituent model, with unique mean compositions in grain interior and intercrystalline regions.
- The compositions extracted for the grain interior and boundary regions reveal a comparatively subtle degree of grain boundary segregation in Ni-W, as compared to other nanocrystalline alloys that apparently obey thermodynamic models of nanostructure stability.

The use of a simulated structure with known grain boundary locations has significantly aided the present analysis by allowing direct comparison of the simulated structure with experimental specimens. Furthermore, the statistical techniques presented in this chapter have been validated in Appendix B on heat treated specimens, suggesting the accuracy and robustness of these methods for measuring grain boundary segregation in nanocrystalline alloys.

The consequences of a subtle degree of segregation in Ni-W have been discussed in terms of the possible reduction in grain boundary energy and likelihood for thermodynamic nanostructure stability in these alloys. Comparing with computer simulations, a ~60% reduction in grain boundary energy is estimated for grain sizes in the range of 2-4 nm, suggesting that

nanocrystalline Ni-W structures are not thermodynamically stable. The elevated temperature behavior of Ni-W specimens will be investigated in detail in the next chapter.

Chapter 5: Thermal stability of nanocrystalline Ni-W alloys

The results of the previous three chapters suggest that nanocrystalline Ni-W alloys may benefit from a significant reduction in grain boundary energy and, hence, should show improved elevated temperature stability compared to pure systems. In the present chapter, we examine the thermal stability of Ni-W alloys by combining traditional and advanced techniques to track grain size, chemical ordering, and grain boundary segregation during isothermal annealing. We also discuss evidence for grain boundary relaxation, including preliminary property measurements, showing that this mechanism is particularly important for the finest nanocrystalline structures. We conclude with an overview of the various processes activated during annealing by way of a microstructural evolution map, incorporating analytical descriptions of the relevant mechanisms in both pure and alloyed systems. The work contained in this chapter is included in Ref. [209].

5.1 Experimental procedures

Nanocrystalline Ni-W specimens were electrodeposited using the periodic reverse pulsing technique described in detail in Chapter 3. For the present investigation, we have used a forward (cathodic) current density of 0.2 A/cm^2 either in direct current mode, or pulsed with a 20 ms forward duration and a 3 ms reverse of 0.1 or 0.2 A/cm^2 intensity. These three conditions resulted in specimens with grain sizes (compositions) of approximately 3 nm (21 at%W), 20 nm (13 at%W), and 70 nm (6 at%W), respectively. All specimens were deposited on commercial purity Ni substrates and will be referred to by their as-deposited (starting) grain size, d_o, throughout this chapter.

Following the electrodeposition process, specimens were isothermally annealed in an inert argon atmosphere at temperatures ranging from 150 to 900 °C and times from 0.5 to 72 hours, followed by a water quench. Structural characterization was performed by X-ray diffraction (XRD) and transmission electron microscopy (TEM) using the procedures outline in Section 3.2. Atom probe tomography, as introduced in the previous chapter for as-deposited specimens, was used to characterization the solute distribution in two representative heat treated specimens ($d_o = 3$ nm heated at 600 °C for 3 hr, and $d_o = 20$ nm heated at 600 °C for 0.5 hr); details of these

experiments can be found in Appendix B. Calorimetry experiments were conducted in a TA Instruments Q1000 differential scanning calorimeter (DSC) at a heating rate of 20 °C/min. Preliminary property measurements were obtained through microhardness indention on a Clark model DMH2 indenter using a 100 g load applied for 15 seconds.

In what follows we begin with an analysis of the structural evolution with heat treatment in nanocrystalline Ni-W alloys using XRD and TEM techniques, with the main goal of assessing grain growth during annealing. We then focus on detailed characterization of the solute distribution, and also present evidence for grain boundary relaxation in the annealed specimens. Data from all isothermal experiments are included as Appendix C, and here we present the main results.

5.2 Grain growth

In the as-deposited state, all three of the present Ni-W alloys are fcc solid solutions, as revealed by both XRD and TEM observations (see Chapter 3). Using XRD line profile analysis, we can accurately quantify the average grain size of Ni-W alloys, in addition to characterizing any secondary phases that may precipitate during annealing. A series of XRD patterns are presented in Fig. 5.1 for the $d_0 = 3$ nm Ni-W specimen heated for 24 hrs at various temperatures from 300 to 900 °C. Note that the structure appears nearly unchanged up to 450 °C, indicating the excellent thermal stability of this alloy as compared to, for example, pure nanocrystalline Ni [58, 60, 61, 210] which coarsens to the micron scale under similar conditions. At 600 °C the XRD pattern sharpens and higher-order fcc-Ni peaks become more obvious, consistent with coarsening of the grain structure. At the highest annealing temperature of 900 °C peaks associated with the equilibrium Ni_4W phase emerge, as expected given the high W content (21 at%) of this alloy [96]. Similar coarsening trends (i.e. sharpening of the fcc diffraction peaks) are observed during annealing of the $d_0 = 20$ and 70 nm specimens, with the notable difference that the Ni_4W phase never appears in these lower W content alloys for the set of conditions studied here. Quantitative grain size measurements based on the XRD analyses are compiled in Fig. 5.2 as a function of temperature for all specimens following 24 hr heat treatments. This plot demonstrates the

exceptional thermal stability of nanocrystalline Ni-W below ~500 °C. At higher temperatures grain growth occurs in all cases, but ultrafine or even nanocrystalline structures are still retained.

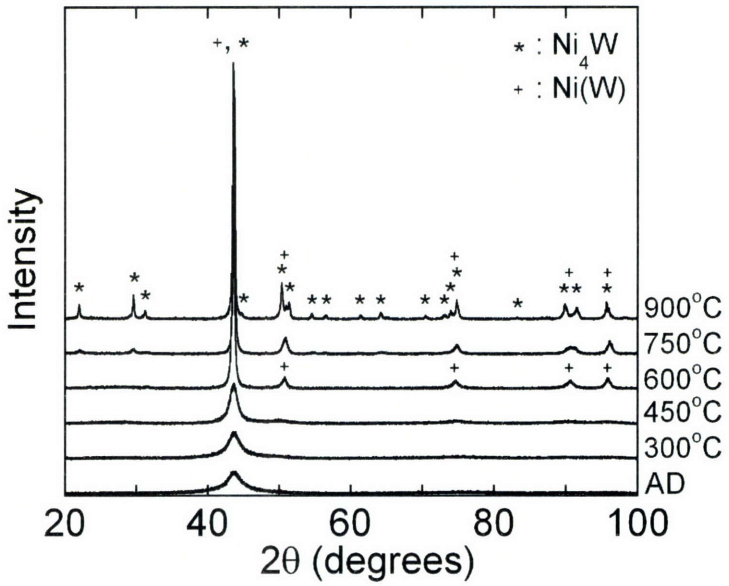

Figure 5.1: X-ray diffraction patterns for 24 hr heat treatments of an as-deposited (AD) 3 nm grain size specimen containing 21 at%W. The structure remains fairly stable up to 450 °C followed by coarsening and eventual precipitation of the equilibrium Ni_4W phase at higher temperatures.

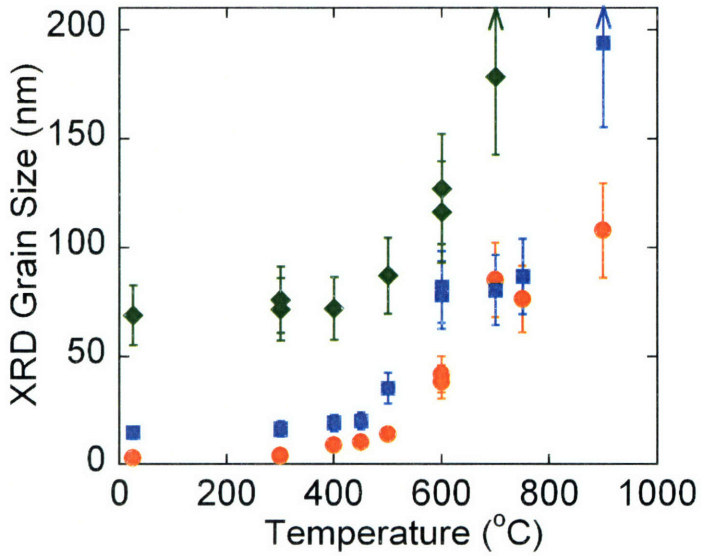

Figure 5.2: Grain size quantified by X-ray diffraction analysis for 24 hr heat treatments of three different starting grain sizes (plotted at 25 °C), showing excellent stability up to ~500 °C.

As an assessment of long-term stability, two XRD patterns are presented in Fig. 5.3 for a $d_o = 3$ nm Ni-W specimen deposited in October, 2003. In Section 1.3 we mentioned that a number of pure nanocrystalline materials have shown significant grain growth at room temperature, even when measured over a period of several days or less [62, 63]. The XRD pattern labeled "April, 2007" in Fig. 5.3 was taken on the same $d_o = 3$ nm specimen after 3.5 years exposure at room temperature; there is no apparent change in the structure and no measurable increase in grain size. This again points to the excellent stability of nanocrystalline Ni-W alloys.

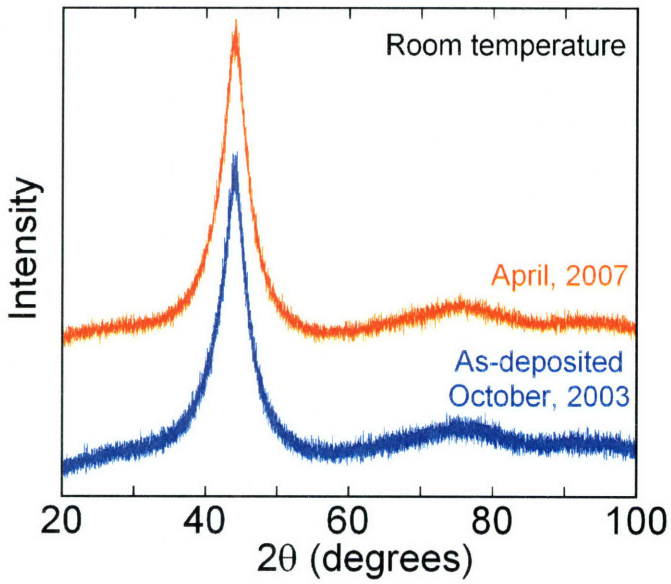

Figure 5.3: X-ray diffraction patterns for a ~3 nm grain size Ni-W specimen deposited in October, 2003. No change in the structure is observed after 3.5 years at room temperature, indicating the exceptional long-term stability of the present alloys.

The above analysis gives a sense of the thermal stability of nanocrystalline Ni-W based on indirect grain size measurements. In order to confirm these measurements, and also observe the type of grain growth (i.e. normal or abnormal), we have conducted direct TEM investigations on several specimens. Representative bright field images and inset SAD patterns are shown in Fig. 5.4 for the (a) $d_o = 3$ nm specimen heat treated for (b) 3 hr at 600 °C and (c) 12 hr at 700 °C as well as the (d) $d_o = 20$ nm specimen heated at 600 °C for (e) 0.5 hr and (f) 12 hr. The grain sizes observed in Fig. 5.4 are in line with those determined by XRD: (a) 3, (b) 16, (c) 100, (d) 20, (e) 28, and (f) 73 nm. The SAD patterns are also consistent with grain coarsening where the diffraction lines sharpen and eventually form discrete spots as fewer grains are sampled. Lastly,

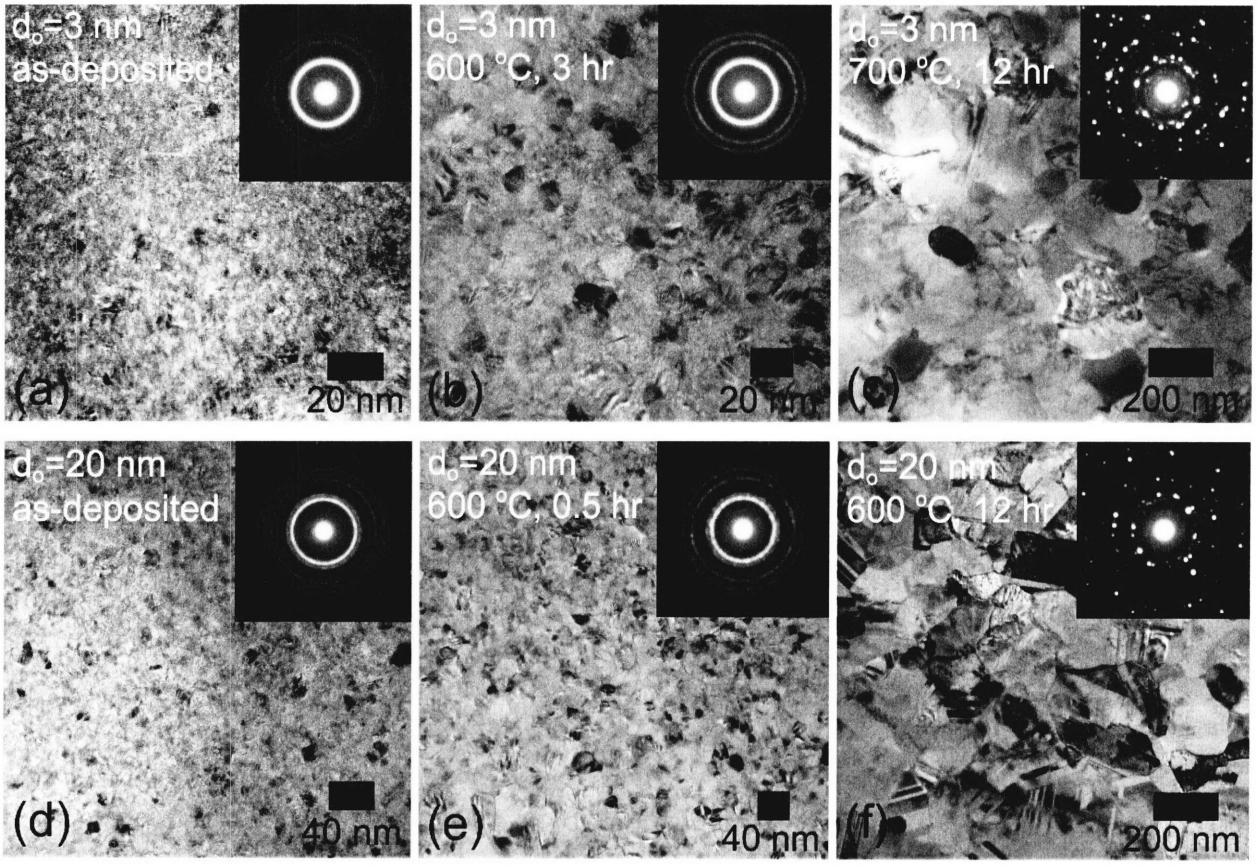

Figure 5.4: Bright-field transmission electron microscopy images and inset selected area diffraction patterns for as-deposited (a-c) ~3 nm and (d-f) ~20 nm grain size specimens in their initial and heat treated states as indicated. Grain growth is normal in all cases.

in no case do we find evidence of abnormal grain growth in Fig. 5.4, such as has been observed in nearly all pure nanocrystalline materials [60, 63, 211]. This uniformity of grain size is an important finding, and simplifies our subsequent analysis by ruling out possible complications from a bimodal grain size distribution.

The above analyses constitute a typical approach to evaluate the thermal stability of nanocrystalline materials; isothermal annealing followed by structural characterization using XRD and TEM techniques. In what follows, we extend our discussion to investigate the solute distribution in nanocrystalline Ni-W. We first consider chemical ordering information that can be gleaned from the electron diffraction patterns in Fig. 5.4, followed by a review of the atom

probe tomography experiments in Appendix B to assess the grain boundary segregation tendency.

5.3 Chemical ordering

The chemical ordering of coarse-grained Ni-W alloys has been extensively studied by Mishra et al. [108, 109, 212] through isothermal annealing experiments at both stoichiometric (Ni_4W) and off-stoichiometric compositions. In addition, the chemically similar Ni-Mo alloy, for which the equilibrium phase diagram is comparable to Ni-W below ~900 °C and at alloying additions less than 25 at% [213], has received even more attention because of its potential application as a high-temperature, corrosion resistant material [111-113, 117, 118, 212, 214-218]. The progression of chemical ordering in both these materials is well established based on electron diffraction experiments in the TEM [108, 109, 111], as well as computer simulation [112, 117, 118]. Following a rapid quench from the melt, supersaturated fcc structures of Ni-W and Ni-Mo can be obtained with no evidence of second-phase (Ni_4W or Ni_4Mo) precipitation. However, the SAD patterns for both these materials show diffuse intensity maxima at {1 ½ 0} positions, which has been attributed to chemical short range ordering (SRO) in the system [108, 109, 111, 113, 118, 216, 217]. Following low temperature annealing, the SRO spots typically increase in intensity and, at higher temperatures (or longer times) split into positions corresponding to the long range ordered (LRO) equilibrium second phase. The SRO condition can therefore be considered as a precursor to the LRO state, and this transition can be monitored through SAD analysis.

Based on the work introduced above, information about the SRO and LRO behavior in the present Ni-W alloys can be accessed by examining SAD patterns, such as those of Fig. 5.4. To precisely evaluate these patterns, radial intensity profiles have been constructed extending outward from the center of the direct beam, as presented in Fig. 5.5 for each of the patterns in Fig. 5.4, with the addition of a low temperature 300 °C, 24 hr heat treatment. Given differences in exposure time, grain size, and sample thickness, the edges of the direct beam and peak intensities vary from one condition to the next. Nevertheless, we may gather important information about the ordering tendency in these alloys from the peak positions and intensity trends at low Bragg angles.

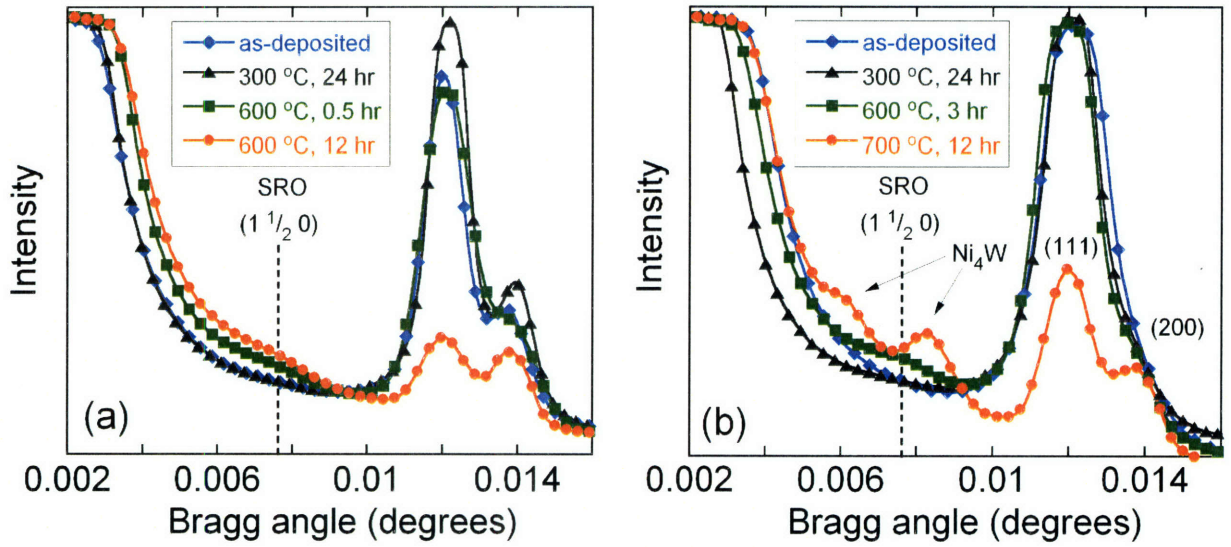

Figure 5.5: Selected area electron diffraction intensity profiles for the (a) $d_o = 20$ nm grain size specimen containing 13 at%W and the (b) $d_o = 3$ nm grain size specimen containing 21 at%W. Short range ordering, as evidenced by intensity maxima at the {1 ½ 0} position, is observed for temperatures greater than 300 °C in both figures. (b) A long range order transition to the equilibrium Ni_4W phase appears in this higher W content alloy at sufficiently high temperature and time.

The as-deposited state (blue diamonds) for both the (a) $d_o = 20$ and (b) $d_o = 3$ nm specimens show a monotonic decrease in measured electron intensity at low Bragg angles below the {111} peak position at ~0.012 degrees. In particular, there is no discernible feature at the {1 ½ 0} position at 0.0076 degrees, which is consistent with a state of complete chemical disorder in the system. This disordered state is apparently maintained following a relatively low temperature heat treatment at 300 °C for 24 hr, after which no appreciable change in the intensity profile is observed near the {1 ½ 0} position for either specimen. Heating the $d_o = 20$ nm specimen at a higher temperature of 600 °C, however, results in a progressive increase in intensity around the {1 ½ 0} position in Fig. 5.5(a), indicative of SRO development. As this alloy lies very near the solubility limit (~13 at%W) at 600 °C [96], it is not surprising that some degree of SRO should develop during annealing. This observation is consistent with that of Mishra et al. [108] who found diffuse intensity maxima at the same {1 ½ 0} positions in a coarse-grained, rapidly quenched Ni-15 at%W alloy. Similarly, the $d_o = 3$ nm specimen shows a broad intensity maximum at {1 ½ 0} after a 3 hr anneal at 600 °C, indicating that SRO also develops in this

alloy. However, due to the higher W content (21 at%) of this specimen, further annealing leads to splitting of the {1 ½ 0} peak into two peaks associated with the equilibrium Ni_4W phase. Because this alloy lies very near the stoichiometric Ni_4W composition, the observed SRO to LRO transition is expected and is again consistent with the work of Mishra et al. on a cast Ni-20 at%W alloy [109].

The measurements in Fig. 5.5 suggest that the ordering sequence in electrodeposited nanocrystalline Ni-W alloys is similar to that observed in rapidly quenched coarse-grained specimens. It is important to note, however, that the as-deposited state in the present work (including both stoichiometric and off-stoichiometric compositions) more closely resembles a random solid solution, with no sign of short or long range chemical ordering. This is unlike the work of Mishra et al. [108, 109, 111] and others [113, 216-218] where rapidly quenched Ni-W or Ni-Mo specimens show diffuse SRO spots prior to annealing. This may be the result of a higher effective "quench rate" for electrodeposition, which has been described as a highly driven process capable of achieving non-equilibrium states [179], or it may be a fundamental consequence of the nanocrystalline grain size. Farkas et al. [128] have proposed that the high density of grain boundaries in nanocrystalline structures may actually lead to a chemical disordering effect, and our simulation work in Chapter 2 has shown the same tendency in Ni-W alloys in particular. Grain growth would then further facilitate ordering during annealing as the density of grain boundaries decreases.

5.4 Grain boundary segregation

Atom probe tomography investigations of the segregation tendency in nanocrystalline Ni-W alloys are reported in Chapter 4 and Appendix B for as-deposited and heat treated specimens, respectively. These analyses yield an average grain interior and boundary composition for each specimen and we use this information here to assess the evolution of grain boundary segregation during annealing. TEM images of the selected heat treated structures are shown in Fig. 5.4(b) and (e) for the 16 and 28 nm grain size specimens, respectively.

To compare the extent of segregation in the as-deposited and heat treated conditions we plot grain boundary composition vs. grain interior composition in Fig. 5.6; grain size is indicated next

to each point and the dashed line in this figure is for the case of no grain boundary segregation where both regions share equal W content. It is apparent that the extent of segregation for the heat treated specimens (i.e. the difference between grain boundary and interior compositions) is similar to that in the as-deposited state; no dramatic enhancement or reduction in grain boundary segregation is apparent as a consequence of annealing. In fact, the minor differences between as-deposited and annealed samples presented in Fig 5.6 are in line with the analytical work of Ishida [131]. As discussed in Chapter 2, Ishida introduced a rule-of-mixtures into the McLean segregation isotherm (Eq. 2.2) to account for the significant fraction of grain boundaries in nanocrystalline materials, and to offer a simple model for changes in segregation state due only to changes in grain size (cf. Eq. 2.3). This concept is best illustrated by comparing the solute distribution in the as-deposited 3 nm specimen with that in the heat treated 16 nm grain size structure, which was annealed from a similar as-deposited $d_o = 3$ nm state. Both samples have approximately the same global composition, near 20 at%W, but their grain boundary volume fractions are now significantly different following heat treatment. Using the geometric construction of Palumbo et al. [20] and assuming a grain boundary thickness of 0.75 nm, we

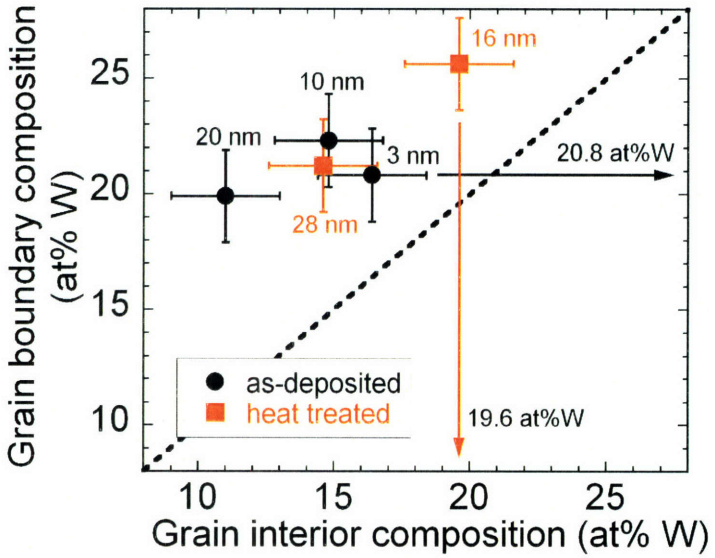

Figure 5.6: Grain boundary vs. grain interior composition for as-deposited and heat treated Ni-W alloys as reported in Chapter 4 and Appendix B, respectively; grain size is indicated next to each point. A similar extent of segregation is observed for all specimens.

calculate that the majority of the 3 nm structure is comprised of grain boundaries (~58%). As a consequence, the grain boundary composition is the dominant contribution to the global composition, as indicated by the horizontal black arrow at 20.8 at%W in Fig. 5.6. On the other hand, the 16 nm specimen contains a larger fraction of grain interior regions (~87%) and, therefore, the grain interior composition essentially equals the global measurement, as shown by a vertical red line at 19.6 at%W in Fig. 5.6. The observed differences in solute distribution between the as-deposited 3 nm and the heat treated 16 nm grain size samples can thus be explained on the basis of grain growth alone. This suggests that the energetics of segregation are essentially similar in both the as-deposited and heat treated conditions.

5.5 Evidence for grain boundary relaxation

The potential for grain boundary relaxation is relevant for all nanocrystalline materials, whether alloyed or pure, and should have an increasingly important effect on properties as grain size is reduced to the finest levels. In what follows, we present evidence for relaxation of the present Ni-W alloys through several techniques including calorimetry, hardness measurements, and atom probe tomography.

A number of studies have focused on calorimetric data and the heat released during annealing of both pure [58-61, 73-75] and alloyed [82, 85, 92] nanocrystalline materials. Exothermic signals have mainly been attributed to two irreversible reactions: grain boundary relaxation and grain growth. During relaxation, energy stored in the form of excess grain boundary dislocations is released as the boundary transforms to a more stable configuration, while exothermic grain growth signals are the direct result of a reduction in total grain boundary area. To confirm that heat released is a consequence of relaxation therefore requires that there be no increase in grain size. For the present Ni-W alloys, we have used DSC to measure irreversible heat flow [59] over a temperature range where grain size remains constant – below 300 °C according to Fig. 5.2. The results are presented in Fig. 5.7 for the $d_o = 3$, 20, and 70 nm specimens. It is important to note that at these relatively low temperatures we also find no evidence of significant chemical ordering (cf. Fig. 5.5) and expect no change in the extent of grain boundary segregation (cf. Fig 5.6). Therefore, the exothermic signals of Fig. 5.7 are likely the result of grain boundary

relaxation alone, allowing for several interesting conclusions to be drawn. First, an exothermic onset temperature of ~120 °C is observed for all specimens, indicating that a structural change occurs even at this relatively low temperature. Second, the total amount of heat released scales inversely with grain size, amounting to ~37, 22, and 6 J/g for the 3, 20, and 70 nm grain size

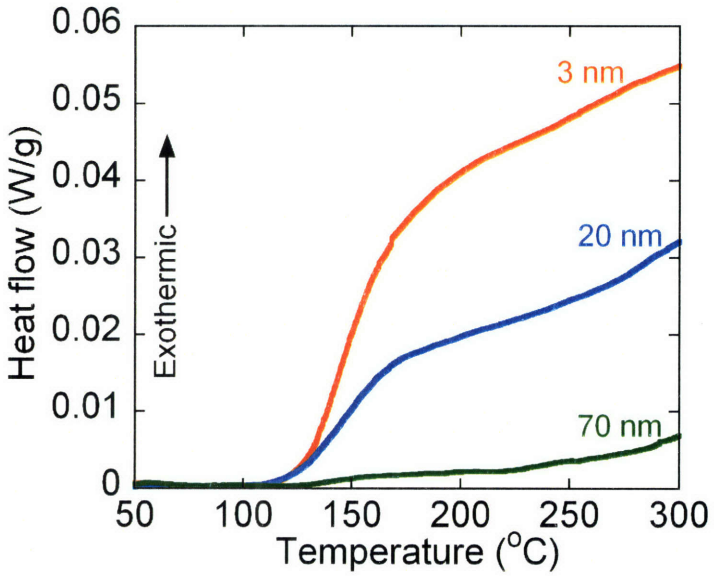

Figure 5.7: Differential scanning calorimetry results showing the irreversible heat release in as-deposited 3, 20, and 70 nm grain size specimens; all experiments were performed at a scanning rate of 20 °C/min. Exothermic signals, beginning at ~120 °C, scale inversely with grain size and are attributed to grain boundary relaxation of the as-deposited Ni-W specimens.

specimens, respectively. Normalizing these energies by an estimated grain boundary area for each sample [20] yields values of ~1 J/m^2 in all cases, on the order of a typical grain boundary energy [21]. Thus, a significant amount of heat is released during low temperature annealing and this amount scales directly with grain boundary area. These observations support an interpretation of grain boundary relaxation in nanocrystalline Ni-W.

Additional evidence for grain boundary relaxation in nanocrystalline Ni-W is presented by macroscopic property measurements. As mentioned in the introduction, the detailed structure of the boundaries plays an important role in nanocrystalline materials, and both experimental [77, 90, 219] and theoretical works [68, 76, 220] have suggested a possible strengthening effect due to relaxation. In light of this, we have used microhardness indentation as a preliminary strength

measurement to assess the effect of relaxation in Ni-W. To isolate the effect of grain boundary relaxation, we consider only low temperature heat treatments (up to 300 °C), where a significant amount of heat can be released from the sample (cf. Fig. 5.7) with no appreciable change in the grain size (cf. Fig. 5.2), chemical ordering (cf. Fig. 5.5), or grain boundary segregation tendency (cf. Fig. 5.6). For samples heat treated at 300 °C for 24 hr, no grain growth was measurable beyond the measurement noise, and for samples heat treated below this temperature grain growth can simply be neglected. Changes in the hardness values of such samples therefore likely reflect changes in the state of the grain boundaries, and Fig. 5.8 shows that finer grain sizes and higher annealing temperatures result in proportionally more strengthening. Similar to our argument for

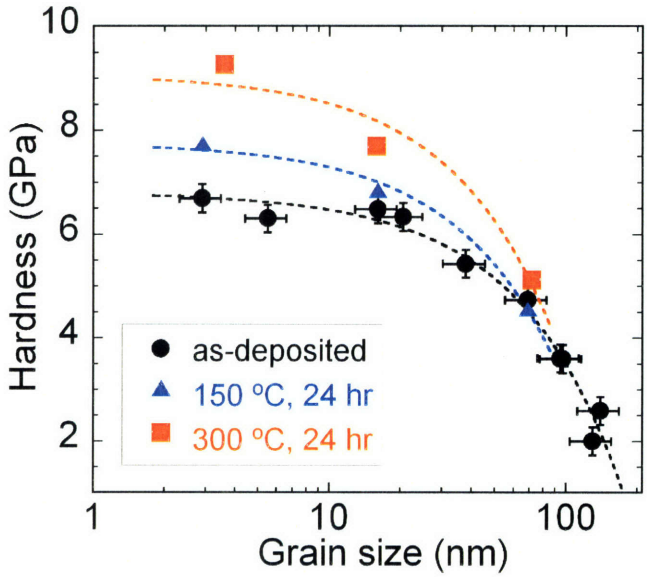

Figure 5.8: Linear-log plot of hardness vs. grain size for specimens in both the as-deposited condition and subject to low temperature heat treatments where negligible grain growth, chemical ordering, and solute redistribution occur. Significant hardening is observed at the finest grain sizes, likely as a result of grain boundary relaxation.

the heat release scaling in Fig. 5.7, this finding is consistent with grain boundary dominated eformation mechanisms that become increasingly important as grain size is reduced. At the finest grain size of ~3 nm, for example, hardness can be increased by almost 3 GPa whereas the largest grain size examined (~70 nm) shows no significant change in hardness within measurement error. The degree of grain boundary relaxation clearly plays an important role in determining the strength of nanocrystalline Ni-W, in particular for the finest grain sizes, and

should be considered when conducting fundamental studies of deformation mechanisms or other properties in nanocrystalline materials in general.

Lastly, some additional qualitative support for a structural change in the grain boundaries is provided by the atom probe data. Based on local structural and energetic effects, a higher number density of grain boundary atoms are often detected in atom probe experiments [182, 197, 221], which, incidentally, serves as an important marker for grain boundary locations in Appendix B. With this in mind, we turn our attention to Fig. 5.9 where the positions of W atoms are plotted within a 4 nm slice of an (a) as-deposited and (b) heat treated specimen having similar grain sizes of ~10 and 16 nm, respectively. In the as-deposited state W atoms appear to be randomly distributed (a) whereas a clear grain structure is observed in the heat-treated specimen (b). It is important to note that this effect is not due to grain boundary segregation, as

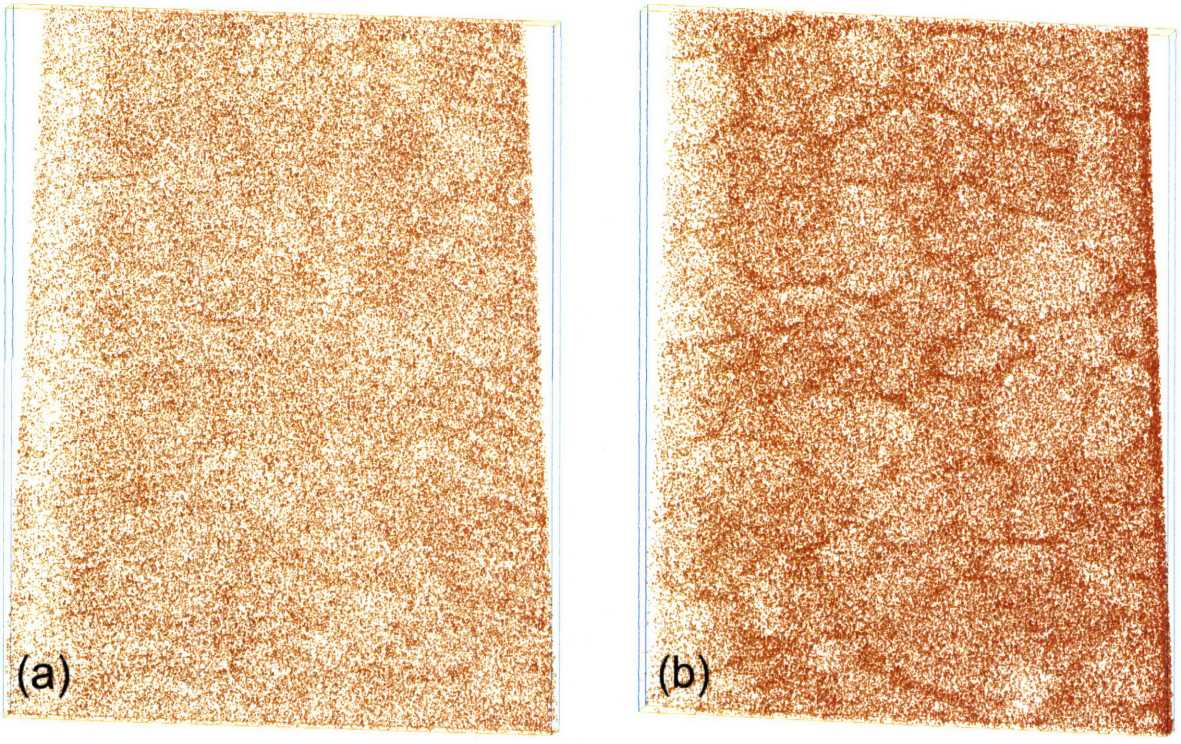

Figure 5.9: Atom probe maps plotting the positions of individual W atoms within a ~70 x 90 x 4 nm section of (a) as-deposited and (b) heat treated specimens having similar grain sizes of ~10 and 16 nm, respectively. The grain structure is clearly observed in (b) possibly owing to a structural change in the grain boundaries upon annealing; the data in (b) also appear in Appendix B.

the extent of segregation is similar in both materials (cf. Fig. 5.6) and, in addition, plotting Ni atoms instead of W yields a similar picture where the grain structure is clearly observed in the heat treated condition, but not in the as-deposited state. It is not entirely clear why annealing leads to such a significant effect in the sampling preference of the atom probe. However, it seems reasonable to speculate that this effect may be associated with a structural change in the grain boundaries upon annealing, because grain boundary atom density in Fig. 5.9(b) is clearly enhanced as compared to virtually any region in Fig. 5.9(a). Although this evidence is not quantitative, it is an intriguing complementary observation to the DSC and hardness measurements, all of which suggest that significant gain boundary relaxation occurs in these alloys during annealing.

5.6 Microstructure evolution map

At this point it is clear that numerous mechanisms may be active during the heat treatment of nanocrystalline alloys: grain growth, chemical ordering, grain boundary segregation, and grain boundary relaxation. In the preceding four sections we have attempted to characterize and quantify these phenomena in the Ni-W system. In what follows, we turn our attention to a more general discussion of these mechanisms by way of a microstructure evolution map; analytical models of the various mechanisms will be introduced and presented together to assess their relative activity in nanocrystalline structures. We emphasize that the following constructions serve only as a rough, order-of-magnitude comparison, and are primarily used as a means to discuss the general grain size dependent trends of microstructural evolution. We begin with a discussion of pure materials, considering only grain growth and boundary relaxation, followed by an analysis of alloys for which the additional complications of solute drag, grain boundary energy reduction, chemical ordering, and grain boundary segregation are introduced.

5.6.1 Grain growth and relaxation in pure metals

Numerous analytical investigations of grain growth have been presented in the literature. One of the most widely used is based on the early work of Burke and Turnbull [55, 222, 223] who expressed grain boundary velocity, v, as the product of a driving pressure, P, and grain boundary mobility, M, as:

$$v = P \cdot M = \frac{2\gamma_o}{r} \cdot M_o \exp\left[\frac{-Q_m}{RT}\right] \tag{5.1}$$

where P is assumed to be entirely curvature driven related to the grain boundary energy, γ_o, and grain radius, r, and the mobility is described by an Arrhenius relationship with M_o a pre-exponential factor, Q_m the activation energy for boundary migration, R the gas constant, and T the temperature. Relating grain boundary velocity to the time rate of change in grain radius (i.e. $v = dr/dt$ in Eq. (5.1)) and integrating, results in the familiar parabolic grain growth law:

$$d^2 - d_o^2 = 16\gamma_o M_o t \exp\left[\frac{-Q_m}{RT}\right] \tag{5.2}$$

where the grain size, $d = 2r$, has been introduced. Further expressing the final grain size as a multiple c of the initial grain size ($d = c \cdot d_o$), Eq. (5.2) can be recast as:

$$d_o = \left[\frac{16\gamma_o M_o t}{c^2 - 1}\right]^{1/2} \cdot \exp\left[\frac{-Q_m}{2RT}\right] \tag{5.3}$$

Plotting d_o as a function of either T or t in Eq. (5.3) therefore describes the temperature/time required to increase the starting grain size by a factor of c. Using this relationship we can compare grain growth kinetics over a wide range of starting grain sizes.

Grain boundary relaxation has been studied experimentally by a number of researchers using high resolution TEM to observe changes in the boundary structure upon annealing [71-73]. Several analytical models have been proposed to describe the associated kinetics of the relaxation process focusing on the climb and/or glide of excess dislocations away from grain boundaries, annihilating either in the lattice or adjacent triple junctions. Here we consider the recent model of Nazarov [224] who, using a continuum energy-balance approach, described the rate of grain boundary relaxation as:

$$\frac{d\Omega}{dt} = \frac{-163\delta D_b G V_m \Omega}{RTd^3} \tag{5.4}$$

where Ω is the density of grain boundary dislocations defined as $\Omega = b/h$ with b the burgers vector and h the spacing between dislocations in the boundary. The remaining terms in Eq. (5.4) are the grain boundary width δ, grain boundary diffusivity D_b, shear modulus G, and molar volume V_m. Assuming a constant grain size during boundary relaxation, introducing an Arrhenius relationship for D_b, and integrating, Eq. (5.4) can be expressed as:

$$d_o = \left[\frac{-163 G V_m \delta D_{o,b} t}{\ln(\Omega/\Omega_o) RT}\right]^{1/3} \cdot \exp\left[\frac{-Q_m}{3RT}\right] \tag{5.5}$$

with $D_{o,b}$ a pre-exponential term for grain boundary diffusivity and Ω/Ω_o representing the fraction of dislocations remaining in the boundary. Note that we assume the same activation energy for grain boundary diffusion in Eq. (5.5) as mobility in Eq. (5.3), a similarity that has been empirically established [55]. Thus, Eq. (5.5) describes the time/temperature required to achieve a given amount of relaxation, quantified by the ratio Ω/Ω_o, based on the initial grain size of the material.

Using Eqs. (5.3) and (5.5) we can compare the grain growth and grain boundary relaxation kinetics in pure nanocrystalline materials. Before proceeding, it is interesting to point out the difference between these two relationships in terms of the scaling behavior with grain size and temperature. Whereas grain growth follows a d^2 dependence, related to the driving pressure on a curved interface, grain boundary relaxation scales as d^3, consistent with the grain boundary volume fraction [20]. This difference implies a cross-over between the two mechanisms, with grain boundary relaxation becoming more important at the finest grain sizes. In addition, the exponential temperature dependence in Eqs. (5.3) and (5.5) includes activation terms with

energies proportional to $Q_m/2$ and $Q_m/3$ for grain growth and boundary relaxation, respectively, suggesting that relaxation should become more prevalent at low temperatures.

Equations (5.3) and (5.5) are plotted together in Fig. 5.10(a) as a function of temperature, for a constant time of 0.5 hr, labeled as "grain growth" (red) and "relaxation" (blue), respectively.

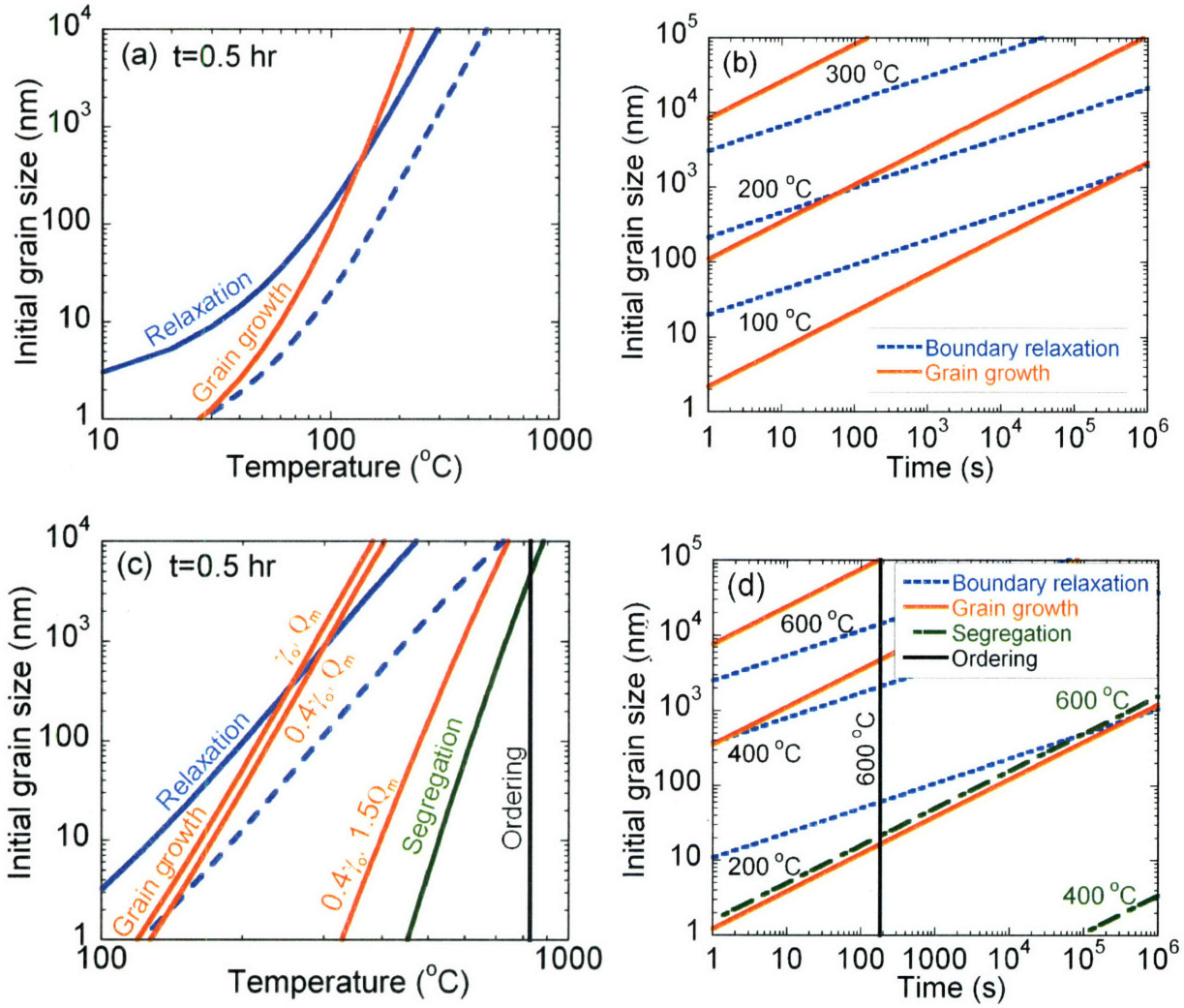

Figure 5.10: Microstructural evolution maps for (a, b) pure and (c, d) alloyed structures summarizing the relationship between initial grain size and (a, c) temperature and (b, d) time required for significant activation of grain boundary relaxation, grain growth, chemical ordering, and grain boundary segregation as described by Eqs. (5.3), (5.5), (5.6), and (5.7) with the constants given in Table 5.1. Solid lines in (a) and (c) represent the onset conditions for each mechanism, while the dashed line signifies the completion of grain boundary relaxation; all lines in (b) and (d) represent onset conditions. Kinetic ("γ_o, Q_m") and thermodynamic ("$0.4\gamma_o$, Q_m" and "$0.4\gamma_o$, $1.5Q_m$") contributions to grain growth in alloys are included in (c); see text for details.

Here, the solid lines are intended to represent the effective onset of each mechanism, as defined by values of $c=2$ in Eq. (5.3) and $\Omega/\Omega_o=0.99$ in Eq. (5.5), respectively; the dashed line indicates the significant completion of boundary relaxation as defined by $\Omega/\Omega_o=0.01$. The remaining constants used here are compiled in Table 5.1, representing typical values for pure Ni [21, 55, 225, 226]. It is interesting to note that the onset temperatures for both grain growth and boundary relaxation decrease with decreasing grain size in Fig. 5.10(a), indicating the relative instability of nanocrystalline materials. Perhaps more interestingly, a cross-over is predicted between these mechanisms at a grain size of ~400 nm, suggesting that grain boundary relaxation plays an important role in nanocrystalline materials and should actually precede grain growth. For larger, microcrystalline initial grain sizes the opposite is true where grain growth occurs before boundary relaxation.

As an alternative analysis, the onset conditions as described above are plotted as a function of time in Fig. 5.10(b) for a series of temperatures from 100-300 °C. The solid red lines here represent the onset of grain growth ($c=2$ in Eq. (5.3)), while the dashed blue lines describe grain boundary relaxation ($\Omega/\Omega_o=0.99$ in Eq. (5.5)). A similar cross-over trend is observed in

Table 5.1: Constants used to plot Eqs. (5.3), (5.5), (5.6) and (5.7) in Fig. 5.10(a-d), representing typical values for pure Ni and/or Ni-W alloys [21, 55, 225, 226]

Description	Symbol	Value	Units
Grain boundary energy	γ_o	1	J/m^2
Grain boundary mobility pre-exponential factor	M_o	0.01	$m^4/J\text{-}s$
Activation energy for boundary migration/diffusion, Ni	Q_m	114.7	kJ/mol
Activation energy for boundary migration/diffusion, Ni-W		149.7	
Shear modulus	G	76	GPa
Molar volume	V_m	6.6×10^{-6}	m^3/mol
Grain boundary thickness	δ	1	nm
Grain boundary diffusion pre-exponential factor	$D_{o,b}$	3.5×10^{-6}	m^2/s
Lattice diffusion pre-exponential factor	D_o	2.0×10^{-4}	m^2/s
Activation energy for lattice diffusion of W in Ni	$Q_{W(Ni)}$	299.4	kJ/mol

this figure where grain boundary relaxation occurs before grain growth at low temperatures and fine grain sizes. It is also evident from Fig. 5.10(b) that, because of the exponential dependence in Eqs. (5.3) and (5.5), temperature plays a critical role in controlling grain growth and boundary relaxation. Changing the constant 0.5 hr time assumed in Fig. 5.10(a) by several hours or more leads to only a minimal shift in the curves, while the relatively minor temperature changes covered in Fig. 5.10(b) lead to order-of-magnitude effects.

5.6.2 Alloying effects on grain growth

We now turn our attention to multi-component systems with the goal of developing a microstructural evolution map for alloys. We begin with a description of the kinetics and thermodynamics of grain growth in alloys, followed by a discussion of the additional mechanisms of chemical ordering and grain boundary segregation.

In the absence of second-phase precipitation, kinetic descriptions of grain growth in solid solutions typically invoke changes in the activation energy for grain boundary mobility, Q_m, to describe solute drag effects [55]. Physically, these changes are related to the enhancement or impediment of grain boundary diffusion that results from alloying, affecting grain boundary velocity through Eq. (5.1). Thus, in the present work we can model this kinetic effect by incorporating an appropriate activation energy for grain boundary diffusion in Ni-W, which we expect to be somewhat higher than that in pure Ni. Unfortunately, to the author's knowledge, this quantity has not been measured experimentally, so here we approximate it as one-half the activation energy for lattice diffusion of W in Ni [226]. This activation energy scaling between crystalline and grain boundary regions is well-established for pure metals [55, 225], and should give an approximate description of the kinetic contribution to stability in Ni-W.

Thermodynamic contributions to alloy stability have historically received less attention in the literature. Recently, however, it has been suggested that a reduction in grain boundary energy via solute segregation may effectively stabilize nanocrystalline structures by reducing the driving pressure in Eq. (5.1). As discussed in the introduction, Weissmuller [44], Kirchheim et al. [45], and others [46, 47, 100, 101] have even considered the limiting case where $\gamma = 0$ in Eq. (5.1)

would completely eliminate the driving force for grain growth, rendering thermodynamically stable polycrystals. Taking a more general approach, Krill et al. [50] considered the stability improvement that comes with a reduction in grain boundary energy, even if $\gamma = 0$ is not achieved, and used this notion to explain the impressive stability of nanocrystalline Pd-Zr. More specifically, Krill et al. estimated that a ~70% reduction in grain boundary energy leads to nanocrystalline Pd-Zr structures that are stable up to ~1500 °C. Our computer simulations in Chapter 2 suggest that a ~60% reduction in boundary energy may be achieved in nanocrystalline Ni-W alloys, and we may incorporate this energy reduction here to evaluate the thermodynamic contribution to stability.

The thermodynamic theories of stability mentioned above have focused on the first term in Eq. (5.1), and the associated reduction in driving pressure with decreasing grain boundary energy. However, it is likely that the mechanisms leading to grain boundary energy reduction will also affect the mobility, as the physical basis for both phenomena are closely related [227]. Grain boundary energy is reduced when solute atoms preferentially occupy high-energy sites, reducing the excess free volume, energy, and local strain in the intercrystalline regions. This effect, in turn, should lead to reduced mobility as diffusion becomes more frustrated in the boundary. This idea is similar to the well-established relationships between grain boundary disorientation angle, energy, and mobility in pure metals [21, 55]; as the disorientation of a low-angle boundary decreases, grain boundary energy drops while the activation energy for boundary migration increases. In systems such as pure Cu and Al [55], an increase in the activation energy of ~50-100% has been observed as the disorientation is decreased to low angles, and this effect is attributed to the same structural changes that account for a reduction in the boundary energy. Based on this analogy, it seems reasonable to suspect that a similar increase in activation energy might be realized when grain boundary energy reduction is achieved through alloying, rather than a change in grain orientation. This idea has received only limited attention in the literature [227], and suggests that thermodynamic effects may enter into both the pressure and mobility terms in Eqs. (5.1-5.3). We will evaluate the consequences of this in more detail later on.

5.6.3 Grain boundary segregation and chemical ordering

In addition to the grain growth effects discussed above, the mechanisms of chemical ordering and grain boundary segregation must also be evaluated for alloys. In general, these mechanisms add significant complication to our discussion as they are likely to interact with each other and with the grain growth and relaxation mechanisms addressed above. However, taking a simplified viewpoint and emphasizing again the schematic nature of the present discussion, we can proceed to approximate the characteristic time/temperature for these effects as well. Recognizing that both segregation and ordering are diffusive processes, we will approximately quantify these mechanisms with a characteristic diffusion distance, $Z = \sqrt{D \cdot t}$, where D describes the diffusivity of the segregating/ordering species. For chemical ordering, the characteristic distance is assumed to be independent of grain size, as atomic rearrangements take place in the bulk and are not likely to depend on this structural length-scale. Thus, ordering can simply be described as:

$$Z = [D_o t]^{1/2} \cdot \exp\left[\frac{-Q_{W(Ni)}}{2RT}\right] \tag{5.6}$$

where an Arrhenius relationship has again been introduced for the diffusivity with D_o a pre-exponential factor and $Q_{W(Ni)}$ the activation energy for lattice diffusion of W in Ni [226]. The onset condition for ordering is then determined by the characteristic distance Z over which solute atoms must diffuse.

To treat static grain boundary segregation we again resort to a characteristic diffusion distance but now assign it as some fraction of the grain size, describing a region bounding the interface acting as a source for solute atoms. Thus, unlike classical kinetic segregation models where grain size is assumed to be infinite [107, 129], this scaling approximately accounts for finite grain size effects that become important in the nanocrystalline regime [228]. With this assumed scaling, the condition for grain boundary segregation can be expressed as:

$$d_o = \frac{1}{s}[D_o t]^{1/2} \cdot \exp\left[\frac{-Q_{W(Ni)}}{2RT}\right] \tag{5.7}$$

where s represents the initial grain size fraction over which solute atoms must diffuse to cause grain boundary segregation. Note that Eq. (5.7) only describes static grain boundary segregation whereas a moving boundary during grain growth will likely serve as an additional route for solute enrichment [197, 229].

5.6.4 Alloy mechanism map

A schematic structural evolution map for alloys is presented in Fig. 5.10(c) as a function of temperature and (d) as a function of time, incorporating the grain boundary relaxation and grain growth analysis used earlier, and now introducing solute effects as well. The approximated activation energy for grain boundary diffusion in Ni-W, given in Table 5.1, has been included in Eq. (5.5) to describe grain boundary relaxation. To model grain growth, three onset curves are presented in Fig. 5.10(c) incorporating the kinetic and thermodynamic effects discussed in Section 5.6.2. The left-most curve, labeled "γ_o, Q_m", represents only the kinetic contribution of solute drag as described by the increased activation energy for grain boundary migration in Table 5.1. Thermodynamic effects are included in the remaining curves where the first, labeled "$0.4\gamma_o$, Q_m", contains a 60% reduction in the initial grain boundary energy only and the second, labeled "$0.4\gamma_o$, $1.5Q_m$" includes both a reduction in boundary energy and a 50% increase in the activation energy for boundary migration. The sequence of onset curves from left to right therefore captures the alloying contributions as introduced in Section 5.6.2. It is apparent in Fig. 5.10(c) that a 60% decrease in grain boundary energy has only a minimal effect on the grain growth prediction of Eq. (5.3), suggesting that this mechanism alone does not account for the improved stability of nanocrystalline Ni-W alloys. However, including an increase in the activation energy term, which, as suggested above, may coincide with grain boundary energy reduction, predicts a vast stability improvement; this will be discussed in relation to experimental data later on. Regardless of the particular curve chosen, grain boundary relaxation is found to precede grain growth for nanocrystalline grain sizes, similar to the results for pure Ni (Fig. 5.10(a)), suggesting that this mechanism remains important in alloys.

To evaluate chemical ordering and grain boundary segregation in Ni-W, appropriate values for the pre-exponential factor, D_o, and activation energy, $Q_{W(Ni)}$, describing diffusion are included in Table 5.1 [226]. Onset curves are plotted for these mechanisms in Fig. 5.10(c, d) defined by values of $Z = 0.35$ nm in Eq. (5.6) and $s = 0.01$ in Eq. (5.7) for ordering and segregation, respectively. Thus, in the description of alloys, ordering will commence when W and Ni atoms can diffuse a distance of ~1 lattice parameter, while segregation is likely if solutes can diffuse a distance of $0.01\,d_o$ into the grain boundary. It is apparent in Fig. 5.10(c) that these additional mechanisms occur secondary to relaxation and grain growth for the finest nanocrystalline grain sizes. Thus, static grain boundary segregation as assumed in Eq. (5.7) is not expected to occur in nanocrystalline structures, where segregation via moving boundaries during grain growth is a more likely scenario [197, 229]. Also, chemical ordering is unlikely before a significant increase in grain size, consistent with the experimental findings of the present work.

The various mechanisms in alloys are plotted as a function of time in Fig. 5.10(d) where similar features are observed compared to the pure system in (b); note that, for clarity, only the onset curves for grain growth incorporating kinetic effects are plotted here (i.e. "γ_o, Q_m" in Fig. 5.10(c)). Although the temperatures are higher in Fig. 5.10(d), a cross-over from grain boundary relaxation to grain growth is observed in the range of 200-600 °C. Also, the ordering and segregation mechanisms, some of which do not appear at lower temperatures on this plot, are found to be secondary over the entire range of initial grain sizes.

Despite the various assumptions inherent in the construction of Fig. 5.10(a-d), the synthesis of mechanisms provides a framework in which to appreciate the complex microstructural changes that occur during the heating of nanocrystalline materials. As a summary, Fig. 5.11 combines the results of Fig. 5.10(a) and (c) to directly contrast the structural evolution in pure metals and alloys. The shaded regions in Fig. 5.11 encompass the mechanisms for alloyed systems, which occur at significantly higher temperatures compared to those in pure structures. Note that only one onset curve is shown for alloy grain growth, incorporating both a thermodynamic reduction in grain boundary energy and increase in the activation energy for migration ("$0.4\gamma_o$, $1.5Q_m$" in Fig. 5.10(c)).

Although Fig. 5.11 serves mainly as a schematic, dependent on the assumptions of Eqs. (5.3), (5.5), (5.6), (5.7) and the constants in Table 5.1, it is instructive to qualitatively compare the predictions with available experimental data in the literature. For example, da Silva et al. [58] and Klement et al. [61] demonstrated that boundary relaxation occurs in pure Ni in the range of ~60-80 °C for grain sizes of ~10-50 nm. For nanocrystalline Ni-W alloys, our DSC measurements (Fig. 5.7) show that relaxation commences at somewhat higher temperatures, above ~120 °C. These findings line up reasonably well with the predictions of Fig. 5.11 suggesting that this type of analysis (Eq. (5.5)) may be applied to interpret relaxation in nanocrystalline materials. Onset temperatures for grain growth in pure nanocrystalline Ni have been measured at ~200 °C, somewhat higher than the prediction of Fig. 5.11 but reasonable considering the order-of-magnitude nature of this discussion. For grain growth in alloys, the experimental results of the present work have shown that nanocrystalline Ni-W is stable up to ~500 °C (cf. Fig. 5.2). Here, it is obvious that the onset curve incorporating thermodynamic effects, mainly an increase in the activation energy for boundary migration, leads to a good fit

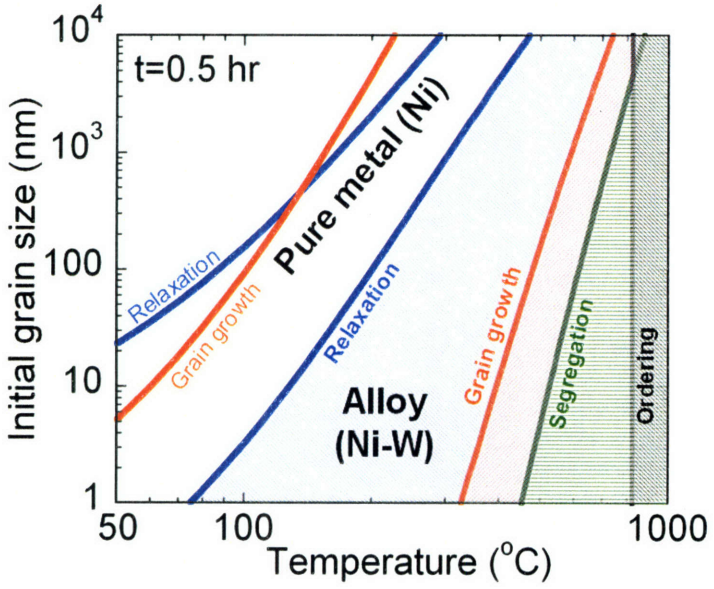

Figure 5.11: Combining the results of Fig. 5.10(a) and (c) showing the improved thermal stability of alloys (shaded regions) as compared to pure systems.

with experiments. This finding lends support to the coupled grain boundary energy reduction-increased activation energy argument discussed above. However, there is significant uncertainty

in the activation energy for grain boundary diffusion in Ni-W and more work should be done in this area to more clearly distinguish these two kinetic effects. Finally, extensive chemical ordering has been observed in the present work only after significant grain growth at temperatures above ~750 °C (cf. Fig. 5.1), matching well with the predictions of Fig. 5.11. Although these constructions mainly serve as order-of-magnitude approximations, the reasonable agreement with experiments is encouraging and suggests that this technique may be used to evaluate the structural evolution in pure and alloyed nanocrystalline specimens.

5.7 Concluding remarks

In the present chapter we have used a variety of techniques to assess the microstructural evolution during heat treatment of nanocrystalline Ni-W. Aside from routine grain size measurements, characterization of the solute distribution and evidence for grain boundary relaxation provide a more complete picture of the processes activated during annealing. The main findings of the present work can be summarized as follows:

- The grain size of nanocrystalline Ni-W remains stable over 24 hrs at temperatures up to ~500 °C; higher temperatures result in normal grain growth.
- A chemical ordering transition is observed at sufficiently high temperatures following a sequence from disorder, to short range order, to long range order, similar to that reported in coarse-grained alloys.
- The extent of grain boundary segregation remains fairly constant after annealing with no significant enrichment or depletion of solute in the grain boundaries beyond that expected as a consequence of grain growth.
- Relaxation of the grain boundaries is manifested through a large heat release in the absence of grain growth, and significant hardening at the finest nanocrystalline grain sizes.

A general microstructural evolution map was also constructed by considering various analytical models describing the mechanisms of grain growth, grain boundary relaxation, chemical ordering, and grain boundary segregation. Plotting onset curves for these mechanisms allows an order-of-magnitude comparison of their activity as a function of grain size, temperature, and time.

Chapter 6: Applications of the reverse pulsing synthesis technique

A main outcome of the present work involves the ability to precisely tailor nanocrystalline grain size in Ni-W alloys through simple adjustment of the electrodeposition parameters. In particular, it has been shown that a periodic reverse pulse in the electrodeposition current can be used to control the composition (cf. Fig. 3.4) and, in turn, grain size (cf. Fig. 3.7) of high quality specimens. Up to now we have aimed at a scientific understanding of the grain size-composition relationship in Ni-W, and the resulting stability of nanocrystalline structures. In the present chapter we apply the reverse pulsing technique in order to illustrate the potential benefit of this new method for both fundamental scientific investigations as well as practical applications. We begin by examining a scaling law that has recently come under scrutiny in the nanocrystalline regime. Following this, we show how the reverse pulsing technique can be used to create patterned nanostructures and functionally graded materials. Some of the work presented here is included in Ref. [162].

6.1 Hall-Petch breakdown

Control of grain size is highly desirable for probing properties at the nanoscale where much attention has recently been focused on the breakdown of classical scaling laws [2, 5, 6, 9, 14, 26, 76, 230-232]. As mentioned in the introduction, the Hall-Petch relationship has received perhaps the most attention and there has been considerable debate over its validity at grain sizes near or below ~10 nm [9, 14, 26, 27, 29, 76]. Fueling this debate is a notable lack of experimental data, as evidenced and discussed in relation to Fig. 1.2, along with the uncertain quality and stability of experimental nanocrystalline specimens. With our new degree of control in the Ni-W system we can now access a wide range of grain sizes, convincingly spanning the suspected crossover from conventional scaling to breakdown behavior. Experimental data for specimens synthesized using the techniques outlined in Chapter 3 are shown as red squares in Fig. 6.1, along with available data from the literature introduced in Fig. 1.2. The new data in Ni-W capture both Hall-Petch strengthening at large grain sizes, as well as an unambiguous demonstration of scaling breakdown for grain sizes below ~10 nm. Although additional complications arise in interpreting this data due to the effects of solid solution strengthening, it can be shown that this

mechanism likely accounts for less than ~0.05 GPa of hardening over the composition range considered here (~2–25 at%W) [95]. Thus, grain refinement may be regarded as the main contributor to strengthening in Fig. 6.1 where a ~5 GPa increase in hardness is observed, two orders of magnitude greater than the solid solution effect. Furthermore, the present Ni-W alloys offer the possibility of examining properties in specimens that are in a relatively stable state over the entire range of grain sizes, as compared to pure Ni where nanoscale grain refinement represents an increasing departure from equilibrium.

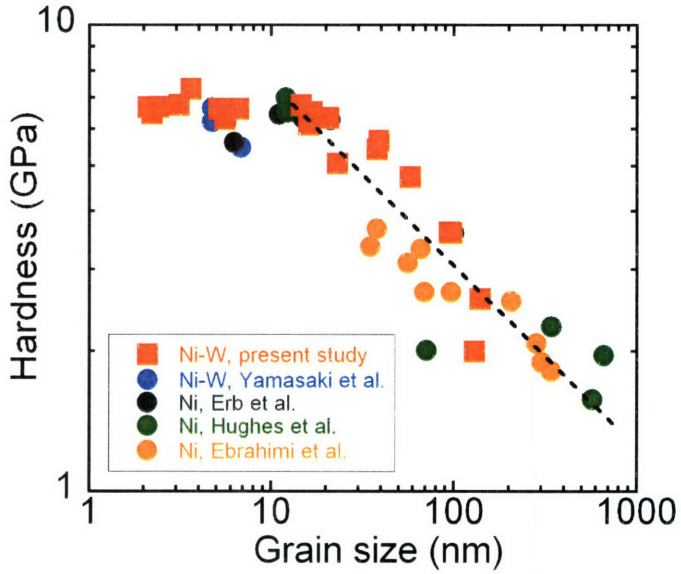

Figure 6.1: Hardness plotted as a function of grain size for the present Ni-W alloys along with data from the literature introduced in Fig. 1.2 [31-34]. The present study convincingly demonstrates Hall-Petch strengthening, followed by a plateau in hardness for grain sizes less than ~10 nm.

The Ni-W hardness data in Fig. 6.1 includes specimens in the as-deposited state, demonstrating one of the major benefits of the reverse pulsing technique in the ability to synthesize specimens over a wide range of grain sizes. As an alternative approach, heat treatment may also be used to tailor grain size where a single fine-grained specimen is annealed through various time/temperature schedules to access a range of nanocrystalline structures. As discussed in Chapter 5, this approach has been used in a number of studies to measure grain size-dependent properties. However, serious complications may arise if researchers neglect other structural changes that occur in additional to grain growth, most notably grain boundary relaxation as discussed in relation to Fig. 5.8.

With the present synthesis technique we have the unique ability to investigate property dependence where grain size is achieved in both the as-deposited state and through heat treatment. For example, the open-hatched points in Fig. 6.2 represent hardness data taken from specimens in the as-deposited condition (as presented in Fig. 6.1); the dashed line is a best-fit to this data and serves as a guide to the eye. In addition, hardness data are included for specimens subject to isothermal annealing, as presented in Appendix C, with three different as-deposited grain sizes of $d_o = 3$, 20, and 70 nm. Points where grain size remains largely unaffected by heat treatment were used in Fig. 5.8 as part of the grain boundary relaxation analysis, and here we include all the isothermal experiments to investigate hardness trends with grain growth; relatively larger grain sizes in Fig. 6.2 are achieved through longer time and/or higher temperature exposures. Independent of the specific heat treatment leading to coarsening, several interesting trends can be observed in this figure. First, all of the hardness data for the heat treated $d_o = 3$ and 20 nm specimens (red circles and blue squares, respectively) lie above the corresponding as-deposited values, while the $d_o = 70$ nm data (green points) roughly follow the Hall-Petch trend at larger grain sizes. In fact, both the $d_o = 3$ and 20 nm data sets exhibit inverse Hall-Petch behavior where hardness initially increases with increasing grain size. In both cases, hardness peaks at a grain size of ~30 nm, followed by a decrease in hardness with further grain growth; note that the maximum hardening is achieved for the 3 nm heat treated specimen, with values above 10 GPa.

Figure 6.2 demonstrates the important influence that prior temperature exposure can have on properties in the nanocrystalline regime. In line with previous experimental [77, 219] and theoretical [76, 220] works, as discussed in detail in Chapter 5, strength scaling can vary widely depending on specimen condition and thermal history. For the Ni-W data in particular, several complicating mechanisms likely contribute to the trends observed in Fig. 6.2. Perhaps the most important is grain boundary relaxation, which was shown in Chapter 5 to have a significant influence on properties for the finest nanocrystalline grain sizes (cf. Fig. 5.8). As introduced in Ref. [76], inverse Hall-Petch behavior and significant hardening in the heat treated $d_o = 3$ and 20 nm specimens may be a fundamental result of grain boundary relaxation, which hinders grain

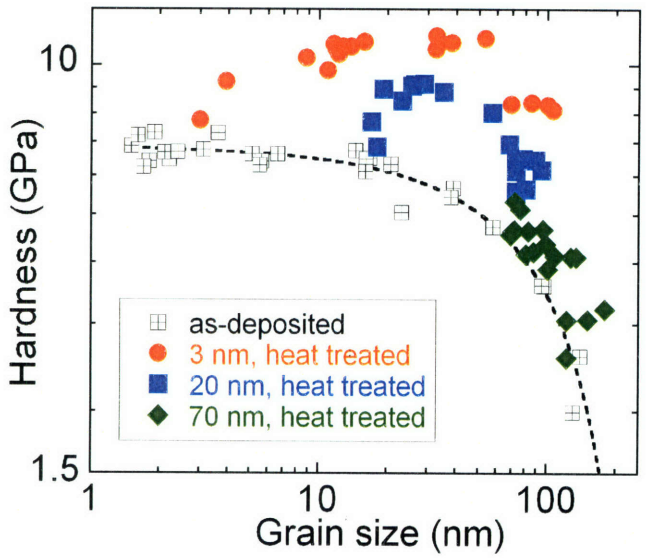

Figure 6.2: Hardness as a function of grain size for specimens in the as-deposited condition, as well as those subject to isothermal annealing experiments from starting grain sizes of 3, 20, and 70 nm; raw data are compiled in Appendix C. Inverse Hall-Petch behavior is observed for the heat-treated specimens with grain size less than ~30 nm.

boundary sliding mechanisms expected to be active in nanocrystalline specimens. However, alloying effects, in particular the tendency for chemical ordering, add further difficulties in interpreting the data of Fig. 6.2. Because finer grain size specimens contain more W, the maximum hardening observed for the $d_o = 3$ and 20 nm specimens may at least partially derive from chemical ordering, in addition to grain boundary relaxation. In both cases, however, high hardness values are achieved in specimens where only short-range chemical ordering is detected in TEM experiments (cf. Fig. 5.5). In line with the solid solution strengthening argument of Fig. 6.1, short range chemical ordering alone is not expected to account for a ~3–5 GPa hardening effect [233, 234], suggesting that grain boundary relaxation is likely the dominant contributor.

In light of the above discussion, data such as those in Fig. 6.2 may be useful for studies of strengthening and deformation mechanisms in nanocrystalline alloys where a number of important effects, including composition, grain size, and grain boundary relaxation, can be incorporated. Future work should be directed in this area to examine these effects in more detail.

6.2 Patterned nanostructures

In addition to controlling grain size in a monolithic specimen, the reverse pulsing approach also enables a new class of nanostructured solids where grain size and properties are patterned through the specimen thickness. In principle, traditional deposition procedures could be applied in a series of discrete steps involving different temperatures, current densities, plating bath chemistries, etc., in order to build up a series of different layers [235]. However, here we propose an in-situ approach to the fabrication of such materials, and to our knowledge this procedure has not been used to create graded or layered nanocrystalline materials previously. By effecting changes in the reverse pulsing conditions in real-time, it is possible to deposit a sequence of tailored layers or smooth gradations in composition and grain size. In principle, any conceivable one-dimensional pattern can be produced, on scales ranging from nanometers to millimeters. Figure 6.3 shows two specimens exemplifying this capability; the specimen in (a) comprises eight layers of increasing grain size (from ~10 to ~60 nm), while that in (b) has a composite structure of alternating ~7 and ~70 nm grain size regions. For the graded specimen in Fig. 6.3(a), a serial-sectioning x-ray study was undertaken to profile the grain size of the deposit through its thickness (cf. Fig. 6.4). For this study, layers ~10 μm in thickness were successively removed from the surface of the deposit by mechanical polishing. After each polishing step, an x-ray scan was performed on the polished surface and grain size was quantified using the line profile procedure introduced in Chapter 3; the penetration depth of the x-rays was ~10-15 μm. In Fig. 6.3(b) grain size was estimated based on composition using the data in Fig. 3.7.

In addition to changes in composition and structure, grain size patterning permits customizable material properties, such as the nanoindentation hardness measurements also shown in Fig. 6.3. Nanoindentation experiments were performed on polished cross-sections of the graded and layered specimens, using a Hysitron TriboIndenter. A Berkovich tip was used with a linear loading function reaching a maximum of 10 mN over 10 seconds; typical indents were ~150 nm deep and hardness was calculated from the load-displacement curves using standard methods and an empirically calibrated tip area function [236]. Six hardness profiles through the deposit thickness were obtained on each specimen by indenting along a line from the substrate to the surface, with indents spaced 6 μm apart, and each data point in Fig. 6.3 is an average over these tests. Such patterned structures may be 'functionally graded' as in Fig. 6.3(a), to impart superior

surface characteristics and allow smooth property transitions to the bulk. Alternatively, laminate structures such as that shown in Fig. 6.3(b) may be useful for balancing two desirable properties individually optimal at different grain sizes.

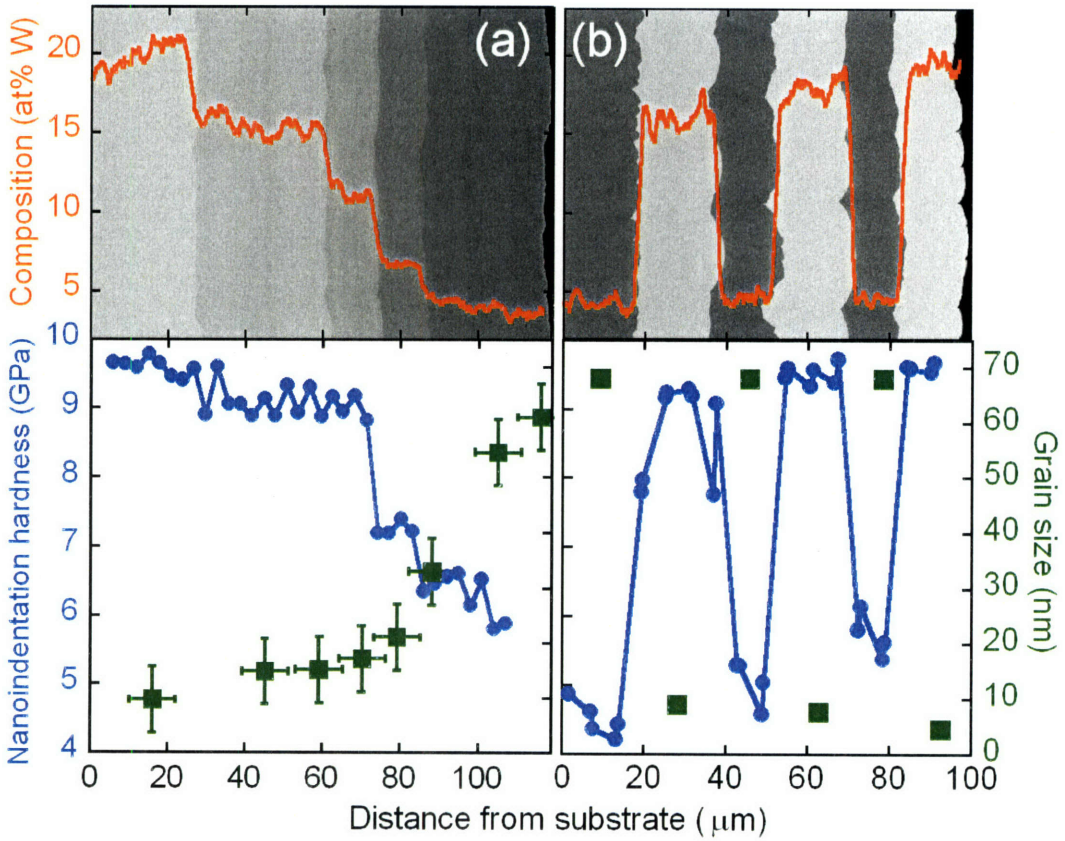

Figure 6.3: Patterned nanocrystalline electrodeposits synthesized using the periodic reverse pulsing technique of Chapter 3. Backscatter SEM images and composition line scans are shown at the top of both figures. Nanoindentation hardness (blue circles) and grain size (green squares) profiles show the level of structure and property control available using this method. The specimen in (a) comprises eight layers of monotonically decreasing W content, while that in (b) contains alternating layers of low and high W content. Grain size measurements in (a) were obtained from a serial sectioning X-ray study, while those in (b) are an estimate based on the composition.

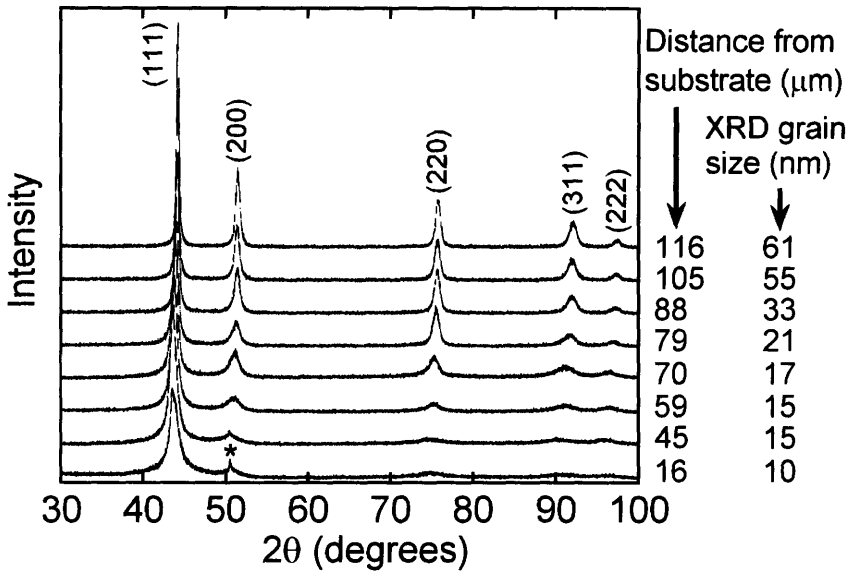

Figure 6.4: Serial XRD study conducted on the eight layer specimen of Figure 6.3(a). Grain size calculated using the integral breadth method is shown along with the corresponding distance from the substrate. The star symbol (*) on the pattern closest to the substrate indicates the emergence of a copper diffraction peak as the X-rays penetrate the Ni-W specimen and begin to sample the substrate.

6.3 Concluding remarks

The examples above briefly demonstrate the potential benefit of the reverse pulsing method towards both fundamental scientific investigations and practical applications. It is expected that the ability to precisely tailor nanocrystalline grain size in Ni-W, combined with high specimen quality, will lead to detailed property studies in the future. This includes not only mechanical behavior, but also magnetic, electrical, and corrosion properties, among others, that show grain size dependence. In addition, the ability to pattern Ni-W nanostructures has already lead to interesting scientific inquires related to the indentation and scratch response of graded materials [237]. Other studies involving residual stress in multilayers, fatigue crack propagation, and corrosion resistance, to name a few, should also be possible. Finally, direct application of nanocrystalline Ni-W as a functional coating, taking advantage of its high hardness, luster, and scratch resistance, should find many practical uses. In fact, this technology is currently being commercialized as an alternative to hard chromium, having important environmental benefits as well as superior properties.

Conclusions

Control of grain size has proven to be a significant barrier towards the understanding and application of nanocrystalline materials. Therefore, a main goal of this work was to develop a method to precisely tailor this length-scale by exploiting the thermodynamics of alloying. Existing theories have suggested that stable nanocrystalline structures can be obtained where the energy penalty from intercrystalline regions is reduced through grain boundary segregation. Here we have used atomistic computer simulations to evaluate this phenomenon and explore the potential for nanostructure stabilization in Ni-W. Detailed investigation of the solute distribution and energetics revealed that a decrease in grain boundary energy occurs in this system, owing to the tendency for grain boundary segregation. In addition, atomic-scale details of the ordering behavior revealed that the fine structural length-scale leads to a chemical disordering effect, which significantly impacts the energetics of nanocrystalline materials.

Based on the computer simulation results, experiments were performed to synthesize Ni-W specimens over a broad range of compositions. An electrodeposition technique was developed where adjustments to the applied current waveform allow for precise composition control. Structural characterization revealed that specimens synthesized using this technique were nanocrystalline, and that grain size scaled with W content as predicted by thermodynamic theories of nanostructure stabilization. High quality specimens with any grain size in the range of ~150-2 nm can be precisely tailored through judicious control of the electrodeposition parameters.

To further investigate the origins of the observed composition-grain size relationship in Ni-W, detailed atom probe tomography experiments were performed to assess the solute distribution in experimental specimens. Through statistical analysis, a subtle extent of grain boundary segregation was measured that was in line with the computer simulation results. Incorporating the findings from simulations and experiments, it was concluded that nanocrystalline Ni-W likely benefits from a reduction in grain boundary energy; however, contrary to previous theories, nanocrystalline Ni-W does not reside in a thermodynamically stable state.

To assess the stability of experimental specimens, elevated temperature annealing experiments were performed in combination with a variety of experimental characterization techniques. Grain size was found to be stable up to ~500 °C, although evidence was presented for a significant structural relaxation in the grain boundaries at lower temperatures. This relaxation leads to hardening of the finest nanocrystalline grain sizes, an important effect that has received little attention in the literature. In addition to grain growth and boundary relaxation, the chemical ordering evolution in Ni-W was evaluated and shown to follow a similar sequence as that reported for coarse-grained alloys. Grain boundary segregation tendency, measured through additional atom probe tomography experiments, showed little change in comparison to the as-deposited state. As a summary, analytical model of the various mechanisms activated during annealing were introduced in a microstructure evolution map, providing a convenient means to appreciate the complex structural and chemical changes that occur in nanocrystalline alloys.

Lastly, the synthesis technique developed in this work was applied in several specific examples in order to highlight the potential benefit of this new method. With precise control over grain size, we demonstrated the direct study of a scaling law that has shown anomalous behavior in the nanocrystalline regime. We also extended the synthesis technique to the production of patterned nanostructures, where functionally graded or composite coatings can be formed in any conceivable combination. Other benefits of this capability were pointed out in terms of both fundamental studies and practical applications.

In closing, the present work has shown that nanocrystalline grain size can be precisely tailored in Ni-W alloys through judicious control of the synthesis parameters. Fundamental understanding of the structure and stability of these alloys was gained through both atomistic computer simulations and advanced experimental techniques. We expect that this unprecedented level of control over the structure will open the door to new studies of material physics at the finest possible length-scales. We are also optimistic that the work presented here will ultimately promote the useful application of nanocrystalline materials.

Directions for future work

This thesis research represents a significant advancement towards grain size control and an understanding of the thermal stability in nanocrystalline alloys. However, future work will help to further elucidate the mechanisms discussed here, as well as apply the methods developed to important scientific questions. In particular, studies should be directed in the following specific areas:

- The atomistic computer simulations of Chapter 2 were focused on a rather narrow range of nanocrystalline grain sizes (2-4 nm) due, in large part, to computational constraints. It would be beneficial to simulate larger grain sizes in order to compare with the length-scales achieved in experiments. Work in this area is currently underway, taking advantage of columnar, rather than fully three-dimensional grain structures. Reducing the dimensions in this way allows for simulation of grain sizes up to ~20 nm while still incorporating bulk behavior. It is anticipated that these simulations will shed further light on the energetics, chemical ordering behavior, and segregation tendency in Ni-W specimens.
- As mentioned in Chapter 3, the methods developed in this work for Ni-W should also be applicable to other alloy systems. Extending the computer simulation technique of Chapter 2 should afford an understanding of alloy selection by substituting appropriate multi-body potentials. In this way, binary or higher alloy systems could be screened before attempting to synthesize experimental specimens. This work would also shed light on the relationship between solute solubility, segregation tendency, and the resulting potential for nanostructure stability.
- Based on the selection of potential candidates from computer simulation, the reverse pulsing electrodeposition technique could be applied to specific alloy systems to investigate processing/composition/structure relationships. This would extend the range of materials available for both fundamental studies and applications.
- Although an electrochemical mechanism for the observed reverse pulsing-composition relationship was suggested in Chapter 3, it was not the main focus of this thesis. Future

studies involving detailed electrochemical measurements would help to fully appreciate this phenomenon, and the reactions occurring at or near the cathode during deposition.

- The thermal stability study of Chapter 5 was intended to provide a complete picture of the microstructural evolution during annealing of nanocrystalline Ni-W. One of the more interesting outcomes of this work was the clear evidence for grain boundary relaxation, affecting not only the DSC results but also significantly influencing the hardness of nanocrystalline specimens. This mechanism deserves further investigation involving, in particular, direct observation via high resolution TEM; to the author's knowledge no work to date has conducted such experiments in nanocrystalline alloys. This type of direct evidence would unequivocally prove the importance of grain boundary relaxation for the finest nanocrystalline grain sizes.
- Additional investigations of grain boundary relaxation via atomistic computer simulation would help to further understand this important mechanism. For example, molecular dynamics studies of the relaxation process would provide a detailed view of the associated kinetics and structural transformations involved in the process. Also, simulating the mechanical properties of bulk nanocrystalline structures, where the grain boundaries reside in various relaxed states, would provide insight on the hardness measurements obtained in the present work (cf. Figs. 5.8 and 6.2).
- Finally, the most immediate benefit will likely come from additional length scale-dependent property investigations using the synthesis technique developed in this thesis. Detailed studies of any property – mechanical, electrical, magnetic, environmental, etc. – will benefit from the ability to precisely control the finest nanocrystalline grain sizes.

Appendix A: Electrodeposition experiments

Table A.1: Synthesis conditions and characterization results for all electrodeposition experiments performed relevant to this work; note that the table is continued on the next page. Details of the electrodeposition process, including a schematic of the set-up (cf. Fig. 3.1), materials used, and definition of the waveform variables (cf. Fig. 3.3), along with the characterization procedures, can be found in Chapter 3. Experiments are sorted according to the resulting deposit composition. The TEM column indicates those sample conditions inspected using this technique, and the notes column contains additional details including identification of those experiments used for the studies in Figs. 3.2 and 3.4(a, b) of Chapter 3. The electrolyte bath composition used for all experiments is given in Table 3.1.

	Forward Pulse			Reverse Pulse						
Bath Temp. (°C)	Current Density (A/cm^2)	t_{on} (ms)	t_{off} (ms)	Current Density (A/cm^2)	t_{on} (ms)	Composition (at%W)	XRD Grain Size (nm)	Hardness (GPa)	TEM	Notes
60	0.06	20	-	0.06	8	1.1	98			
60	0.15	5	-	0.15	2	1.5	130	2.00		
60	0.10	20	-	0.10	5	1.5	140	2.58		
75	0.20	20	-	0.30	3	2.5	95	3.60	X	b
75	0.20	20	-	0.05	9	3.7	84			c
60	0.15	5	-	0.08	2	4.3	97	3.59		
75	0.20	20	-	0.20	3	4.4	58	4.73	X	b
60	1.00	5	45	-	-	5.1				
40	0.15	50	50	-	-	5.6	39	5.67		
75	0.20	20	-	0.05	6	5.8	73			c
75	0.20	20	-	0.05	5	7.7	56		X	c
75	0.20	20	-	0.15	3	7.7	38	5.43	X	b
45	0.20	DC				8.9	23	5.06		a
40	0.15	20	20	-	-	9.0	14			d
60	0.15	5	45	-	-	12.5				
55	0.20	DC				13.0	16	6.12		a
75	0.20	20	-	0.05	4	13.3	19			c
60	0.10	20	20	-	-	13.9				
60	0.30	1	90	-	-	14.3	7			
75	0.20	20	-	0.10	3	15.0	21	6.34	X	b
60	0.15	50	50	-	-	15.7	17	6.51		
60	0.03	40	-	0.03	2	16.0	4			
60	0.03	40	-	0.03	2	16.0	4			d
75	0.20	20	-	0.05	3	16.5	16	6.48	X	b, c
60	0.03	DC				17.3	5	6.63		
60	0.03	DC				17.5	3			d
70	0.15	20	20	-	-	17.5				
60	0.15	DC				17.8	15	6.75		

	Forward Pulse			Reverse Pulse						
Bath Temp. (°C)	Current Density (A/cm^2)	t_{on} (ms)	t_{off} (ms)	Current Density (A/cm^2)	t_{on} (ms)	Composition (at%W)	XRD Grain Size (nm)	Hardness (GPa)	TEM	Notes
60	0.02	DC				17.8	4			
70	0.20	20	20	-	-	18.2				
85	1.00	5	45	-	-	18.9				
60	0.15	50	50	-	-	18.9	7	6.63		d
65	0.20	DC				19.1	6	6.41		a
83	0.03	DC				19.3	4			
75	0.15	50	50	-	-	20.8	4	7.31		
75	0.20	20	-	0.002	2	21.0	6	6.30		
85	0.20	50	-	0.005	1	22.8				
60	0.15	5	40	-	-	22.8	3			d
75	0.20	DC				23.0	3	6.70	X	a, b, c
60	0.15	DC				23.3	2	6.68		d
75	0.35	DC				23.5	2	6.87		
75	0.35	34	67	-	-	23.7	3	6.76		
85	0.20	20	20	-	-	23.9	2			
75	0.35	75	25	-	-	24.2	2	6.41		
60	0.15	20	20	-	-	24.3	2	6.24		
60	0.15	20	20	-	-	24.3	2	6.24		d
60	0.15	18	6	-	-	24.7	2	6.47		
60	0.15	18	6	-	-	24.7	2	6.47		d
75	0.15	DC				24.8	2	7.32		
60	0.1	5	10	-	-	25.4	2			d
83	0.35	DC				26.2	2	7.22		
85	0.2	DC				26.2	3			a
83	0.15	DC				26.5	2			
75	0.20	40	-	0.01	1		2			
75	0.20	40	-	0.03	1		2			
75	0.20	40	-	0.1	1		2			
75	0.20	20	-	0.1	1		2			
75	0.20	20	-	0.03	3		17			

a: experiment used in bath temperature study on composition (Fig. 3.2)

b: experiment used in reverse pulse current density study on composition (Fig. 3.4(a))

c: experiment used in reverse pulse time study on composition (Fig. 3.4(b))

d: cathode slowly rotated during deposition

Appendix B: Measuring grain boundary segregation in heat-treated nanocrystalline alloys: Direct validation of statistical techniques using atom probe tomography

In Chapter 4 we introduced a statistical procedure to measure the grain interior and grain boundary composition in nanocrystalline alloys without prior knowledge of the structure or exact position of individual grain boundaries. In what follows we perform identical procedures to quantify the average level of grain boundary segregation in heat-treated nanocrystalline Ni-W alloys. In addition, grain boundary locations for these specimens are uniquely identified in the atom probe data due to a residual effect of the technique itself. Using this information, a comparison is made between the statistical approach and direct measurements of grain boundary composition, showing good agreement between the methods. The work that follows has been published in Ref. [238].

The two Ni-W specimens examined here were electrodeposited following the procedures of Chapter 3, and exhibited an average grain size (composition) of ~3 nm (21 at%W) and ~20 nm (13 at%W) in the as-deposited condition. After deposition, the specimens were subject to short heat-treatments (3 hr and 0.5 hr, respectively) at 600 °C to induce slight grain growth. Bright field TEM images and inset selected area diffraction patterns, reproduced from Chapter 5, are shown in Fig. B.1; the approximate grain size of each is (a) 16 nm and (b) 28 nm (Chapters 3 and 5 provide details of the TEM specimen preparation and observation techniques, and the x-ray line broadening method used to quantitatively assess the average grain sizes reported here.) Atom probe experiments were performed on these specimens at Oak Ridge National Laboratory using an Imago Scientific Instruments Local Electrode Atom Probe. In what follows, the statistical approach of Chapter 4 is employed to evaluate grain boundary segregation in these specimens, followed by a direct comparison of local segregation measurements at known grain boundary positions.

In the statistical approach, composition profiles are constructed along the length of each acquired atom probe data set using a moving average over 100 atoms within a 2 x 2 nm cross-sectional

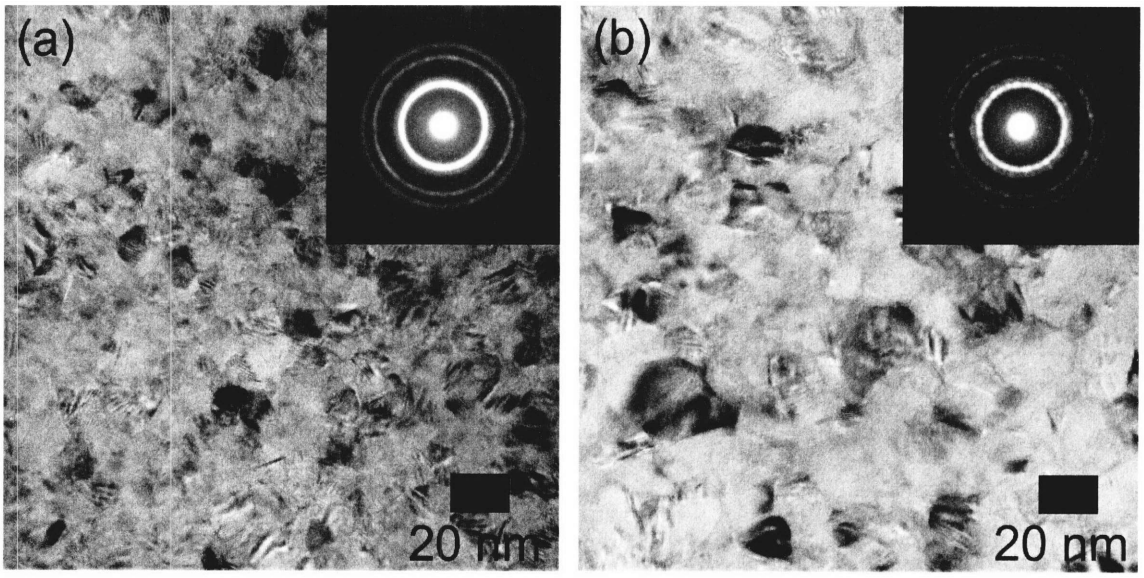

Figure B.1: Bright field transmission electron microscopy images and inset selected area diffraction patterns for the heat treated (a) ~16 nm (b) ~28 nm grain size Ni-W alloys containing approximately 21 and 13 at%W, respectively.

area. For the case of grain boundary segregation, a characteristic wavelength is expected in these profiles, and should be similar to the measured grain size of the alloy. As shown in Fig. B.2(a) for the ~16 nm grain size specimen, the composition exhibits fluctuations with a wavelength of ~20 nm. Similarly, the composition profile presented in Fig. B.2(c) for the ~28 nm grain size specimen exhibits fluctuations of ~30 nm. For a more statistically robust measure of this length-scale a 3-dimensional autocorrelation function analysis is performed over the entire atom probe data-set. This analysis is presented in Fig. B.2(b) and (d) for the 16 and 28 nm grain size specimens, where the characteristic wavelength is clearly observed as the first non-trivial maximum in the autocorrelation function. For comparison, an arrow is drawn at the position of the grain size for each specimen. The mutual agreement between these measurements in both alloys is strong evidence for grain boundary segregation of W.

The average composition of grain boundary and grain interior regions can also be assessed from the atom probe data using statistical methods. As described in Chapter 4, a composition distribution is constructed by dividing the structure into blocks containing ~100 atoms each and counting the frequency of composition observations amongst these blocks. The results of this

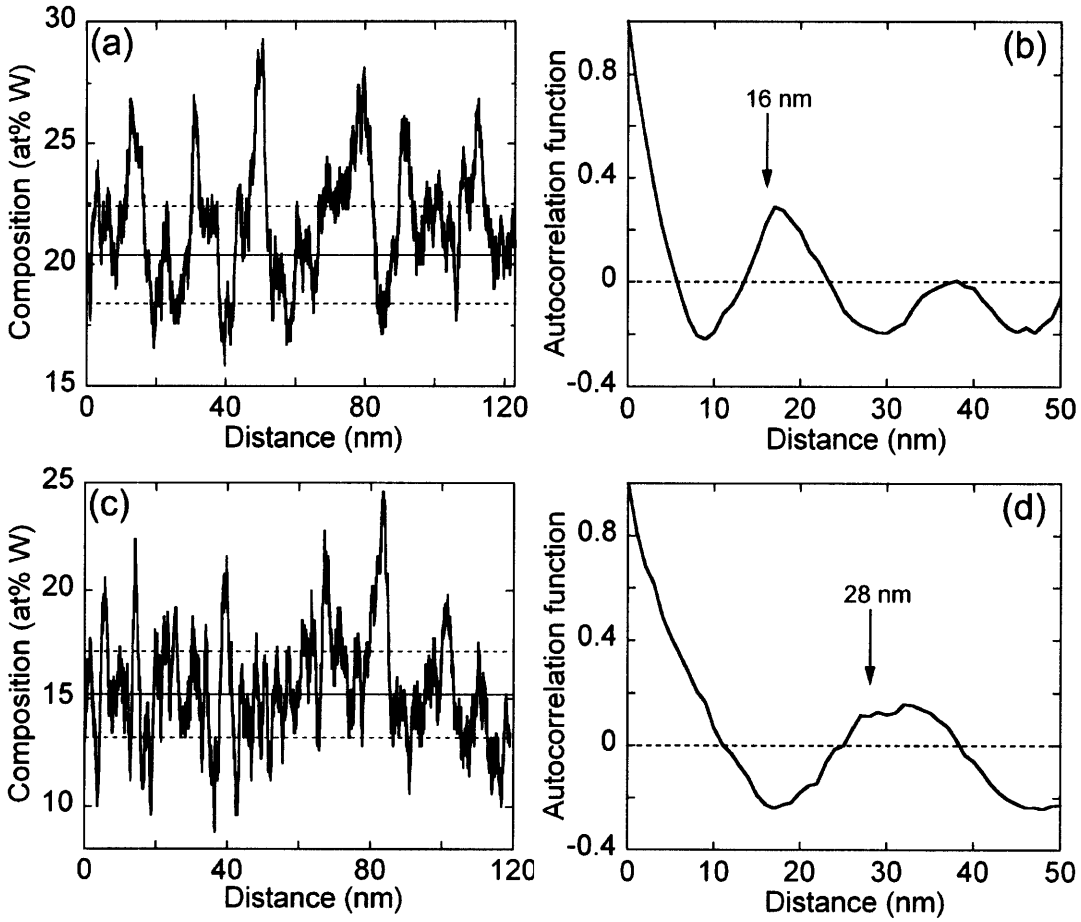

Figure B.2: Composition profiles constructed from atom probe data in the heat treated (a) ~16 nm grain size and (c) ~28 nm grain size Ni-W alloys. Autocorrelation functions revealing characteristic wavelengths in the composition profiles of (a) and (c) are presented as (b) and (d), respectively. The wavelengths are consistent with the measured grain size in both alloys, suggesting W segregation at the grain boundaries.

analysis are plotted as points in Fig. B.3 (a) and (b) for the ~16 nm and ~28 nm grain size alloys, respectively. To extract an average grain interior and boundary composition, this data is fit with a model function (Eq. 4.3) that superimposes two normal distributions, one each for the grain interior and boundary regions. A weighting factor is introduced to account for the contribution of these individual regions based on the measured grain size of the alloy; more details on this procedure can be found in Chapter 4.

Best-fits of the model function to the experimental data are plotted as solid black lines in Fig. B.3. Also shown for illustrative purposes are the individual distributions for the grain interior and boundary regions in red and blue, respectively. In all cases the standard deviation of these

regions amounted to 4.0 ± 0.1 at%W, which is near that expected for random solid solutions at these compositions. The grain interior and boundary compositions extracted from this analysis are, for the ~16 nm grain size specimen: 19.6 and 25.6, and for the ~28 nm grain size specimen: 14.6 and 21.2 at%W, respectively. These values are well in line with the amplitude of composition fluctuations in Fig. B.2(a, c), and present a statistical estimate of the average W content in the grain interior and grain boundary regions. Note that the ~6 at% solute enhancement measured here constitutes a relatively subtle degree of grain boundary segregation as compared to previous atom probe studies of heat-treated nanocrystalline alloys [82].

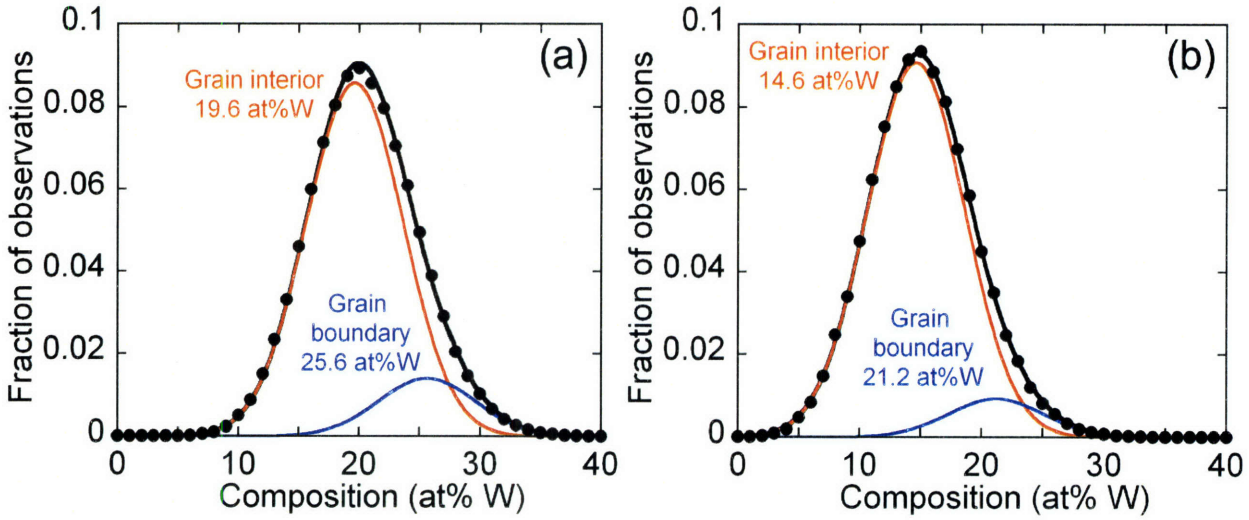

Figure B.3: Composition distributions for the heat treated (a) ~16 nm grain size and (b) ~28 nm grain size Ni-W alloys. A double-normal model fit to the experimental points yields information about the individual grain interior (red) and grain boundary (blue) distributions.

The subtle extent of segregation estimated for the present Ni-W alloys, in combination with high global solute contents, would normally prevent positive identification of grain boundaries based solely on the distribution of W in atom map images. However, in comparison to crystalline regions, grain boundaries are sometimes found to yield higher local evaporation/detection rates in atom probe experiments [182, 197, 221]. This, in turn, enables grain boundaries to be distinguished in the structure as regions of *apparently* higher density. Atom maps for W are presented in Fig. B.4(a, b) for the ~16 and ~28 nm specimens, respectively, and, due to enhanced evaporation at the boundaries, the grain structure can be directly observed in these images.

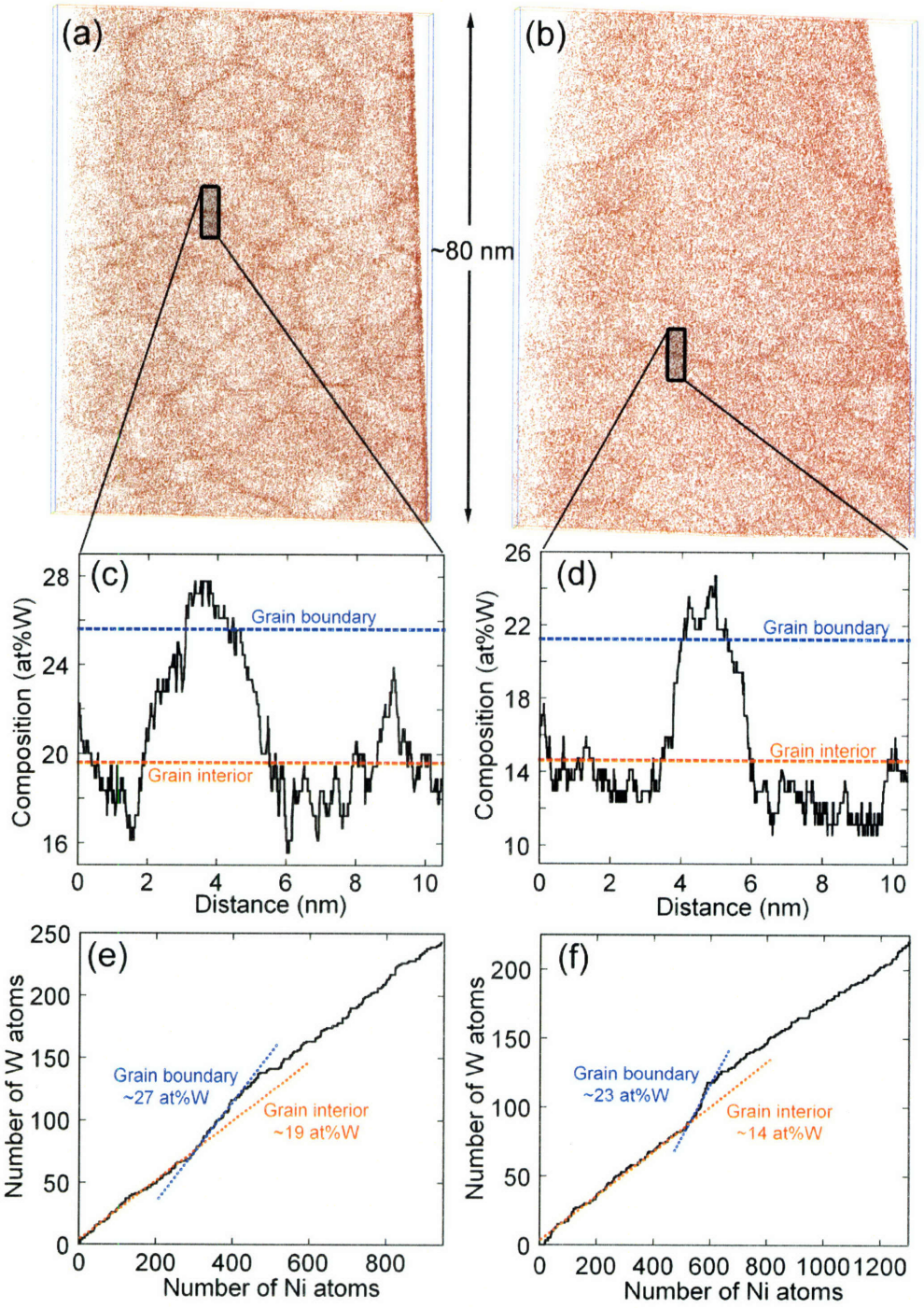

Figure B.4: Atom maps plotting the position of individual W atoms within a 4 nm slice of the heat treated (a) ~16 and (b) ~28 nm grain size specimens; the grain structure is seen in these images due to enhanced evaporation from the grain boundary regions. Typical (c, d) composition profiles and (e, f) ladder diagrams are taken across known grain boundary positions in (a, b), respectively. Segregation of W is observed in these constructions and the extent is consistent with the statistical analysis of Fig. B.3.

The clear observation of grain boundaries in the heat treated specimens of Fig. B.4(a, b) was proposed to be the result of grain boundary relaxation in Chapter 5 (cf. Fig. 5.9(a, b)). In any case, the additional structural information revealed here enables a direct analysis of grain boundary composition for comparison with the statistical methods used earlier.

Traditional composition profiles and ladder diagrams are presented in Fig. B.4(c-f), taken directly from the atom map images as indicated; note that these are typical results based on a number of independent measurements of various grain boundaries in the structures. These constructions represent two of the most common techniques employed in atom probe analyses of interfacial segregation when the position of the interface is known [184, 185]. The composition profiles in Fig. B.4(c, d) were constructed using the same moving average technique as in Fig. B.2(a, c) and show peaks in W content consistent with the grain boundary locations. All boundaries examined revealed similar amplitudes within ± 4 at%W of those plotted in Fig. B.4(c, d). Overlaid on these plots as blue and red dashed lines, respectively, are the grain boundary and interior compositions approximated by the statistical technique of Fig. B.3. As a first direct comparison, the statistical predictions are found to line up very well with the observed composition profiles.

The ladder diagrams of Fig. B.4(e, f) represent an additional method to visualize and measure grain boundary segregation. In this construction, the cumulative number of W atoms is plotted as a function of Ni atoms, taken sequentially along the same sections as examined in the composition profiles. Solute content is directly proportional to the slope of these plots, and the differentiation between grain boundary and grain interior regions is shown schematically with blue and red dashed lines, respectively. Direct calculation of the grain boundary (interior) composition yields values of ~27 (19) and ~23 (14) at%W for the ~16 nm and ~28 nm grain size specimens as indicated. These measurements line up well with the composition profile peaks of Fig. B.4(c, d), and are again consistent with the statistical predictions of Fig. B.3.

With unique knowledge of the grain boundary locations, the statistical technique of Chapter 4 has been validated for measuring grain boundary segregation in nanocrystalline alloys. Good agreement between the distribution analyses of Fig. B.3 and the composition profiles and ladder

diagrams of Fig. B.4 suggests the accuracy and robustness of these measurements. Therefore, statistical analysis of atom probe data may be regarded as an accurate technique to characterize grain boundary segregation in nanocrystalline solids.

Appendix C: Isothermal annealing experiments

Table C.1: Compiled data from isothermal heat treatments of nanocrystalline Ni-W. The results are incorporated in the thermal stability study presented in Chapter 5. Specimen preparation and characterization procedures can be found in Chapter 3. Note that this table is continued on the following page.

As-deposited grain size (nm)	Temperature (°C)	Time (hr)	Heat treated XRD grain size (nm)	Microhardness (GPa)
2.9	*as-deposited*			6.73
	150	24	-	7.74
	300	24	4.0	9.27
	400	24	8.8	10.35
	500	0.5	10.9	9.76
		3	11.8	10.82
		12	11.6	11.03
		24	13.8	10.90
		73	12.7	10.89
	600	0.5	12.2	10.55
		3	15.8	11.14
		12	32.7	11.46
		24	38.1	11.11
		72	53.3	11.34
	700	0.5	32.5	10.78
		3	69.4	8.34
		12	100.4	8.31
		24	85.1	8.40
		72	105.9	8.12
18.0	*as-deposited*			6.59
	150	24	-	6.84
	300	24	15.9	7.69
	400	24	19.1	8.95
	500	0.5	23.2	8.46
		3	25.5	9.08
		12	26.2	9.14
		24	35.2	8.83
		73	57.4	8.02
	600	0.5	28.9	9.16
		3	68.1	6.93
		12	72.9	6.42
		24	78.1	6.48
		72	88.7	6.44
	700	0.5	72.7	6.17
		3	94.3	6.16
		12	72.7	6.13
		24	80.4	5.63
		72	72.6	5.57

As-deposited grain size (nm)	Temperature (°C)	Time (hr)	Heat treated XRD grain size (nm)	Microhardness (GPa)
69.0	*as-deposited*			4.77
	150	24	-	4.55
	300	24	76.0	5.12
	400	24	72.0	5.31
	500	0.5	80.5	4.16
		3	82.3	4.63
		12	71.7	4.65
		24	87.0	4.20
		73	70.3	4.62
	600	0.5	95.5	4.67
		3	108.0	4.12
		12	98.6	4.36
		24	126.8	4.10
		72	100.3	3.87
	700	0.5	133.9	4.11
		3	121.5	3.06
		12	150.1	3.06
		24	178.3	3.22
		72	121.7	2.56

References

[1] Gleiter H, *Nanocrystalline materials*, Progress in Materials Science, **33**, 223-315 (1989)

[2] Gleiter H, *Nanostructured materials: basic concepts and microstructure*, Acta Materialia, **48**, 1-29 (2000)

[3] Aus MJ, Szpunar B, El-Sherik AM, et al., *Magnetic properties of bulk nanocrystalline nickel*, Scripta Metallurgica et Materialia, **27**, 1639-1643 (1992)

[4] Grossinger R, Sato R, Holzer D, et al., *Properties, benefits, and application of nanocrystalline structures in magnetic materials*, Advanced Engineering Materials, **5**, 285-290 (2003)

[5] Herzer G, *Anisotropies in soft magnetic nanocrystalline alloys*, Journal of Magnetism and Magnetic Materials, **294**, 99-106 (2005)

[6] Jiles DC, *Recent advances and future directions in magnetic materials*, Acta Materialia, **51**, 5907-5939 (2003)

[7] Kim SH, Erb U, Aust KT, et al., *The corrosion behavior of nanocrystalline electrodeposits*, Plating and Surface Finishing, **91**, 68-70 (2004)

[8] Kumar KS, Suresh S, Chisholm MF, et al., *Deformation of electrodeposited nanocrystalline nickel*, Acta Materialia, **51**, 387-405 (2003)

[9] Kumar KS, Van Swygenhoven H, Suresh S, *Mechanical behavior of nanocrystalline metals and alloys*, Acta Materialia, **51**, 5743-5774 (2003)

[10] Lu L, Shen Y, Chen X, et al., *Ultrahigh strength and high electrical conductivity in copper*, Science, **304**, 422-426 (2004)

[11] Lund AC, Schuh CA, *Strength asymmetry in nanocrystalline metals under multiaxial loading*, Acta Materialia, **53**, 3193-3205 (2005)

[12] McHenry ME, Willard MA, Laughlin DE, *Amorphous and nanocrystalline materials for applications as soft magnets*, Progress in Materials Science, **44**, 291-433 (1999)

[13] Meyers MA, Mishra A, Benson DJ, *Mechanical properties of nanocrystalline materials*, Progress in Materials Science, **51**, 427-556 (2006)

[14] Schiotz J, Jacobsen KW, *A maximum in the strength of nanocrystalline copper*, Science, **301**, 1357-1359 (2003)

[15] Suzuki T, Kosacki I, Anderson HU, *Microstructure-electrical conductivity relationships in nanocrystalline ceria thin films*, Solid State Ionics, **151**, 111-121 (2002)

[16] Wang LP, Zhang JY, Gao Y, et al., *Grain size effect in corrosion behavior of electrodeposited nanocrystalline Ni coatings in alkaline solution*, Scripta Materialia, **55**, 657-660 (2006)

[17] Wolf D, Yamakov V, Phillpot SR, et al., *Deformation of nanocrystalline materials by molecular-dynamics simulation: relationship to experiments?*, Acta Materialia, **53**, 1-40 (2005)

[18] Yamakov V, Wolf D, Phillpot SR, et al., *Deformation mechanism crossover and mechanical behaviour in nanocrystalline materials*, Philosophical Magazine Letters, **83**, 385-393 (2003)

[19] Youssef KMS, Koch CC, Fedkiw PS, *Improved corrosion behavior of nanocrystalline zinc produced by pulse-current electrodeposition*, Corrosion Science, **46**, 51-64 (2004)

[20] Palumbo G, Thorpe SJ, Aust KT, *On the contribution of triple junctions to the structure and properties of nanocrystalline materials*, Scripta Metallurgica et Materialia, **24**, 1347-1350 (1990)
[21] Sutton AP, Balluffi RW, *Interfaces in Crystalline Materials*, New York, Oxford University Press (1995)
[22] Finnis MW, Sinclair JE, *A simple empirical N-body potential for transition metals*, Philosophical Magazine A, **50**, 45-55 (1984)
[23] Daw MS, Foiles SM, Baskes MI, *The Embedded-Atom Method - a Review of Theory and Applications*, Materials Science Reports, **9**, 251-310 (1993)
[24] Heffelfinger GS, *Parallel atomistic simulations*, Computer Physics Communications, **128**, 219-237 (2000)
[25] Hall EO, *The deformation and ageing of mild steel III. Discussion of results*, Proceedings of the Physical Society, **64**, 747-753 (1951)
[26] Nieh TG, Wadsworth J, *Hall-Petch relation in nanocrystalline solids*, Scripta Metallurgica et Materialia, **25**, 955-958 (1991)
[27] Van Vliet KJ, Tsikata S, Suresh S, *Model experiments for direct visualization of grain boundary deformation in nanocrystalline metals*, Applied Physics Letters, **83**, 1441-1443 (2003)
[28] Gutkin MY, Ovid'ko IA, Pande CS, *Theoretical models of plastic deformation processes in nanocrystalline materials*, Reviews on Advanced Materials Science, **2**, 80-102 (2001)
[29] Fan GJ, Choo H, Liaw PK, et al., *A model for the inverse Hall-Petch relation of nanocrystalline materials*, Materials Science & Engineering, **A409**, 243-248 (2005)
[30] Nan CW, Tschope A, Holten S, et al., *Grain size-dependent electrical properties of nanocrystalline ZnO*, Journal of Applied Physics, **85**, 7735-7740 (1999)
[31] Yamasaki T, Tomohira R, Ogino Y, et al., *Formation of ductile amorphous and nanocrystalline Ni-W alloys by electrodeposition*, Plating and Surface Finishing, **87**, 148-152 (2000)
[32] Erb U, *Electrodeposited nanocrystals: synthesis, properties and industrial applications*, Nanostructured Materials, **6**, 533-538 (1995)
[33] Ebrahimi F, Bourne GR, Kelly MS, et al., *Mechanical properties of nanocrystalline nickel produced by electrodeposition*, Nanostructured Materials, **11**, 343-350 (1999)
[34] Hughes GD, Smith SD, Pande CS, et al., *Hall-Petch strengthening for the microhardness of twelve nanometer grain diameter electrodeposited nickel*, Scripta Metallurgica, **20**, 93-97 (1986)
[35] Courtney TH, *Mechanical Behavior of Materials*, Boston, McGraw Hill (2000)
[36] Dalla Torre F, Spatig P, Schaublin R, et al., *Deformation behaviour and microstructure of nanocrystalline electrodeposited and high pressure torsioned nickel*, Acta Materialia, **53**, 2337-2349 (2005)
[37] Khan AS, Zhang H, Takacs L, *Mechanical response and modeling of fully compacted nanocrystalline iron and copper*, International Journal of Plasticity, **16**, 1459-1476 (2000)
[38] Koch CC, *Top-down synthesis of nanostructured materials: mechanical and thermal processing methods*, Reviews on Advanced Materials Science, **5**, 91-99 (2003)
[39] Koch CC, Youssef KM, Scattergood RO, et al., *Breakthroughs in optimization of mechanical properties of nanostructured metals and alloys*, Advanced Engineering Materials, **7**, 787-794 (2005)

[40] Valiev R, *Nanostructuring of metals by severe plastic deformation for advanced properties*, Nature Materials, **3**, 511-516 (2004)
[41] Koch CC, *Synthesis of nanostructured materials by mechanical milling: problems and opportunities*, Nanostructured Materials, **9**, 13-22 (1997)
[42] Koch CC, Malow TR, *The ductility problem in nanocrystalline materials*, Materials Science Forum, **312-314**, 565-574 (1999)
[43] Koch CC, Narayan J, *The inverse Hall-Petch effect - fact or artifact?*, Materials Research Society Symposium Proceedings, **634**, B5.1.1-B5.1.11, Boston, MA, USA (2001)
[44] Weissmuller J, *Alloy effects in nanostructures*, Nanostructured Materials, **3**, 261-272 (1993)
[45] Kirchheim R, *Grain coarsening inhibited by solute segregation*, Acta Materialia, **50**, 413-419 (2002)
[46] Liu F, Kirchheim R, *Nano-scale grain growth inhibited by reducing grain boundary energy through solute segregation*, Journal of Crystal Growth, **264**, 385-391 (2004)
[47] Beke DL, Cserhati C, Szabo IA, *Segregation inhibited grain coarsening in nanocrystalline alloys*, Journal of Applied Physics, **95**, 4996-5001 (2004)
[48] Cserhati C, Szabo IA, Beke DL, *Size effects in surface segregation*, Journal of Applied Physics, **83**, 3021-3027 (1998)
[49] Krill CE, Ehrhardt H, Birringer R, *Grain-size Stabilization in Nanocrystalline Materials*, in *Chemistry and Physics of Nanostructures and Related Non-Equilibrium Materials*, E. Ma, et al., Warrendale, PA, The Minerals, Metals, and Materials Society (1997)
[50] Krill CE, Ehrhardt H, Birringer R, *Thermodynamic stabilization of nanocrystallinity*, Zeitschrift Fur Metallkunde, **96**, 1134-1141 (2005)
[51] Krill CE, Klein R, Janes S, et al., *Thermodynamic stabilization of grain boundaries in nanocrystalline alloys*, Materials Science Forum, **179-181**, 443-448 (1995)
[52] Swaminarayan S, Srolovitz DJ, *Surface segregation in thin films*, Acta Materialia, **44**, 2067-2072 (1996)
[53] Gupta D, *Influence of solute segregation on grain-boundary energy and self-diffusion*, Metallurgical Transactions, **8A**, 1431-1438 (1977)
[54] Gibbs JW, *The collected works of J. Willard Gibbs*, New Haven, Yale University Press (1928)
[55] Humphreys FJ, Hatherly M, *Recrystallization and related annealing phenomena*, Boston, MA, Elsevier (2004)
[56] Weissmuller J, Krauss W, Haubold T, et al., *Atomic structure and thermal stability of nanostructured Y-Fe alloys*, Nanostructured Materials, **1**, 439 (1992)
[57] Farber B, Cadel E, Menand A, et al., *Phosphorus segregation in nanocrystalline Ni-3.6 at.% P alloy investigated with the tomographic atom probe (TAP)*, Acta Materialia, **48**, 789-796 (2000)
[58] da Silva M, Klement U, *A comparison of thermal stability in nanocrystalline Ni- and Co-based materials*, Zeitschrift Fur Metallkunde, **96**, 1009-1014 (2005)
[59] Hibbard G, Aust KT, Palumbo G, et al., *Thermal stability of electrodeposited nanocrystalline cobalt*, Scripta Materialia, **44**, 513-518 (2001)
[60] Hibbard G, Erb U, Aust KT, et al., *Thermal stability of nanostructured electrodeposits*, Materials Science Forum, **386-388**, 387-396 (2002)
[61] Klement U, Erb U, ElSherik AM, et al., *Thermal stability of nanocrystalline Ni*, Materials Science and Engineering A, **203**, 177-186 (1995)

[62] Birringer R, *Nanocrystalline Materials*, Materials Science and Engineering A, **117**, 33-43 (1989)
[63] Malow TR, Koch CC, *Thermal stability of nanocrystalline materials*, Materials Science Forum, **225-227**, 595-604 (1996)
[64] Liao XZ, Kilmametov AR, Valiev RZ, et al., *High-pressure torsion-induced grain growth in electrodeposited nanocrystalline Ni*, Applied Physics Letters, **88**, 021909 (2006)
[65] Fan GJ, Fu LF, Choo H, et al., *Uniaxial tensile plastic deformation and grain growth of bulk nanocrystalline alloys*, Acta Materialia, **54**, 4781-4792 (2006)
[66] Fan GJ, Fu LF, Qiao DC, et al., *Grain growth in a bulk nanocrystalline Co alloy during tensile plastic deformation*, Scripta Materialia, **54**, 2137-2141 (2006)
[67] Sanders PG, Fougere GE, Thompson LJ, et al., *Improvements in the synthesis and compaction of nanocrystalline materials*, Nanostructured Materials, **8**, 243-252 (1997)
[68] Hasnaoui A, Van Swygenhoven H, Derlet PM, *On non-equilibrium grain boundaries and their effect on thermal and mechanical behaviour: a molecular dynamics computer simulation*, Acta Materialia, **50**, 3927-3939 (2002)
[69] Gleiter H, *Nanostructured materials: State of the art and perspectives*, Nanostructured Materials, **6**, 3-14 (1995)
[70] Zhang XH, Wang HY, Kassem M, et al., *Origins of stored enthalpy in cryomilled nanocrystalline Zn*, Journal of Materials Research, **16**, 3485-3495 (2001)
[71] Varin RA, Romanowskahaftek E, *On the Kinetics of the Spreading of Extrinsic Grain-Boundary Dislocations*, Metallurgical Transactions, **17A**, 1967-1975 (1986)
[72] Pumphrey PH, Gleiter H, *Annealing of Dislocations in High-Angle Grain-Boundaries*, Philosophical Magazine, **30**, 593-602 (1974)
[73] Jang D, Atzmon M, *Grain-boundary relaxation and its effect on plasticity in nanocrystalline Fe*, Journal of Applied Physics, **99**, 083504 (2006)
[74] Tschope A, Birringer R, Gleiter H, *Calorimetric Measurements of the Thermal Relaxation in Nanocrystalline Platinum*, Journal of Applied Physics, **71**, 5391-5394 (1992)
[75] Eckert J, Holzer JC, Krill CE, et al., *Structural and Thermodynamic Properties of Nanocrystalline Fcc Metals Prepared by Mechanical Attrition*, Journal of Materials Research, **7**, 1751-1761 (1992)
[76] Gutkin MY, Ovid'ko IA, Pande CS, *Yield stress of nanocrystalline materials: role of grain-boundary dislocations, triple junctions and Coble creep*, Philosophical Magazine, **84**, 847-863 (2004)
[77] Weertman JR, *Hall-Petch Strengthening in Nanocrystalline Metals*, Materials Science and Engineering A, **166**, 161-167 (1993)
[78] Sanders PG, Youngdahl CJ, Weertman JR, *The strength of nanocrystalline metals with and without flaws*, Materials Science and Engineering A, **234**, 77-82 (1997)
[79] Shvindlerman LS, Gottstein G, *Cornerstones of grain structure evolution and stability: Vacancies, boundaries, triple junctions*, Journal of Materials Science, **40**, 819-839 (2005)
[80] Shvindlerman LS, Gottstein G, *Efficiency of drag mechanisms for inhibition of grain growth in nanocrystalline materials*, Zeitschrift Fur Metallkunde, **95**, 239-241 (2004)
[81] Murty BS, Datta MK, Pabi SK, *Structure and thermal stability of nanocrystalline materials*, Sadhana, **28**, 23-45 (2003)

[82] Hentschel T, Isheim D, Kirchheim R, et al., *Nanocrystalline Ni-3.6 at.% P and its transformation sequence studied by atom-probe field-ion microscopy*, Acta Materialia, **48**, 933-941 (2000)

[83] Talin AA, Marquis EA, Goods SH, et al., *Thermal stability of Ni-Mn electrodeposits*, Acta Materialia, **54**, 1935-1947 (2006)

[84] Choi P, Al-Kassab T, Gartner F, et al., *Thermal stability of nanocrystalline nickel-18 at.% tungsten alloy investigated with the tomographic atom probe*, Materials Science and Engineering A, **353**, 74-79 (2003)

[85] Choi P, Da Silva M, Klement U, et al., *Thermal stability of electrodeposited nanocrystalline Co-1.1at.%P*, Acta Materialia, **53**, 4473-4481 (2005)

[86] Kizuka T, Nakagami Y, Ohata T, et al., *Structure and Thermal-Stability of Nanocrystalline Silver Studied by Transmission Electron-Microscopy and Positron-Annihilation Spectroscopy*, Philosophical Magazine A, **69**, 551-563 (1994)

[87] Kuriplach J, van Petegem S, Hou M, et al., *Positron annihilation study of nanocrystalline Ni3Al: Simulations and measurements*, Materials Science Forum, **363-3**, 94-96 (2001)

[88] Segers D, Van Petegem S, Loffler JF, et al., *Positron annihilation study of nanocrystalline iron*, Nanostructured Materials, **12**, 1059-1062 (1999)

[89] Weigand H, Sprengel W, Rower R, et al., *Interfacial free volumes and segregation effects in nanocrystalline Pd85Zr15 studied by positron annihilation*, Applied Physics Letters, **84**, 3370-3372 (2004)

[90] Weertman J, Sanders PG, *Plastic deformation of nanocrystalline metals*, Solid State Phenomena, **35-36**, 249-262 (1994)

[91] Eckert J, Holzer JC, Johnson WL, *Thermal-Stability and Grain-Growth Behavior of Mechanically Alloyed Nanocrystalline Fe-Cu Alloys*, Journal of Applied Physics, **73**, 131-141 (1993)

[92] Lu K, Wei WD, Wang JT, *Grain-Growth Kinetics and Interfacial Energies in Nanocrystalline Ni-P Alloys*, Journal of Applied Physics, **69**, 7345-7347 (1991)

[93] Ebrahimi F, Li HQ, *Grain growth in electrodeposited nanocrystalline fcc Ni-Fe alloys*, Scripta Materialia, **55**, 263-266 (2006)

[94] Boylan K, Ostrander D, Erb U, et al., *In-situ tem study of the thermal stability of nanocrystalline Ni-P*, Scripta Metallurgica et Materialia, **25**, 2711-2716 (1991)

[95] Schuh CA, Nieh TG, Iwasaki H, *The effect of solid solution W additions on the mechanical properties of nanocrystalline Ni*, Acta Materialia, **51**, 431-443 (2003)

[96] Gabriel A, Lukas HL, Allibert CH, et al., *Experimental and Calculated Phase Diagrams of the Ni-W, Co-W, and Co-Ni-W Systems*, Zeitschrift Fur Metallkunde, **76**, 589-595 (1985)

[97] Seidman DN, *Subnanoscale studies of segregation at grain boundaries: Simulations and experiments*, Annual Review of Materials Science, **32**, 235-269 (2002)

[98] Foiles SM, Seidman DN, *Atomic resolution study of solute-atom segregation at grain boundaries: experiments and Monte Carlo simulations*, in *Materials interfaces : atomic-level structure and properties*, D. Wolf and S. Yip, New York, Chapman & Hall (1992)

[99] Lejcek P, Hofmann S, *Thermodynamics and Structural Aspects of Grain-Boundary Segregation*, Critical Reviews in Solid State and Materials Sciences, **20**, 1-85 (1995)

[100] Millett PC, Selvam RP, Saxena A, *Molecular dynamics simulations of grain size stabilization in nanocrystalline materials by addition of dopants*, Acta Materialia, **54**, 297-303 (2006)

[101] Millett PC, Selvan RP, Bansal S, et al., *Atomistic simulation of grain boundary energetics - Effects of dopants*, Acta Materialia, **53**, 3671-3678 (2005)
[102] Detor AJ, Schuh CA, *Grain boundary segregation, chemical ordering, and stability of nanocrystalline alloys: Atomistic computer simulations in the Ni-W system*, Acta Materialia, in press, (2007)
[103] Kong LT, Liu JB, Lal WS, et al., *Correlation of lattice constant versus tungsten concentration of the Ni-based solid solution examined by molecular dynamics simulation*, Journal of Alloys and Compounds, **337**, 143-147 (2002)
[104] Morawiec A, *Misorientation-angle distribution of randomly oriented symmetric objects*, Journal of Applied Crystallography, **28**, 289-293 (1995)
[105] Foiles SM, *Calculation of Grain-Boundary Segregation in Ni-Cu Alloys*, Physical Review B, **40**, 11502-11506 (1989)
[106] Rittner JD, Foiles SM, Seidman DN, *Simulation of surface segregation free energies*, Physical Review B, **50**, 12004-12014 (1994)
[107] Seah MP, *Grain boundary segregation*, Journal of Physics F (Metal Physics), **10**, 1043-1064 (1980)
[108] Mishra NS, Ranganathan S, *Electron-Microscopy and Diffraction of Ordering in an Off-Stoichiometric Ni-W Alloy*, Scripta Metallurgica et Materialia, **27**, 1337-1342 (1992)
[109] Mishra NS, Ranganathan S, *Electron-Microscopy and Diffraction of Ordering in Ni-W Alloys*, Acta Metallurgica Et Materialia, **43**, 2287-2302 (1995)
[110] Liu JB, Yang GW, Liu BX, et al., *Possible metastable states in the Ni-W system predicted by ab initio calculations*, Physical Review B, **62**, 11277-11279 (2000)
[111] Mishra NS, Ranganathan S, *Electron-Microscopy and Diffraction of Ordering in a Ni-25wt%Mo Alloy*, Materials Science and Engineering A, **150**, 75-85 (1992)
[112] Arya A, Banerjee S, Das GP, et al., *A first-principles thermodynamic approach to ordering in Ni-Mo alloys*, Acta Materialia, **49**, 3575-3587 (2001)
[113] Cao SQ, Brooks CR, Allard L, *In-Situ Transmission Electron-Microscopy Study of Ordering in a Splat-Cooled Ni-20 at-Percent Mo Alloy*, Materials Characterization, **34**, 87-95 (1995)
[114] Oramus P, Kozubski R, Pierron-Bohnes V, et al., *Computer simulation of long-range order relaxation in homogeneous systems*, Materials Science and Engineering A, **324**, 11-15 (2002)
[115] Pareige C, Soisson F, Martin G, et al., *Ordering and phase separation in Ni-Cr-Al: Monte Carlo simulations vs three-dimensional atom probe*, Acta Materialia, **47**, 1889-1899 (1999)
[116] Pourovskii LV, Ruban AV, Abrikosov IA, et al., *Bulk ordering and surface segregation in Ni50Pt50*, Physical Review B, **64**, 035421 (2001)
[117] Hata S, Fujita H, Schlesier CG, et al., *Monte Carlo study of ordering processes in fcc-based Ni-Mo alloys*, Materials Transactions, **39**, 133-138 (1998)
[118] Kulkarni UD, *Monte Carlo simulation of ordering transformations in Ni-Mo-based alloys*, Acta Materialia, **52**, 2721-2732 (2004)
[119] Muller S, *Bulk and surface ordering phenomena in binary metal alloys*, Journal of Physics-Condensed Matter, **15**, R1429-R1500 (2003)
[120] Sundaram VS, Alben RS, Robertson WD, *Order-Disorder Transformation at a (100) Surface of Cu3au - Theory and Experiment*, Surface Science, **46**, 653-671 (1974)

[121] Dosch H, Mailander L, Lied A, et al., *Experimental-Evidence for an Interface Delocalization Transition in Cu3Au*, Physical Review Letters, **60**, 2382-2385 (1988)
[122] Dosch H, Reichert H, *Ordering, disordering and segregation at binary interfaces: Model system Cu3Au(001)*, Acta Materialia, **48**, 4387-4393 (2000)
[123] Bikondoa O, Castro GR, Torrelles X, et al., *Surface-induced disorder on the clean Ni3Al(111) surface*, Physical Review B, **72**, 195430 (2005)
[124] Binder K, *Monte carlo simulations of surfaces and interfaces in materials*, in *Stability of materials*, A. Gonis, P.E.A. Turchi and J. Kudrnovsky, New York, Plenum Press (1996)
[125] Yang B, Asta M, Mryasov ON, et al., *The nature of A1-L1(0) ordering transitions in alloy nanoparticles: A Monte Carlo study*, Acta Materialia, **54**, 4201-4211 (2006)
[126] Lipowsky R, *Critical Surface Phenomena at 1st-Order Bulk Transitions*, Physical Review Letters, **49**, 1575-1578 (1982)
[127] Lipowsky R, Gompper G, *Interface Delocalization Transitions in Finite Systems*, Physical Review B, **29**, 5213-5215 (1984)
[128] Farkas D, Jang H, *Grain-Boundary Ordering, Segregation, and Melting Transitions in a Two-Dimensional Lattice-Gas Model*, Physical Review B, **39**, 11769-11774 (1989)
[129] McLean D, *Grain boundaries in metals*, Oxford, Clarendon Press (1957)
[130] Rittner JD, Udler D, Seidman DN, et al., *Atomic scale structural effects on solute-atom segregation at grain boundaries*, Physical Review Letters, **74**, 1115-1118 (1995)
[131] Ishida K, *Effect of grain size on grain boundary segregation*, Journal of Alloys and Compounds, **235**, 244-249 (1996)
[132] Najafabadi R, Wang HY, Srolovitz DJ, et al., *The Effects of Segregation on Grain-Boundary Cohesive Energies in Ni3-XAl1+X*, Scripta Metallurgica et Materialia, **25**, 2497-2502 (1991)
[133] Lee BJ, Choi SH, *Computation of grain boundary energies*, Modelling and Simulation in Materials Science and Engineering, **12**, 621-632 (2004)
[134] Starostenkov MD, Demyanov BF, Kustov SL, et al., *Computer modeling of grain boundaries in Ni3Al*, Computational Materials Science, **14**, 146-151 (1999)
[135] Murr LE, *Interfacial phenomena in metals and alloys*, Reading, MA, Addison-Wesley (1975)
[136] Younes O, Gileadi E, *Electroplating of Ni/W alloys*, Journal of the Electrochemical Society, **149**, 100-111 (2002)
[137] Younes O, Gileadi E, *Electroplating of high tungsten content Ni/W alloys*, Electrochemical and Solid State Letters, **3**, 543-545 (2000)
[138] Sridhar TM, Eliaz N, Gileadi E, *Electroplating of Ni4W*, Electrochemical and Solid State Letters, **8**, C58-C61 (2005)
[139] Atanassov N, Gencheva K, Bratoeva M, *Properties of nickel-tungsten alloys electrodeposited from sulfamate electrolyte*, Plating and Surface Finishing, **84**, 67-71 (1997)
[140] Wu Y, Chang D, Kim D, et al., *Influence of boric acid on the electrodepositing process and structures of Ni-W alloy coating*, Surface & Coatings Technology, **173**, 259-264 (2003)
[141] Wu YY, Chang DY, Kwon SC, et al., *Ni-W alloy electrodeposition from a bath containing an organic amine substitute for inorganic ammonia*, Plating and Surface Finishing, **90**, 46-49 (2003)

[142] Obradovic MD, Bosnjakov GZ, Stevanovic RM, et al., *Pulse and direct current plating of Ni-W alloys from ammonia-citrate electrolyte*, Surface & Coatings Technology, **200**, 4201-4207 (2006)
[143] Obradovic MD, Stevanovic RM, Despic AR, *Electrochemical deposition of Ni-W alloys from ammonia-citrate electrolyte*, Journal of Electroanalytical Chemistry, **552**, 185-196 (2003)
[144] Younes O, Zhu L, Rosenberg Y, et al., *Electroplating of amorphous thin films of tungsten/nickel alloys*, Langmuir, **17**, 8270-8275 (2001)
[145] Wu YY, Chang DY, Kim DS, et al., *Effects of 2-butyne-1,4-diol on structures and morphologies of electroplating Ni-W alloy*, Surface and Coatings Technology, **162**, 269-275 (2003)
[146] Yamasaki T, Schlossmacher P, Ehrlich K, et al., *Formation of amorphous electrodeposited Ni-W alloys and their nanocrystallization*, Nanostructured Materials, **10**, 375-388 (1998)
[147] Yamasaki T, *High-strength nanocrystalline Ni-W alloys produced by electrodeposition and their embrittlement behaviors during grain growth*, Scripta Materialia, **44**, 1497-1502 (2001)
[148] Somekawa H, Nieh TG, Higashi K, *Instrumented indentation properties of electrodeposited Ni-W alloys with different microstructures*, Scripta Materialia, **50**, 1361-1365 (2004)
[149] Giga A, Kimoto Y, Takigawa Y, et al., *Demonstration of an inverse Hall-Petch relationship in electrodeposited nanocrystalline Ni-W alloys through tensile testing*, Scripta Materialia, **55**, 143-146 (2006)
[150] Sriraman KR, Raman SGS, Seshadri SK, *Synthesis and evaluation of hardness and sliding wear resistance of electrodeposited nanocrystalline Ni-W alloys*, Materials Science and Engineering A, **418**, 303-311 (2006)
[151] Hwang WS, Cho WS, *The effect of tungsten content on nanocrystalline structure of Ni-W alloy electrodeposits*, Materials Science Forum, **510-511**, 1062-1065 (2006)
[152] Iwasaki H, Higashi K, Nieh TG, *Tensile deformation and microstructure of a nanocrystalline Ni-W alloy produced by electrodeposition*, Scripta Materialia, **50**, 395-399 (2004)
[153] Slavcheva E, Mokwa W, Schnakenberg U, *Electrodeposition and properties of NiW films for MEMS application*, Electrochimica Acta, **50**, 5573-5580 (2005)
[154] Lee DB, Ko JH, Kwon SC, *High temperature oxidation of Ni-W coatings electroplated on steel*, Materials Science and Engineering A, **380**, 73-78 (2004)
[155] Sulitanu N, Brinza F, *Structure properties relationships in electrodeposited Ni-W thin films with columnar nanocrystallites*, Journal of Optoelectronics and Advanced Materials, **5**, 421-427 (2003)
[156] Lee DB, Ko JH, Kwon SC, *Oxidation of Ni-W coatings at 700 and 800 degrees C in air*, Surface and Coatings Technology, **193**, 292-296 (2005)
[157] Zhu L, Younes O, Ashkenasy N, et al., *STM/AFM studies of the evolution of morphology of electroplated Ni/W alloys*, Applied Surface Science, **200**, 1-14 (2002)
[158] Schlossmacher P, Yamasaki T, *Structural analysis of electroplated amorphous-nanocrystalline Ni-W*, Mikrochimica Acta, **132**, 309-313 (2000)

[159] Nasu T, Sakurai M, Kamiyama T, et al., *EXAFS study on amorphous and nanocrystalline M-W (M=Fe, Ni) alloys produced by electrodeposition*, Journal of Non-Crystalline Solids, **312**, 319-322 (2002)
[160] Nasu T, Sakurai M, Kamiyama T, et al., *Microstructure of M-W (M=Fe, Ni) alloys produced by electrodeposition and mechanical alloying*, Materials Science Forum, **426-4**, 4585-4590 (2003)
[161] Hosokawa H, Yamasaki T, Sugamoto N, et al., *Bending properties of nanocrystalline Ni-18at% W alloy produced by electrodeposition*, Materials Transactions, **45**, 1807-1810 (2004)
[162] Detor AJ, Schuh CA, *Tailoring and patterning the grain size of nanocrystalline alloys*, Acta Materialia, **55**, 371-379 (2007)
[163] Zhang Z, Zhou F, Lavernia EJ, *On the analysis of grain size in bulk nanocrystalline materials via x-ray diffraction*, Metallurgical and Materials Transactions, **34A**, 1349-1355 (2003)
[164] Choo RTC, Toguri JM, El-Sherik AM, et al., *Mass transfer and electrocrystallization analyses of nanocrystalline nickel production by pulse plating*, Journal of Applied Electrochemistry, **25**, 384-403 (1995)
[165] Qu NS, Zhu D, Chan KC, et al., *Pulse electrodeposition of nanocrystalline nickel using ultra narrow pulse width and high peak current density*, Surface and Coatings Technology, **168**, 123-128 (2003)
[166] Natter H, Schmelzer M, Hempelmann R, *Nanocrystalline nickel and nickel-copper alloys: synthesis, characterization, and thermal stability*, Journal of Materials Research, **13**, 1186-1197 (1998)
[167] Wong KP, Chan KC, Yue TM, *A study of hardness and grain size in pulse current electroforming of nickel using different shaped waveforms*, Journal of Applied Electrochemistry, **31**, 25-34 (2001)
[168] Tsai W-C, Wan C-C, Wang Y-Y, *Mechanism of copper electrodeposition by pulse current and its relation to current efficiency*, Journal of Applied Electrochemistry, **32**, 1371-1378 (2002)
[169] Saber K, Koch CC, Fedkiw PS, *Pulse current electrodeposition of nanocrystalline zinc*, Materials Science and Engineering A, **341**, 174-181 (2003)
[170] Youssef KMS, Koch CC, Fedkiw PS, *Influence of additives and pulse electrodeposition parameters on production of nanocrystalline zinc from zinc chloride electrolytes*, Journal of the Electrochemical Society, **151**, C103-C111 (2004)
[171] Nee CC, Kim W, R. W, *Pulsed Electrodeposition of Ni-Mo Alloys*, Journal of the Electrochemical Society, 1100-1103 (1988)
[172] Yang JM, Zhu D, Qu NS, et al., *Pulse electroforming of nanocrystalline Ni-Mn alloy*, Key Engineering Materials, **259-260**, 596-601 (2004)
[173] Chassaing E, Roumegas MP, Trichet MF, *Electrodeposition of Ni-Mo alloys with pulse reverse potentials*, Journal of Applied Electrochemistry, **25**, 667-670 (1995)
[174] Aroyo A, Tzonev N, *Pulse periodic reverse plating-possibilities for electrodeposition of metal coatings with improved properties: Part 2*, Plating and Surface Finishing, **90**, 50-54 (2003)
[175] Aroyo M, Tzonev N, *Pulse periodic reverse plating - New possibilities for electrodeposition of metal coatings with improved properties: Part 1*, Plating and Surface Finishing, **89**, 48-53 (2002)

[176] Qu NS, Chan KC, Zhu D, *Surface roughening in pulse current and pulse reverse current electroforming of nickel*, Surface and Coatings Technology, **91**, 220-224 (1997)
[177] Vasko AT, *Chromium, Molybdenum, and Tungsten*, in *Standard potentials in aqueous solution*, A.J. Bard, New York, NY, M. Dekker (1985)
[178] Vanysek P, *Electrochemical Series*, in *CRC Handbook of Chemistry and Physics*, D.R. Lide, Cleveland, OH, CRC Press (2006)
[179] Raub E, Muller K, *Fundamentals of Metal Deposition*, New York, Elsevier Publishing Company (1967)
[180] Moussa SO, Ibrahim MAM, Abd El Rehim SS, *Induced electrodeposition of tungsten with nickel from acidic citrate electrolyte*, Journal of Applied Electrochemistry, **36**, 333-338 (2006)
[181] Brenner A, *Electrodeposition of alloys: principles and practice*, New York, NY, Academic Press (1963)
[182] Miller MK, *Three-dimensional atom probes*, Journal of Microscopy, **186**, 1-16 (1997)
[183] Miller MK, *The development of atom probe field-ion microscopy*, Materials Characterization, **44**, 11-27 (2000)
[184] Miller MK, *Atom Probe Tomography: Analysis at the Atomic Level*, Boston, Kluwer Academic/Plenum Publishers (2000)
[185] Miller MK, Cerezo A, Hetherington MG, et al., *Atom Probe Field Ion Microscopy*, Oxford, Clarendon Press (1996)
[186] Thuvander M, Andren HO, *APFIM studies of grain and phase boundaries: A review*, Materials Characterization, **44**, 87-100 (2000)
[187] Henjered A, Norden H, *A Controlled Specimen Preparation Technique for Interface Studies with Atom-Probe Field-Ion Microscopy*, Journal of Physics E, **16**, 617-619 (1983)
[188] Karlsson L, Norden H, *The Determination of Grain-Boundary Segregation Profiles in Boron Containing Austenitic Stainless-Steels Using Tem, Ap and Iap*, Journal De Physique, **45**, 391-396 (1984)
[189] Horton JA, Miller MK, *An atom probe study of boron segregation to line and planar defects in Ni3Al*, Materials Research Society Symposium Proceedings, **81**, 105-110, Boston, MA, USA (1987)
[190] Seidman DN, *Solute-atom segregation at internal interfaces on an atomic scale. Atom-probe experiments and computer simulations*, Materials Science and Engineering A, **137**, 57-67 (1991)
[191] Miller MK, Jayaram R, *Characterization of internal interfaces by atom probe field ion microscopy*, Materials Research Society Symposium Proceedings, **295**, 247-252, Boston, MA, USA (1992)
[192] Miller MK, Jayaram R, Russell KF, *Characterization of phosphorus segregation in neutron-irradiated pressure vessel steels by atom probe field ion microscopy*, Materials Research Society Symposium Proceedings, **373**, 113-118, Boston, MA, USA (1994)
[193] Lundin L, Richarz B, *Atom-probe study of phosphorus segregation to the carbide/matrix interface in an aged 9% chromium steel*, Applied Surface Science, **87-88**, 194-199 (1995)
[194] Blavette D, Letellier L, Duval P, et al., *Atomic-scale investigations of grain boundary segregation in Astroloy with a three dimensional atom-probe*, Materials Science Forum, **207-209**, 79-92 (1996)

[195] Seto K, Larson DJ, Warren PJ, et al., *Grain boundary segregation in boron added interstitial free steels studied by 3-dimensional atom probe*, Scripta Materialia, **40**, 1029-1034 (1999)
[196] Warren PJ, Thuvander M, Abraham M, et al., *3-D atom probe studies of some nanostructured materials*, Materials Science Forum, **343-346**, 701-708 (2000)
[197] Abraham M, Holdway P, Thuvander M, et al., *Thermal stability of electrodeposited nanocrystalline nickel*, Surface Engineering, **18**, 151-156 (2002)
[198] Wu YQ, Kramer MJ, Chen Z, et al., *Behavior of Nb atoms in Nb substituted Nd2Fe14B nanocrystalline alloys investigated by atom probe tomography*, IEEE Transactions on Magnetics, **40**, 2886-2888 (2004)
[199] Ohsaki S, Hono K, Hidaka H, et al., *Characterization of nanocrystalline ferrite produced by mechanical milling of pearlitic steel*, Scripta Materialia, **52**, 271-276 (2005)
[200] Abraham M, Thuvander M, Lane HM, et al., *Atomic scale characterisation of electrodeposited nanocrystalline Ni-P alloys*, Materials Research Society Symposium Proceedings, **581**, 517-522, Boston, MA, USA (2000)
[201] Detor AJ, Miller MK, Schuh CA, *Solute distribution in nanocrystalline Ni-W alloys examined through atom probe tomography*, Philosophical Magazine, **86**, 4459-4475 (2006)
[202] Hetherington MG, Miller MK, *On the statistical analysis of atom probe data*, Journal de Physique Colloque, **48**, 559-564 (1987)
[203] Van Genderen MJ, Sijbrandij SJ, Bottger A, et al., *Atom probe analysis of initial decomposition of Fe-N martensite*, Materials Science and Technology, **13**, 806-812 (1997)
[204] Hyde JM, Cerezo A, Hetherington MG, et al., *Three-dimensional characterization and modelling of spinodally decomposed iron-chromium alloys*, Surface Science, **266**, 370-377 (1992)
[205] Oehring M, v. Alvensleben L, *Evaluation of atom probe concentration profiles by autocorrelation analysis*, Journal de Physique Colloque, **49**, 415-420 (1988)
[206] Kendall MG, Stuart A, Ord JK, *The Advanced Theory of Statistics*, New York, Macmillan (1983)
[207] Scheaffer RL, McClave JT, *Probability and Statistics for Engineers*, Belmont, CA, Duxbury Press (1995)
[208] Iwasaki H, Higashi K, Nieh TG, *Effect of Solid-Solution W Addition on the Nanostructure of Electrodeposited Ni*, Materials Research Society Symposium Proceedings, **740**, 119, (2003)
[209] Detor AJ, Schuh CA, *Microstructural evolution during the heat treatment of nanocrystalline Ni-W alloys*, Journal of Materials Research, submitted, (2007)
[210] Klement U, Erb U, Aust KT, *Investigations of the grain growth behaviour of nanocrystalline nickel*, Nanostructured Materials, **6**, 581-584 (1995)
[211] Hibbard GD, McCrea JL, Palumbo G, et al., *An initial analysis of mechanisms leading to late stage abnormal grain growth in nanocrystalline Ni*, Scripta Materialia, **47**, 83-87 (2002)
[212] Mishra NS, Singh CD, Ranganathan S, *Order Hardening in Nickel Molybdenum and Nickel Tungsten Alloys*, Journal of Materials Science, **27**, 1599-1607 (1992)
[213] *ASM Handbooks, v. 3 (alloy phase diagrams)*, Materials Park, OH, ASM International (2003)

[214] Spruiell JE, Stansbury EE, *X-ray study of short-range order in nickel alloys containing 10.7 and 20.0 at% molybdenum*, Journal of the Physics and Chemistry of Solids, **26**, 811-822 (1965)
[215] Das SK, Okamoto PR, Fisher PMJ, et al., *Short-Range Order in Ni-Mo, Au-Cr, Au-V and Au-Mn Alloys*, Acta Metallurgica, **21**, 913-928 (1973)
[216] Okamoto PR, Thomas G, *On short range order and micro-domains in the Ni4Mo system*, Acta Metallurgica, **19**, 825-841 (1971)
[217] Stobbs WM, Stobbs SH, *Short-Range Order in (1-1/2-0) Special-Point Alloys*, Philosophical Magazine B, **53**, 537-544 (1986)
[218] Kumar M, Vasudevan VK, *Ordering reactions in an Ni-25Mo-8Cr alloy*, Acta Materialia, **44**, 1591-1600 (1996)
[219] Volpp T, Goring E, Kuschke WM, et al., *Grain size determination and limits to Hall-Petch behavior in nanocrystalline NiAl powders*, Nanostructured Materials, **8**, 855-865 (1997)
[220] Masumura RA, Hazzledine PM, Pande CS, *Yield stress of fine grained materials*, Acta Materialia, **46**, 4527-4534 (1998)
[221] Forbes RG, *Field Evaporation Theory - A Review of Basic Ideas*, Applied Surface Science, **87-8**, 1-11 (1995)
[222] Burke JE, *Some factors affecting the rate of grain growth in metals*, Transactions of the Metallurgical Society AIME, **180**, 73 (1949)
[223] Burke JE, Turnbull D, *Recrystallization and Grain Growth*, Progress in Metal Physics, **3**, 220 (1952)
[224] Nazarov AA, *Kinetics of grain boundary recovery in deformed polycrystals*, Interface Science, **8**, 315-322 (2000)
[225] Brown AM, Ashby MF, *Correlations for Diffusion Constants*, Acta Metallurgica, **28**, 1085-1101 (1980)
[226] *Smithells Metals Reference Book*, Oxford, Elsevier Butterworth-Heinemann (2004)
[227] Liu F, Kirchheim R, *Comparison between kinetic and thermodynamic effects on grain growth*, Thin Solid Films, **466**, 108-113 (2004)
[228] Mishin Y, Herzig C, *Diffusion in fine-grained materials: Theoretical aspects and experimental possibilities*, Nanostructured Materials, **6**, 859-862 (1995)
[229] Michels A, Krill CE, Ehrhardt H, et al., *Modelling the influence of grain-size-dependent solute drag on the kinetics of grain growth in nanocrystalline materials*, Acta Materialia, **47**, 2143-2152 (1999)
[230] Weertman JR, Farkas D, Hemker K, et al., *Structure and mechanical behavior of bulk nanocrystalline materials*, MRS Bulletin, **24**, 44-50 (1999)
[231] Lu L, Sui ML, Lu K, *Superplastic extensibility of nanocrystalline copper at room temperature*, Science, **287**, 1463-1466 (2000)
[232] Wang Y, Chen M, Zhou F, et al., *High tensile ductility in a nanostructured metal*, Nature, **419**, 912-915 (2002)
[233] Fisher JC, *On the strength of solid solution alloys*, Acta Metallurgica, **2**, 9-10 (1954)
[234] Flinn PA, *Solute hardening of close-packed solid solutions*, Acta Metallurgica, **6**, 631-635 (1958)
[235] Wang H, Yao S, Matsumura S, *Preparation, characterization and the study of the thermal strain in Ni-W gradient deposits with nanostructure*, Surface and Coatings Technology, **157**, 166-170 (2002)

[236] Oliver WC, Pharr GM, *An Improved Technique for Determining Hardness and Elastic-Modulus Using Load and Displacement Sensing Indentation Experiments*, Journal of Materials Research, **7**, 1564-1583 (1992)

[237] Choi IS, Detor AJ, Schwaiger R, et al., *Mechanics of Indentation of Plastically Graded Materials: II. Experiments on Nanocrystalline Alloys with Grain Size Gradients*, Journal of the Mechanics and Physics of Solids, submitted, (2006)

[238] Detor AJ, Miller MK, Schuh CA, *Measuring grain boundary segregation in nanocrystalline alloys: Direct validation of statistical techniques using atom probe tomography*, Philosophical Magazine Letters, to appear, (2007)